Energy & Environmental Science

ROYAL SOCIETY OF CHEMISTRY

REVIEW

View Article Online
View Journal | View Issue

Cite this: *Energy Environ. Sci.*, 2025, **18**, 3917

Emerging strategies for the large-scale fabrication of perovskite solar modules: from design to process

Bochun Kang [a] and Feng Yan *[ab]

Perovskite solar cells (PSCs), recognized as a promising third-generation thin-film photovoltaic technology, offer notable advantages including low-cost production, high power conversion efficiency, and tunable bandgap characteristics. Despite these advancements, scaling up PSCs to large-area perovskite solar modules (PSMs) presents substantial challenges. To overcome the obstacles, alternative deposition methods such as solution-based blade coating, slot-die coating, spray coating, inkjet printing, and screen printing, as well as solvent-free methods like chemical vapor deposition and physical vapor deposition, are being explored to eliminate film inhomogeneity and defects when applied to a larger area. These emerging strategies aim to enhance film quality, uniformity, and scalability, which are essential for large-area applications. This comprehensive review systematically summarizes the manufacturing status of PSMs from fundamental theoretical principles to practical applications in processing, discussing various deposition techniques, and simultaneously exploring strategies to enhance PSM performance in terms of solvent, additive and interface engineering. Additionally, it delves into the stability challenges faced by large-scale manufacturing of commercial products, analyzing and summarizing the latest scribing processing and encapsulation technologies, and providing prospects for module development.

Received 28th November 2024,
Accepted 17th March 2025

DOI: 10.1039/d4ee05613b

rsc.li/ees

Broader context

With the onset of the fossil energy crisis, the efficient utilization of solar energy has become critically important. This has led to significant commercial and research investments in the photovoltaic industry. The promising third-generation photovoltaic solutions, perovskite solar cells, recognized, have garnered substantial attention and made significant advancements in recent years. Certified small-area perovskite solar cell efficiencies have reached 26.7%, rivaling those of silicon solar cells. To facilitate commercialization, developing stable and efficient large-scale perovskite solar modules remains a crucial challenge. The commonly used small-scale spin-coating method in laboratory settings is less effective for large-area applications due to uneven centripetal forces. This comprehensive review addresses the emerging strategies for the large-scale fabrication of perovskite solar modules. Large-area coating techniques primarily include liquid-phase deposition methods (meniscus coating and droplet spraying) and non-liquid-phase deposition methods (physical and chemical vapor deposition). Furthermore, device design, encapsulation, and stability testing of solar modules are essential steps on the path to commercialization.

1. Introduction

Solar panels, as simple and efficient devices for converting renewable solar energy into electricity, have contributed to mitigating the depletion of traditional fossil fuels.[1,2] From the client's perspective, the rapid and sustained demand for photovoltaics (PV), which is forecast to grow by over 30% over the next five years, which has further attracted substantial commercial investment in the scale production of solar cells. As of 2023, the global cumulative installed capacity has exceeded 1 TW-scale.[3,4]

Perovskite solar cells (PSCs), as a promising third-generation thin-film photovoltaic technology, are considered one of the most potentially applicable photovoltaic technologies for the future due to their ease of fabrication, low cost, high power conversion efficiency, and tunable bandgap characteristics.[5–8] Based on the photovoltaic effect, when photons with energy greater than the bandgap of perovskite are absorbed, excitons are generated.[9,10] Due to the low exciton binding energy in the perovskite absorbing layer, excitons rapidly dissociate to form electron–hole pairs.[11] Subsequently, electrons pass through an electron transport layer (ETL) composed of an n-type semiconductor with matched energy levels while holes diffuse across a hole transport layer (HTL) based on a p-type semiconductor in the opposite direction, generating a directed output current.[9,10]

[a] *Department of Applied Physics, Research Center for Organic Electronics, The Hong Kong Polytechnic University, Hung Hom, Kowloon, Hong Kong, P. R. China*
[b] *Research Institute of Intelligent Wearable Systems, The Hong Kong Polytechnic University, Hung Hom, Kowloon, Hong Kong SAR, P. R. China*

Currently, PSCs have undergone rapid development at the laboratory scale. Over the past decades, the power conversion efficiency (PCE) record has been continuously broken, soaring swiftly from 3.8% to over 26%, nearing the record held by silicon solar cells.[12,13]

Typically, small-area PSCs are extensively studied to innovate while conserving materials. However, in terms of real-world PV applications and industry, the scaling up of PSCs is an irresistible trend. In practical applications, large-area PSCs may necessitate the integration of multiple sub-cells into large-area perovskite solar modules (PSMs). The built-in series-connection cells enhance the output voltage while effectively relieving substantial losses due to parasitic resistance arising from charge transport distances within the transparent electrodes.[14] The majority of PSCs now being explored are based on the spin-coating approach, with effective areas in the range of 0.04–1 cm^2.[15,16] When attempting to adopt spin-coating for large-area perovskite production, the radial centrifugal force can severely affect the film quality and form films with severe non-linear inhomogeneous thicknesses along the radial direction.[17] These morphological defects are manifested as numerous ring-shaped pinholes in thinner regions and non-radiative recombination in thicker areas.[18] Nevertheless, the PSMs' requirement for film uniformity, non-pinhole, and nice crystallographic properties are mandatory for the sake of the series circuit. This conflict has stimulated the emergence of new processes for scaling up. Since the first report of PSM by Carlo *et al.*[19] in 2014, research groups worldwide have made significant progress, reaching up to 23.3%,[20] in the development of scalable processes for large-area PSMs and film deposition over the past decade.

Currently, various strategies have been developed in two dominant technique routes, solution-based and solvent-free evaporation, for depositing high-quality large-area perovskite films. These include solution-based blade coating,[21] slot-die coating,[22] spray coating,[23] inkjet printing,[24] and screen printing,[25] as well as solvent-free vapor-based chemical vapor deposition (CVD)[26] and physical vapor deposition (PVD).[27] In response to these blossoming technologies, strategies such as solvent engineering,[28] interface engineering,[29] and additive engineering,[30] *etc.* have been employed to enhance the crystallization, carriers transport laterally and vertically among every single subcell, thereby paving the way for achieving high photovoltaic performance in PSMs.

This review systematically summarizes and discusses PSMs fabricated *via* various deposition technologies. Beginning with fundamental principles, we focus on the captivating and beneficial progress in the production of high-efficiency large-area modules and explore strategies for enhancing PSM performance from the perspectives of auxiliary processes and micro-scale science. Furthermore, we analyze the challenges faced by the large-scale fabrication application of PSMs and propose potential development pathways for future modules.

2. Device configuration

2.1 Perovskite solar modules

The exploration of PSCs performance is typically conducted on individual cells with very small areas in labs, usually ranging from 0.04 to 1 cm^2.[15,16,31] As these small cells are poised for commercial applications, there is an inevitable trend towards scaling up to larger areas. However, when the effective area is increased, the efficiency often experiences a significant decline. This is primarily due to the increased carrier transport distance within the PSC device, resulting in more charge loss over this extended distance. Additionally, the increase in cell area leads to higher internal resistance, hindering the flow of current and reducing current output, thereby resulting in lower PCE.[32,33] Therefore, in response to the challenges of scaling up laboratory-scale photovoltaic cells for commercial applications and to drive commercialization, researchers have begun to shift their focus towards the development and optimization of solar modules.

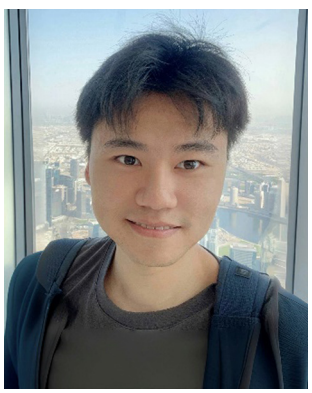

Bochun Kang

Bochun Kang joined Professor Yan's group in 2023 and is now pursuing his PhD degree in the Hong Kong Polytechnic University, Department of Applied Physics. His current research interests include scalable perovskite solar modules design and fabrication.

Feng Yan

Feng Yan is a Chair Professor at the Department of Applied Physics and the director of Research Center for Organic Electronics in the Hong Kong Polytechnic University. He received his PhD degree in Physics from Nanjing University. He worked at Engineering Department of Cambridge University in 2001 as a Research Associate and joined the Department of Applied Physics of The Hong Kong Polytechnic University in 2006. He is a Highly Cited Researcher identified by Clarivate from 2021 to 2024. He has research interests in organic electronics, thin-film transistors, biosensors, solar cells, 2D materials, and smart materials.

Since the diverse applications and fabrication processes of different-sized PSC devices, there is an urgent need for a standardized classification criterion to categorize module sizes and mitigate conflicting comparisons. The National Renewable Energy Laboratory (NREL) has proposed a universally applicable standard for module size classification, which finds wide application in various photovoltaic technologies such as Si and cadmium telluride (CdTe) solar modules.[34] In the champion photovoltaic module efficiency chart, NREL has classified modules larger than 200 cm^2 into distinct categories. Modules ranging from 200 to 800 cm^2 are designated as ''submodules'', while those spanning 800 to 6500 cm^2 fall under the classification of ''modules''. Modules with an area between 6500 and 14 000 cm^2 are identified as ''standard modules'', and modules exceeding 14 000 cm^2 are referred to as ''large modules''. NREL has chosen to disregard modules smaller than 200 cm^2 in their classification. Research findings indicate that large-scale modules are typically manufactured by commercial enterprises, whereas laboratory investigations predominantly focus on modules ranging from 10 to 100 cm^2. However, NREL's classification framework still necessitates complementary information to present a comprehensive categorization of modules. Encouragingly, Green *et al.*[35] have bridged this gap in their continually updated solar cell efficiency tables over three decades. They define modules ranging from 10 to 200 cm^2 as ''minimodules'', while modules smaller than 10 cm^2 are referred to as ''cells''. Over the years, outstanding performers have emerged in various fields, with some already transitioning to large-scale commercial production, which is a highly promising development. Table 1 provides a record of the outcomes from the different classification categories to date.

2.1.1 Device design. To mitigate the issue of charge losses in large-scale production, modular manufacturing can be implemented in either parallel or series configurations to alleviate this pressure.[40] In principle, the parallel configuration of PSMs yields an increased aggregate working current under voltage-stabilized benchmarks. As shown in Fig. 1a and b, the parallel PSMs exhibit an even dispersion of parallel metallic grids adjacent to individual cells, facilitating the collection and integration of current. The paramount merit of this architecture lies in its inherent fault tolerance. In the event of a malfunction in a single cell, the remaining sections continue to work normally, greatly enhancing robustness. However, the presence of metallic grids in parallel PSMs results in inevitable energy dissipation, predominantly attributed to the intrinsic grids resistive losses, the elevated contact resistance with transparent conducting oxide (TCO) and the declining utilization of effective area. These three factors severely curtail the advancement of PCE, impeding its widespread scalability.[40–42] Owing to these factors, the research on parallel PSMs have not garnered the same level of focal attentions as the series ones, leading to scarcity outputs dedicated to this field. Presently, the record is upheld by Chen *et al.*,[43] who achieved a remarkable PCE of 16.63% on an effective area of 20.77 cm^2 through perovskite precursor engineering utilizing the Lewis base additive diphenyl sulfoxide (DPSO) *via* slot-die coating.

In contrast, series-connected PSMs enhance the open-circuit voltage while maintaining a stable current, which thereby limit the total current passing through the TCO and enable a greater reduction of resistive losses. Consequently, the series connection is regarded as a more promising module industrialization strategy. Normally, series modularization for PSCs is commonly achieved through a built-in circuit established by a P1–P2–P3 scribing process. This can be rapidly accomplished within microseconds under laser irradiation.[45] This approach shows advantageous for large-scale batch production. The three-step sequential laser scribing process, the P1–P2–P3 interconnection process, is employed to achieve the formation of multiple interconnected independent PSCs for constructing a PSM, as depicted in Fig. 2c–e. Initially, the P1 laser scribing step is performed on the indium tin oxide (ITO) layer deposited on the glass substrate, creating isolated ITO substrates. Subsequently, in the P2 step, the entire structure is selectively removed before the top electrode is deposited, allowing the interconnection of individual cells through the deposition of the top electrode, resulting in a series-connected structure. Disparate from P1, the energy requirement for P2 is much higher depending on the material and the increase in thickness. P3 removes the top electrode with the assistance of laser, creating a conductive pathway eventually. It is noteworthy that the three scribing lines are required to be kept in strict geometrical parallel, preventing cells failure and leakage caused by the cross.[46] The distance from P1 to P3 (scribing lines included) called the 'dead area', which act as wires and does not make any

Table 1 Definition of different PSCs and PSMs sizes and record analysis in various classifications

Size (cm^2)	Combined criteria	PCE records (%)	Active area (cm^2)	Year	Stability description	Contributors	Ref.
≤1	Small cells	26.7	0.0519	2024	Undisclosed	University of Science and Technology of China	35
1–10	Cells						
10–200	Minimodules	23.30	27.22	2024	Decrease to 94.66% after 1000 h light soaking under room temperature	École Polytechnique Fédérale de Lausanne	20
200–800	Submodules	20.6	215.53	2024	Undisclosed	Korea Research Institute of Chemical Technology and Unitest	36
800–6500	Modules	20.7	810	2024	Pass IEC61215 IEC61730	Wuxi Utmolight Technology	37
6500–14 000	Standard modules	18.4	7200	2024	Undisclosed	Renshine Solar	38
>14 000	Large modules	19.04	20 000	2024	Undisclosed	Kunshan GCL Photoelectric Materials	39

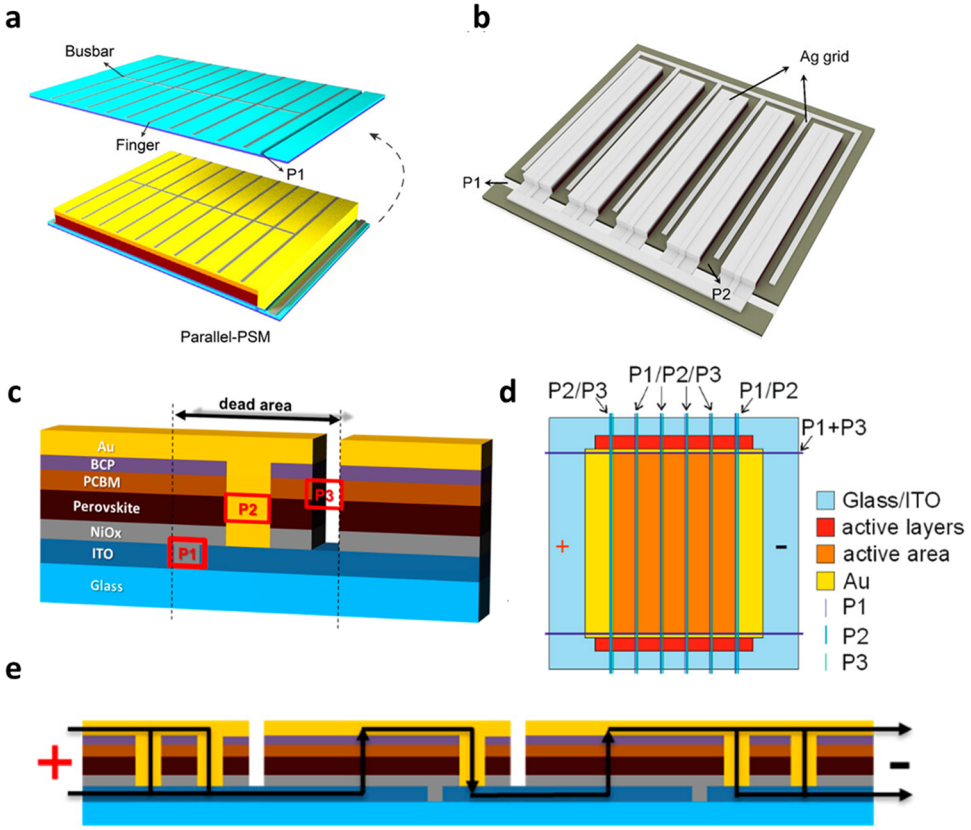

Fig. 1 (a) Architecture of the parallel PSMs.[40] Copyright 2021, Wiley-VCH GmbH. (b) Metallic grids on parallel PSMs.[43] Copyright 2021, American Association for the Advancement of Science. (c) P1–P2–P3 laser scribing on series PSMs. (d) The overall plane view and (e) the current flow path in the side view of the series PSMs.[44] Copyright 2020, MDPI, Basel, Switzerland.

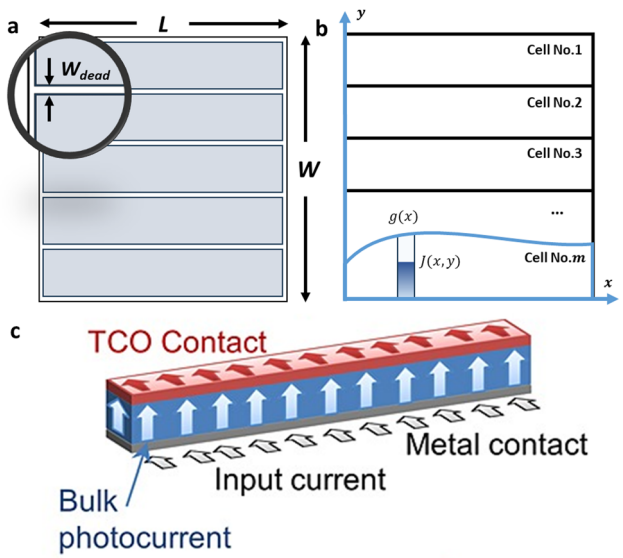

Fig. 2 (a) Schematic diagram of subcells distribution segment. (b) Current flow in one arbitrarily segment.[50] (c) Schematic of the vertical current flow received from the back bottom and collected from the edge of the TCO contact in subcells.[51] Copyright 2013, John Wiley & Sons, Ltd.

contributions to the photoelectric effects. In contrast to the ''dead zone'', the ''active region'' bears the responsibility for the entire power conversion process. These two zones together compose the aperture area. And the geometric fill factor (GFF), determined by the ratio of 'active area' and 'aperture area' is an essential parameter for describing the effectively utilized area of PSMs. GFF plays a pivotal role in PSMs, serving as a crucial determinant of the module's light utilization capacity and conversion efficiency per unit area. A higher GFF signifies an augmented capability of the module to harness sunlight effectively, thereby establishing a positive correlation with the reduction of 'dead area'. Simultaneously, it represents a paramount objective pursued in the development of PSMs scribing techniques.[44,47] Compared to traditional mask-based patterning, laser scribing technology has the capability to elevate the GFF from 50% to a stable level exceeding 90%.[48,49]

2.1.2 Numerical analysis of the subcells design. The modules in the literature are reported to have various sizes and shapes, however, how to proceed with quantitative analysis is an essential numerical theoretical issue to define the best shape. The fundamental basis for this analysis lies in the resistance loss. To achieve balanced load distribution among the subcells in a module, each subcell is typically designed with the same width (Fig. 2a). Suppose in the case of inconsistent subcells' widths, the variation in the active area will hinder the

performance of the PSMs due to the differences in current load between adjacent subcells.

The initial work is to determine the shapes. It is known from the published paper that high-performance PSMs are typically designed in a rectangular configuration. Here, we will analyze the reasons behind this design through numerical analysis.[50] Starting from the principle, under AM 1.5 solar illumination, the photovoltaic effect generates electron–hole pairs at each point distributed across the active area, resulting in a local current density. Subsequently, these electrons move vertically through the p–i–n junction and reach the top electrode edge to enter the series circuit loop as shown in Fig. 2c. Assuming that the subcell's length is the same as the module's length L, the area of every single subcell A can be illustrated as:

$$A = A_{\text{active}}/m = \int_0^L g(x)\mathrm{d}x \tag{1}$$

where A_{active} is the active area, m is the number of subcells and $g(x)$ is defined as the width of a single cell as a function of x in the L direction (Fig. 2b). Here, Alam *et al.*[50] assumed that $g(x)$ is expressed as:

$$g(x) = (n+1)A^{xn}/L^{n+1} \tag{2}$$

which ensures that the cell area is preserved for all exponent n so that the amount of sunlight absorption is the same. Building on this, the total power loss of a single subcell, P_{loss}, is a monotonically increasing function with respect to n ($n > 0$). This implies that when $n = 0$, the shape of the subcell corresponds to the rectangles with the lowest P_{loss}, making it the most ideal subcells geometry.

The subsequent task behind is to ascertain the ideal number of subcells within the fixed module width W. We supposing that the module is divided into m subcells, the $m - 1$ scribings are required to complete the module fabrication. The total output power P_{out} within the module can be approximated as a compensation relationship between the power of a unscribed perfect device P_{ideal}, P_{loss} and the scribing power loss P_{scribing} as follows:

$$\begin{aligned} P_{\text{out}} &= \left(\frac{J_{\text{sc}}}{m}\right)\cdot(mV_{\text{oc}})\cdot \text{FF} \\ &= P_{\text{ideal}} - mP_{\text{loss}} - (m-1)P_{\text{scribing}} \end{aligned} \tag{3}$$

$$P_{\text{scribing}} = \frac{L_{\text{dead}}}{A_{\text{active}}}P_{\text{out}} \tag{4}$$

where J_{sc} is the short-circuit current density, V_{oc} is the open-circuit voltage, FF is the fill factor, and W_{dead} is the width of the dead area. Combined with the series circuits law we find that P_{out} independ of the number m. Also at the same scale of the W and L, P_{ideal} is fixed. Thus, the value of m turns out to be completely dependent on the resistive contribution of the subcells. Ideally, PSMs have $W_{\text{dead}} \ll W$, at which it can be assumed that $P_{\text{out}} \to P_{\text{ideal}}$, P_{loss} and P_{scribing} is negligible. To summarize, the amount of m can be considered as a function, whose key determining factors within this relationship are the current density and the PCE, which is proportional to the ratio of P_{out} to A_{active}. On the other hand, the current density is influenced by the bandgap of the perovskite materials. Consequently, for various perovskite precursor systems, the module size needs to be recalculated to achieve the optimal arrangement structure. As a result, we can conclude that the number is directly proportional to the current density and inversely proportional to the materials' bandgap and efficiency. Currently, several solar module design software such as SETFOS and LAOSS provide rapid structural aids.[52,53] Apart from the investigation of the distribution expansion in terms of the L scale, researchers have also examined the design of the W scale length to ensure the attainment of optimal efficiency in PSMs. Gao *et al.*[54] tested cells ranging from 5–35 mm in length based on a fixed width of 2 mm. They discovered a pattern of increasing and then decreasing efficiency in the PSCs, with the best optimal PCE achieved at a length of 10 mm. The J_{sc} exhibited a decreasing trend with the incase of the length, while the V_{oc} showed an increasing trend.

2.1.3 Modularization process. The establishment of PSMs starts with the large-area deposition of functional layers. The specific implementation methods can be divided into two categories. One is based on solvent methods, such as spin coating, blade coating, screen printing, and slot-die. One type is based on dry coatings, such as electrospraying, PVD and CVD. Precursor materials and solvents such as dimethyl formamide (DMF)/dimethyl sulfoxide (DMSO)[20] and highly volatile acetonitrile (ACN)[21] have been proven effective in manufacturing large-area PSMs during the cell-to-module process. Therefore, the key lies in the optimization of processing techniques and parameters.

Laser scribing is undoubtedly the most widely used technology in the module process. Functional materials can be vaporized through high-intensity lasers in an instant by absorbing laser photons.[55–57] By taking advantage of the different absorption ranges of materials for wavelength, selective removal of materials can be achieved. Longer durations of laser pulses lead to higher energy output, resulting in a larger thermal impact zone. However, if the laser power is too high or the pulse frequency is not appropriate, it may lead to excessive damage to the perovskite layer or other functional layers, even causing burnout, thereby increasing the reject rate and lowering manufacturing yield. This also corresponds to higher process improvement costs. Generally, the smaller laser processing area in the PSMs, the larger GFF, indicating higher light utilization efficiency. Therefore, picosecond and femtosecond lasers have greater advantages compared to nanosecond lasers. Huang *et al.*[57] performed dead area optimization, reducing the dead zone to 70 μm with the assistance of a picosecond laser, resulting in a GFF of 99%. Apart from laser scribing, another common scribing method is mechanical scribing.[58] Unfortunately, mechanical scribing is a relatively unstable scribing process. During the P2 and P3 stages, excessive stress during mechanical scribing can cause damage to the bottom TCO, resulting in poor contact between the top metal electrode and TCO. This increases the series resistance of the device and leads to a decrease in the device's FF and GFF. Additionally, during the P3 stage, there is a risk of directly pressing the top metal electrode onto the TCO during mechanical scribing,

which can result in a short circuit in the device. Unidirectional scribing can also lead to the accumulation of detached material at the trailing end along the direction of motion, causing serious defects. However, the energy saving of the mechanical one has also attracted the attention of the industry. For both scribing methods, the issue of electrode peeling after the P3 stage is unavoidable. The integrated dust removal functionalities have been developed to effectively alleviate this problem. Interestingly, it has been demonstrated that beyond the process itself, the design of scribing patterns can also enhance the performance of PSMs. Rakocevic and colleagues[59] have innovatively designed a module with a point-contact configuration, achieving an enhancement in GFF from 95% to 99% as well. The record of GFF was broken by Carlo *et al.*,[60] reaching a remarkable 99.6% improvement. They designed an unconventional discontinuous P2 pattern that miraculously reduced the dead area from a small size of 45 μm to an incredible limit of the average of 19.5 μm (Fig. 3a–c). And they proved the feasibility of a PCE of 20.7% on a miniature size of 2.6 cm^2. Hence, the choice of the final commercial modularization process should be a decision that respects both production yield requirements and manufacturing costs. This is dependent on multiple constraining factors. For instance, opting for laser scribing implies substantial energy consumption, while enhancing precision using shorter pulse widths results in slower production efficiency.

It is worth noting that the process inhomogeneities may have a negative impact on the PSMs in the cell-to-module fabrications. Especially in perovskite materials, their soft lattice structure makes them prone to deformation and aging. The presence of functional thin film defects in the layered structure of PSCs can lead to the exposure of the perovskite layer. When the perovskite material overflows or encounters the top electrode, irreversible reactions may occur, resulting in device damage. To address this issue, thin insulating layers such as bathocuproine (BCP)[63] are used for longitudinal protection. These protective layers can be deposited above the perovskite layer, preventing its exposure to the external environment and thereby improving the device's lifespan. However, merely controlling the vertical diffusion is not sufficient to ensure the stability of PSMs. The severe lateral exposure in the cross-sectional area caused by laser scribing becomes a specific issue for PSMs. In the P2 and P3 layers, this leads to direct contact between perovskite materials and the external environment. Although subsequent encapsulation can isolate the environment, it cannot completely prevent stability losses caused by ion migration. Therefore, several efficacious strategies for lateral protection have been investigated. Mai *et al.*[61] used ozone (O_3) treatment to obtain PbO_x at the cross-section, innovatively providing a solution to block lateral diffusion, while protecting P2 and P3, greatly reducing leakage caused by burrs generated by metal electrodes in laser scribing, and improving efficiency as shown in Fig. 3d. Additionally, low-dimensional diffusion barriers (DBL) were demonstrated by Han *et al.*[62] as excellent lateral protection measures, increasing the potential barrier for ion diffusion as illustrated in Fig. 3e. The experiments illustrated that two-dimensional graphitic carbon nitride (g-C_3N_4) effectively inhibits the lateral migration of iodide by reducing it by a factor of 10^3–10^7. These modules achieved a stable PCE exceeding 15% for over 1000 hours under 85 °C.

2.2 Flexible/semitransparent solar modules

For catering to achieve broader commercial application scenarios such as building integrated photovoltaics (BIPV), researchers are developing a range of attractive module solutions, especially focusing on enhancing flexibility and transparency. The flexible PSMs (F-PSMs) are an emerging solar technology

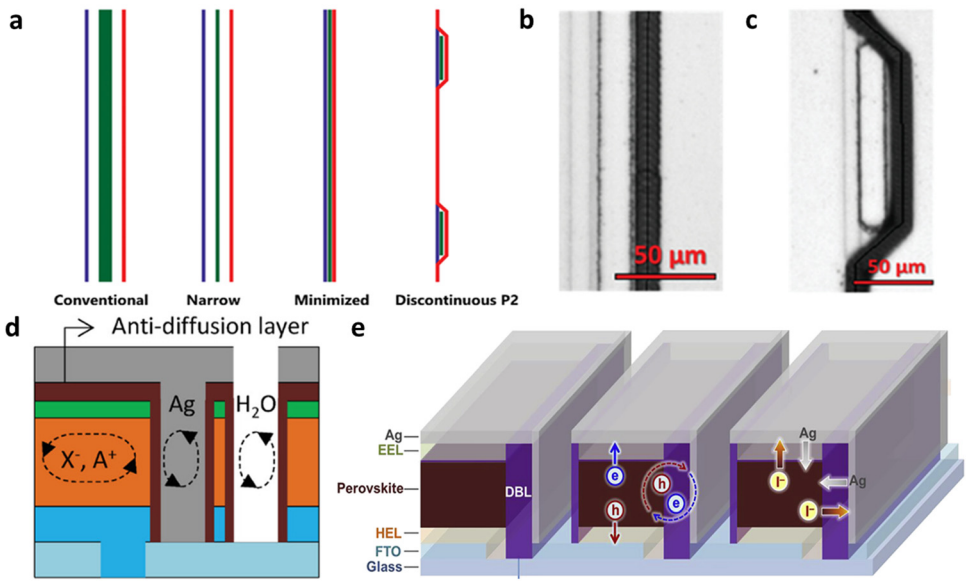

Fig. 3 (a) Schematic diagram of conventional, narrow, minimized and discontinuous laser scribing designs. (b) Scanning electron microscope (SEM) figures of minimized and (c) discontinuous P2 interconnection.[60] Copyright 2024, Wiley-VCH GmbH. (d) Anti-diffusion layer treated by O_3.[61] Copyright 2023, Wiley-VCH GmbH. (e) DBL for blocking lateral diffusion.[62] Copyright 2019, Elsevier Inc.

that has demonstrated a significant efficiency increase to 18.84%.[64] A flexible substrate is a critical component of the F-PSM, providing a flexible support structure for the perovskite material. These substrates can be made of flexible plastics, films, or fiber materials, enabling the solar module to have characteristics such as lightweight, bendable, and customizable properties, usually polyethylene terephthalate (PET) and polyethylene naphthalate (PEN). However, the primary challenges of this technology involve designing efficient flexible electrodes and ensuring the bending stability of device structures and materials. From the perspective of large-scale production, flexible substrates often present challenges in achieving high-quality perovskite crystallization due to their relatively rough surfaces. During annealing, uneven thermal conduction and the presence of solvent trapped in substrate crevices in air-assisted coating processes can exacerbate this issue. The evaporation of retained solvent can lead to a significant number of defects at the grain boundaries.[65] Gao *et al.*[66] took inspiration from tendons and incorporated supramolecular poly(dimethylsiloxane) polyurethane materials with self-healing properties, resulting in a significant enhancement in the bending durability of F-PSMs. Even after undergoing 8000 bending cycles, the F-PSMs retained 80% of their initial efficiency. Meng *et al.*[67] introduced glue-like poly(3,4-ethylenedioxythiophene):poly(ethylene-*co*-vinyl acetate) (PEDOT:EVA) as HTL, which lent its strong cohesion as shown in Fig. 4a to obtain 17.55% PCE on 31.20 cm^2 and maintained 85% of the initial efficiency after 7000 mechanical bends.

Additionally, semi-transparent PSMs (ST-PSMs) are considered a significant research direction due to their effective photovoltaic conversion while maintaining high visible light transparency, meeting both architectural aesthetics and functional requirements. Since the light absorption capacity and photoelectric conversion capacity of perovskite are mutually restricted, how to balance PCE and average visible transmittance (AVT) becomes thought-worthy. In 2014, Eperon *et al.*[71] first proposed semi-transparent PSCs, which triggered extensive subsequent research. Compared with traditional PSMs, the key technologies of ST-PSMs lie in the transparent top electrode and the preparation of high-quality semi-transparent perovskite films. Typically, transparent electrodes include TCO,[72] ultra-thin metal electrodes,[73] dielectric/metal/dielectric multilayer electrodes,[74] *etc.* Normally, the method for depositing the top transparent electrode is magnetron sputtering, but this technique frequently causes damage to the exposed substrate layer. To mitigate this Magliano *et al.*[75] incorporated a vanadium oxide protective buffer layer, resulting in an efficiency of 15.7% over an area of 1 cm^2, while preserving the AVT of 42%. The conductivity of these materials is generally lower than that of opaque materials, and they also lose the ability to reflect unabsorbed photons, allowing the perovskite layer to engage in secondary absorption. Another critical constraint on transparency is the composition and thickness of the perovskite. The size of the halide ions in the perovskite determines its bandgap; as the radius of the halide ions decreases, the bandgap of the perovskite widens, thereby increasing the visible light transmission region. Typically, an increase in bromide content leads to a noticeable enhancement in transparency. Additionally, employing diluted solvent concentrations to reduce the thickness of the perovskite layer can more effectively increase the AVT, as illustrated in Fig. 4b. Differently, a recent research proposed a method to achieve visual transparency without the conventional increase in AVT. This approach leverages the optical properties of human eyes. Yoo *et al.*[69] utilized laser cutting to create micro-patterns with varying densities on the non-wavelength-selective PSMs. As shown in Fig. 4c, they achieved 32% AVT and 9.0% PCE over an aperture area of 4 cm^2.

According to empirical investigations, diverse thin film coating processes exhibit disparate levels of selectivity and compatibility within distinct functional layers, each presenting unique merits and drawbacks. To facilitate expedited industrial manufacturing, the amalgamation of multiple technologies is imperative. For instance, realizing highly efficient and economically viable roll-to-roll (R2R) ideal production paradigms is a culmination of the synergistic integration of various methodologies. For example, Weerasinghe and colleagues[70] achieved sustainable production of 11% efficient F-PSMs using an R2R process in an ambient environment. In this process, the ETL was applied using gravure printing, while the perovskite and HTL layers were coated through slot-die coating with air-knife assist. The top carbon electrode was coated using screen printing. As a trend for future development, this highly integrated mode, leveraging the strengths of each process (Fig. 4d), has led to breakthroughs in the final device, offering possibilities for the realization of rapid flow in industrial-scale production.

3. Large-scale perovskite deposition methods

3.1 Meniscus-based perovskite fabrication processes

3.1.1 Theoretical modeling of fluid mechanics. The current research focus and highest expectations for the fabrication methods of large-area PSMs lie in blade coating and slot-die coating. The benefits of these two methods for coating from a linear to a planar shape are found in their ability to effectively control the quality, thickness, and consistency of the liquid film. Theoretically, the fundamental reason for this coating controllability is attributed to the fluidic mechanics of meniscus structures.[76] During the coating process, the solution is trapped between the substrate and the coating head, forming a concave meniscus maintained by capillary force. A curved liquid–air interface, known as the meniscus, naturally forms near the edge of the coating head and extends towards the substrate. According to the move direction, the meniscus is divided into an advancing meniscus and a receding meniscus. Generally, the receding meniscus plays a more decisive role. During the coating process, the relative motion of the head creates a shearing force on the precursor solution filling the space between the head and the substrate and initiates a Couette flow as shown in Fig. 5a.[77] The pressure difference between the two meniscus affects the magnitude and direction of this flow. Levich and Landau[78] were the first to analyze the flow characteristics of fluids under the motion of a plate in terms of fluid mechanics and established the Levich–Landau regime (Fig. 5b). The viscous forces act as the dominant

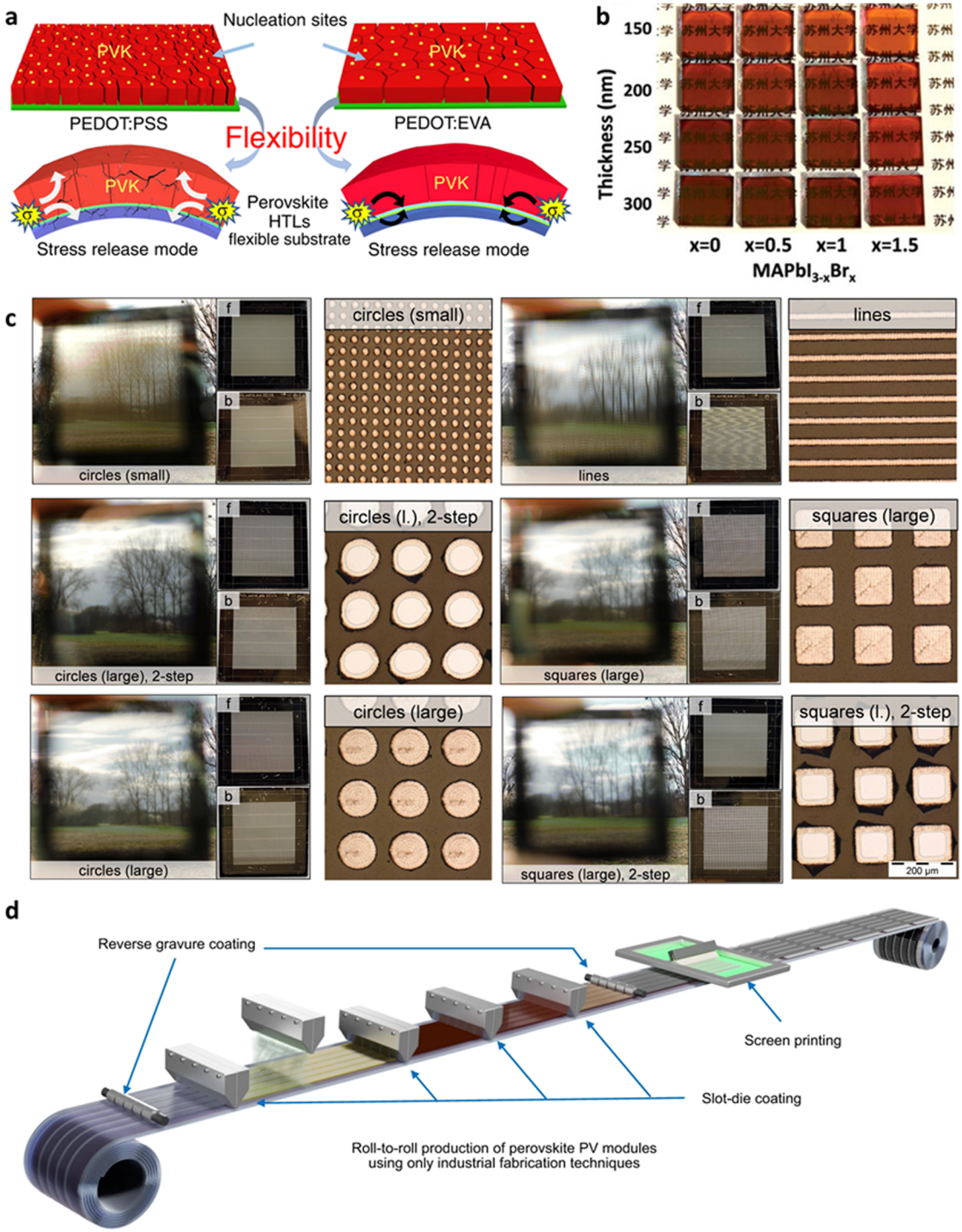

Fig. 4 (a) Schematic diagram of PEDOT:EVA stress relief.[67] (b) Transmittance changes with the amount of Br and the perovskite thickness.[68] (c) Transparency effect under different laser patterns.[69] (d) Schematic diagram of the large-scale R2R PSMs production process with the help of multi-process collaboration.[70]

affect factor in this regime. The viscous forces become strong enough under high coating speed to drag a liquid film out of the meniscus. The liquid thickness t_{wet} is given by:

$$t_{wet} = 0.94\kappa^{-1}\mathrm{Ca}^{2/3} = 0.94\frac{\gamma^{1/3}}{\rho g^{1/2}}(\mu v)^{2/3} \quad (5)$$

where the thickness t_{wet} is related to the surface tension γ, density ρ, dynamic viscosity μ, the gravitational acceleration g and board moving speed v. In these calculations $\mathrm{Ca} = \mu v/\gamma$ is capillary number and $\kappa^{-1} = \rho g^{1/2}/\gamma$ presents the capillary length. The prerequisite for applying the Levich–Landau regime above depends on a higher coating speed, and drying timescales are

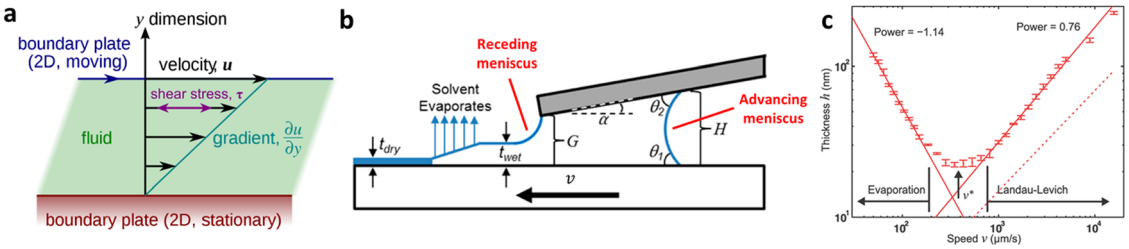

Fig. 5 (a) Schematic diagram of fluid dynamics of the meniscus coating process. (b) Schematics of the functions relationships between speed and perovskite thickness under evaporation and Landau–Levich regimes.[80] (c) Measured film thickness h as a function of deposition speed v.[79] Copyright 2009, American Chemical Society.

comparable to movement speeds. Under the low speeds situation, the fluid obeys evaporation mode which lead the liquid film adhere directly to the blade instead of substrate. The gradually accumulating barriers will disrupt the stability of receding meniscus and hinder the film formation. Le Berre *et al.*[79] firstly discuss the two regimes' speed critical point (Fig. 5c). They proved that the two regimes have blanket relationships $t_{wet} \propto v^{\alpha}$, α is a constant which equals -1 and 2/3 respectively for evaporation and Levich–Landau regimes. Subsequently, Huang's team[30] applied and verified its feasibility in perovskite precursors. Under the assumption of negligible evaporation during blade coating, and evaporate fast after the wet film formation, Le Berre *et al.* developed the blade coating model based on the lubrication approximation within the Levich–Landau regime building upon the research on polymer thin films. They envisaged that the meniscus coated wet film thickness is affected by the geometry of the solution contact process, the relationship is given by:

$$t_{wet} = 1.34\frac{C}{\rho}\frac{H}{\cos\theta_1 + \cos\theta_2 - \frac{H^2}{2\kappa^{-2}}}\mathrm{Ca}^{2/3} \quad (6)$$

where C is the geometric parameter curvature, H is the height of the advancing meniscus, θ_1 and θ_2 are the contact angles between the advancing meniscus and the substrate and the blade, respectively. Beyond this work, Davis and colleagues[80] introduced a solvent evaporation approach to receding meniscus, replenishing the mathematical relationship between dry film thickness t_{dry} and t_{wet} as follow:

$$\frac{t_{dry}}{t_{wet}} = \frac{\frac{w_{solute}}{\rho_{solute}}}{\frac{w_{solute}}{\rho_{solute}} + \frac{w_{solvent}}{\rho_{solvent}}} \quad (7)$$

where ρ_{solute}, w_{solute}, $\rho_{solvent}$, $w_{solvent}$ are density ρ and mass fraction w of solute and solvent. Two commonly employed coating techniques that are in line with this theory are blade coating and slot-die coating. In the following discussion, we will explore the characteristics and advancements of these two processes.

3.1.2 Crystal growth dynamics by solution process. The performance of perovskite photovoltaic devices relies heavily on the quality of the light-absorbing layer, known as the perovskite thin film. A well-developed crystalline structure in this film plays a crucial role by increasing grain size, and reducing the formation of defects and the number of grain boundaries, thereby minimizing the detrimental effects of non-radiative recombination. Achieving an ideal perovskite thin film requires a research approach that stems from the principles of crystal growth kinetics, in order to devise effective strategies for improvement.[81] By following the LaMer crystal growth mechanisms, the crystallization process of perovskite films unfolds in a series of three distinct steps: starting from the precursor state, transitioning into nucleation, and culminating in crystal growth. Initially, the evaporation of the solvent in the precursor induces the entire system to reach an oversaturated and unstable state, thereby triggering the onset of crystallization. Let us direct our attention to the microscopic nucleus. Building upon the classical theories proposed by Volmer,[82] Becker–Döring,[83] the nucleus is considered to be a condensed phase in the form of a sphere. Assuming uniform nucleation, the thermodynamically defined free energy, $\Delta G(r)$ is closely related to the radius r, of the nucleus. Their relationship can be expressed as:

$$\Delta G(r) = 4\pi r^2\gamma + \frac{4}{3}\pi r^3\Delta G_v \quad (8)$$

$$\Delta G_v = -\frac{RT\ln S}{\tilde{V}} \quad (9)$$

where γ represents the surface free energy and ΔG_v denotes the difference in free energy before and after nucleation, which is determined by the degree of supersaturation S, molar volume $\tilde{V}$, temperature T and the ideal gas constant R. By combining the positive surface free energy term ($4\pi r^2\gamma$) and the negative bulk free energy term ($4/3\pi r^2\Delta G_v$), their relationship is graphically depicted (Fig. 6a). From the plot of the $\Delta G(r)$ function, a distinct nucleation critical size, r_c, can be observed. When the crystal nucleus size is smaller than r_c, re-dissolution phenomena occur, leading to a decrease in $\Delta G(r)$. Conversely, when the nucleus size exceeds r_c, the crystal nucleus continues to grow. In this context, the competition between cluster nucleation and growth determines the cluster size. The nucleation rate J, can then be expressed as a Boltzmann-type Arrhenius expression as follows:

$$J = A\exp\left(-\frac{\Delta G_N}{kT}\right) = A\exp\left(-\frac{16\pi\gamma^3\tilde{V}^2}{3k^3T^3(\ln S)^2}\right) \quad (10)$$

where A is the kinetic prefactor which is predominantly influenced by the rate at which vapor molecules strike and the effective surface area involved in this interaction, k is the Boltzmann constant. Due to the energy potential barrier ΔG_N,

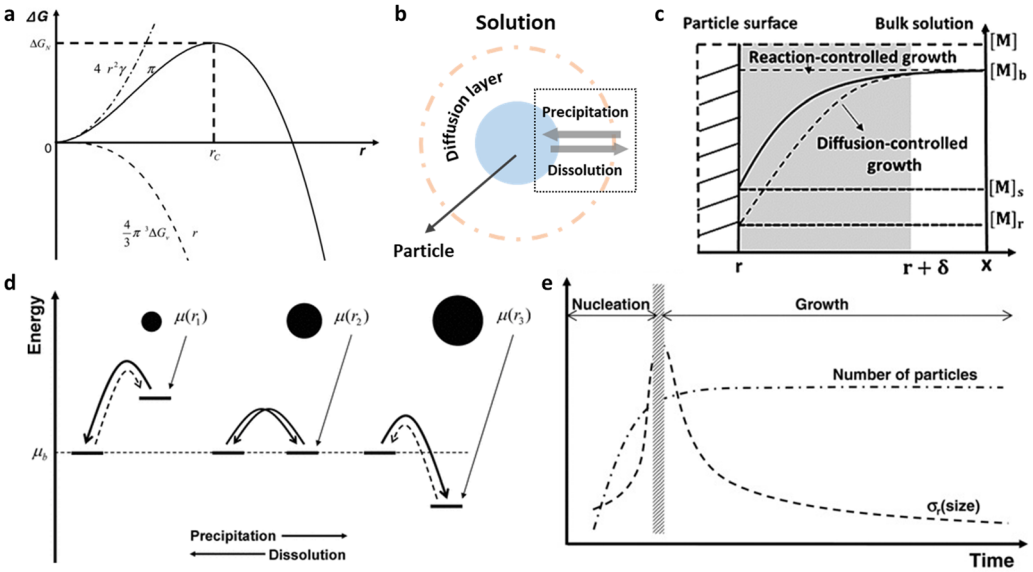

Fig. 6 (a) Plots for the relationship between crystallization free energy and particle radius. (b) Schematic illustration of the diffusion region around the spherical particle and (c) the plot of monomer concentration [*M*] as a function of distance *x* under reaction and diffusion-controlled situation. (d) Schematic diagrams of the chemical potential level shifts of particles with disparate size. (e) Plots of the relationship between the number of particles from nucleation to growth and σ_r of the size distribution.[81] Copyright 2011, WILEY-VCH Verlag GmbH & Co. KGaA, Weinheim.

the supersaturation level for homogeneous nucleation is usually much higher than that for colloidal particle growth. The presence of a uniform nucleation energy barrier is crucial for controlling the distribution of size in the synthesis of nanocrystal colloid. After nucleation, the crystals enter the growth stage, which is a diffusion process following Fick's diffusion law. The process of monomer diffusion to the particle surface and the relationship between monomer concentration [M] and position can be observed in Fig. 6b and c.

This process remains closely related to the particle size and is primarily influenced by solubility. From a morphological perspective, both small and large particles reach the same size at the end of the growth period. This indicates that smaller particles have a higher growth rate. Theoretically, according to the Gibbs–Thomson relationship, when particles are too small, the chemical potential of their monomers is lower than that of the monomers in the solution. This favors the dissolution of solute particles in Ostwald ripening, leading to larger average crystalline sizes (Fig. 6d). The growth rate which is determined by radius r and time t can be expressed as:

$$\frac{dr}{dt} = \frac{D\tilde{V}([M]_b - [M]_r)}{r - D/k} \quad (11)$$

where $[M]_b$ and $[M]_r$ represent the bulk concentration of the solution and the solubility of the spherical particle of radius r, respectively, k is the reaction constant, and D is the diffusion rate. Here, the Damköhler criterion $RTD/2\gamma\tilde{V}k$ can be used to determine whether diffusion or reaction is the main factor in the growth process. Overall, throughout the nucleation and growth process, the average size of the particles and the relative standard deviation σ_r of the size distribution slowly increase. In the later stages of Ostwald ripening, the size distribution of the particles reaches a stable state, where the average size is primarily determined by the surface free energy as shown in Fig. 6e. This provides a theoretical basis for the high-quality growth of the perovskite layer.

3.1.3 Blade coating technology. Blade coating technology, by virtue of its simplicity, raw material savings (usage is about 10% of conventional spin coating), low equipment requirements, scalability, area adjustability has been widely studied and favored for application in large-scale production.[18,21,84,85] In 2000, Padinger *et al.*[86] pioneered the first application of the blade coating approach to solar cells and coated with an active layer consisting of Poly[2-methoxy-5-(3′,7′-dimethyloctyloxy)-1,4-phenylenevinylene] (MDMO-PPV) mixed with C_{60} to obtain effective organic solar cells devices. With the iterative development of solar cells afterward, the blade coating process has also been utilized in the large-scale production of copper indium gallium selenide (CIGS) solar cells,[87,88] dye-sensitized solar cells (DSSC),[89–91] and organic solar cells (OSC).[92,93] In PSC, the application of blade coating has seen an explosive and massive exploration since it was first published by Jen's team[94] in 2014 to enhance environmental stability. As of now, Huang and his colleagues[95] keep the lead, achieving a champion PCE of 24.6% on a 0.08 cm^2 p–i–n structure PSC and an NREL-certified PCE of 21.8% on a 26.9 cm^2 module.

In the typical blade coating process, the precursors are dripped parallel to the doctor blade or the gap between the doctor blade and the glass, where it is spread uniformly using the liquid's surface tension. Subsequently, the blade moves relatively to the substrate and drags the solution onto the substrate to form a uniform film. Based on the fluid mechanics theory discussed at the beginning of this chapter, it has been determined that the coating speed and the distance between

the blade and the substrate play decisive roles in the thickness of the film. However, when it comes to the quality and uniformity of crystallization, there is still a lack of quantitative control. Under constant velocity conditions, as the film coating progresses, the amount of perovskite precursor stored within the gap decreases. This significantly leads to uneven film thickness caused by meniscus deformation. In addition, the property of the content of precursor storage in blade gap can limit its development in terms of film expandability. In 2015, Tsai *et al.*[96] proposed a coating method with constant acceleration, increasing the uniformity under the acceleration of 6 mm s^{-2} (Fig. 7a). For the same principle, uniformly accelerated variation of the distance of the blade head from the substrate may be a worthwhile option to explore for guiding high quality films. There are still no attempts in this process. In addition, higher speeds lead to severe viscous resistance exerted on the meniscus, resulting in higher solution consumption, thickness gradients along the coating direction, and prolonged drying time.[79,97] Therefore, several strategies have been developed to reduce the viscosity of precursor solutions. The alteration of solvents can condition the viscosity, and Zhuang *et al.*[21] adjusted the high-evaporation solvent ACN in the blade-coated bromide surface modifier and perovskite precursor (Fig. 7b), resulting in the preparation of PSCs with an efficiency exceeding 24%. Moreover, in 2018, Deng *et al.*[30] introduced trace amounts of the surfactant L-α-phosphatidylcholine (LP) into the precursor solution. This approach modulated the fluid drying kinetics of the $MAPbI_3$ precursor where MA is methylammonium and increased the adhesion of the perovskite ink to the underlying non-wetting charge transport layer. This strategy enabled them to achieve a PCE of around 15% with an effective area exceeding 50 cm^2. LP subsequently emerged as a widely influential pre-additive surfactant. Furthermore, temperature and the volume of the added solution are also important controllable parameters. Arun *et al.*[98] conducted temperature control on the doctor blade and explored the different effects of substrate temperature, solution volume, and speed parameters on the crystalline morphology (Fig. 7c and d). The early-stage process exploration of this system discovered that the size of perovskite islands increases with the increase in solution volume and substrate temperature. Overall, the effects of these parameters are based on the hydrodynamic tuning of the Levich–Landau regime, a quest to achieve an optimal balance between the equipment and the fluid flow characteristics.

3.1.4 Slot-die coating. In the slot-die coating process, the liquid material is contained in a reservoir and is fed into a narrow slot or channel within the die head. The die head is positioned above the substrate, and a small gap is maintained between the die head and the substrate surface. As the liquid flows through the slot, a meniscus is formed at the exit of the die head. The liquid coating material is then pulled down onto the substrate either through capillary action or by controlling the pressure difference, resulting in the deposition of a thin and uniform film (Fig. 8a and b).[99] Unlike blade coating, slot-die coating utilizes a continuous liquid supply system, allowing for precise control of the solution volume within the gap by adjusting the liquid drawing rate, which ensures high uniformity in the thickness of the perovskite film by accurately controlling the amount of solution delivered. The thickness and quality are determined by the supply and demand relationships between solution coating and extrusion. Slot-die coating was first introduced by Vak *et al.*[100] to perovskite photovoltaic devices in 2014 with a PCE of 4.57% on over 45 cm^2. Subsequently, Cai *et al.*[101] pioneered the fabrication of PSMs using $MAPbI_3$ as the material, achieving a PCE of 10.6% on an active area of 17.6 cm^2. These

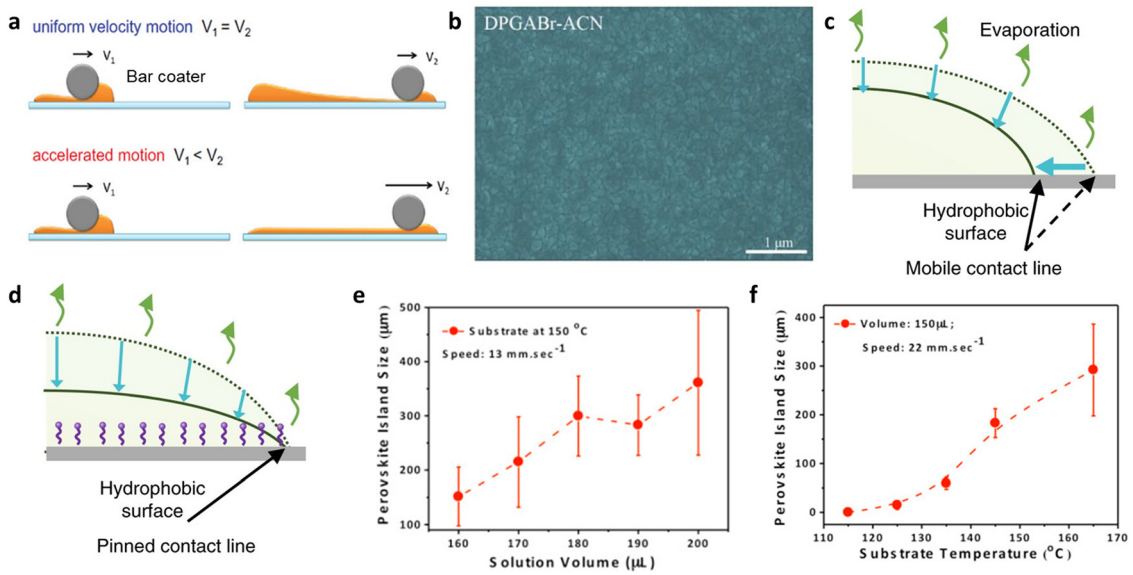

Fig. 7 (a) Schematic diagram of bar coating with constant speed and constant acceleration.[96] Copyright 2015, Elsevier B.V. All rights reserved. (b) SEM of surface reconstructed $MA_{0.7}FA_{0.3}PbI_3$ perovskite film.[21] (c) Schematics of the shrinkage of the ink droplet drying on a hydrophobic substrate without LP and (d) the pinning effect with LP.[30] Copyright 2018, Springer Nature. (e) Plots of the perovskite island size variation with the solution volume and (f) substrate temperature.[98] Copyright 2016, Elsevier.

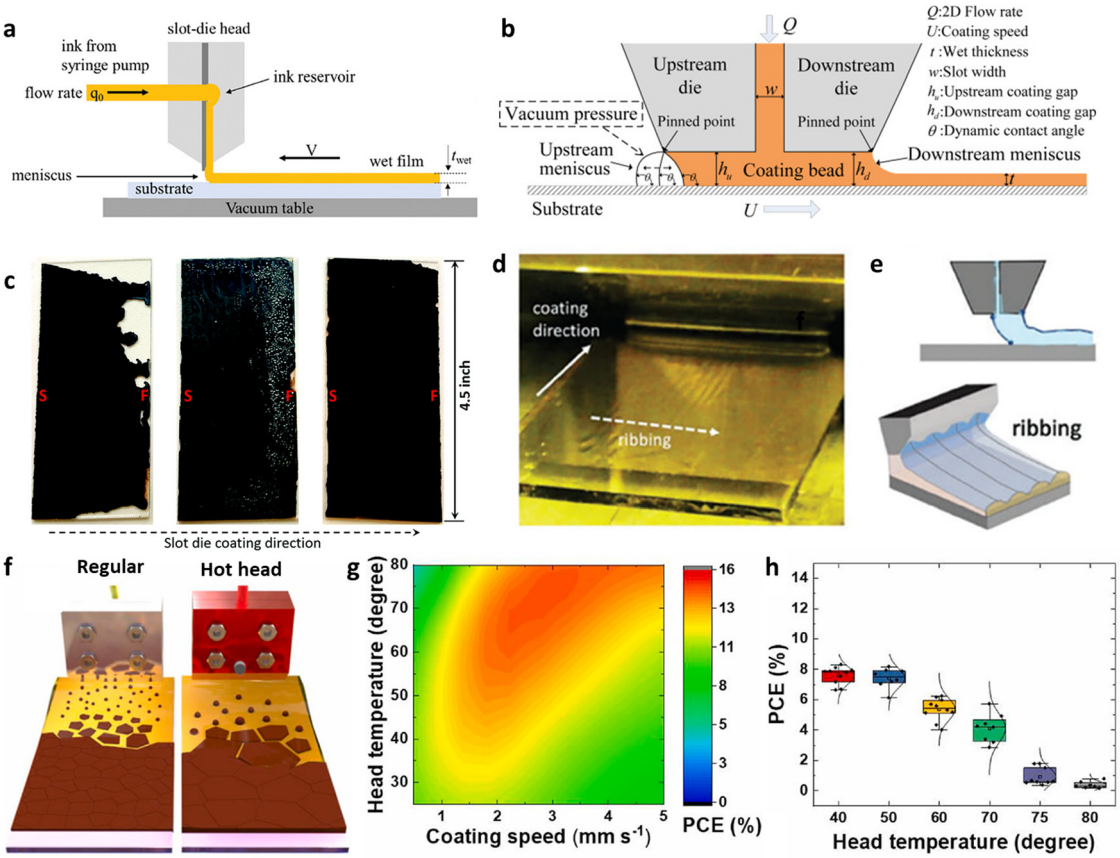

Fig. 8 (a) Schematic diagram of the slot-die coating equipment.[99] Copyright 2024, Wiley-VCH GmbH. (b) Schematic diagram fluid mechanics models and core parameters in slot-die coating.[103] Copyright 2016, American Institute of Chemical Engineers. (c) Images of slot-die coated perovskite thin films under different combination of ink supply rate and coating speed. From left to right: too fast, too slow and balanced supply.[104] (d) The image and (e) schematic illustrations of ribbing defects during slot-die coating.[99] Copyright 2024, Wiley-VCH GmbH. (f) Schematic diagram of slot die coating of perovskite films using 150 °C substrate-heating (left) and 150 °C substrate-heating/75 °C substrate-heating (right). (g) Color map of PCEs at the different head temperatures *versus* slot-die coating speeds. (h) Only-head heating with various temperatures.[105] Copyright 2022, Elsevier B.V.

pioneers have led the flourishing development of slot-die coating in perovskite photovoltaic devices. The current record for the highest slot-die-coated PSMs is held by Rana *et al.*[102] designed a organic molecular passivation strategy, which achieved 19.28% minimodule on a limited area of 58.5 cm^2.

From the perspective of process parameters, both slot-die coating and blade coating belong to the meniscus coating model, sharing fundamental process parameters. However, due to the slot-die mode, the precursor flow rate, or the injection rate, becomes an additional influential parameter in slot-die coating. Its matching with the motion speed of the slot-die is a key approach to addressing film formation defects. It is worth noting that it is a double-edged sword as it provides a more sustained solution supply, but the liquid reservoir in the slot-die introduces complex and unpredictable fluid changes in the meniscus. In this regard, Ding *et al.*[103] systematically discussed the causes of defects in slot-die processes. They identified five defect formation mechanisms. Firstly, a too low solvent injection flow rate affects the minimum wet film thickness, leading to the rupture of the receding meniscus and the formation of an incomplete film (Fig. 8c). Additionally, imbalances in dynamic wetting, such as interruptions during the coating process, result in film discontinuity. The introduction of bubbles during liquid reservoir injection creates bubble-related voids within the wet film and uncoated areas of the substrate. Exceeding speed limitations causes ink to gradually accumulate on the coating head and leads to loss of pre-measured and expected film thickness. Lastly, the mismatch of vacuum pressure results in the appearance of ribbings (Fig. 8d and e). These four defects are all caused by variations in the advancing meniscus.[99] In addition, they designed a different coating head to try to widen the machining window and eliminate defects caused by meniscus variations. In 2021, Zimmermann *et al.*[106] explored a two-step sequential deposition process to achieve precise control over the porosity of lead-based intermediates for optimal perovskite conversion efficiency. They successfully obtained a uniform perovskite layer with an area of 5 × 10 cm^2. Furthermore, they achieved an efficiency of 15.2% on an effective area of 12 cm^2.

Similar to blade coating, slot-die coating also lacks the crystallization driving force inherent in traditional spin coating. Therefore, additional quenching assistance is necessary.[107] The volatility rate of the solvent is crucial for the quality of perovskite thin films. Rapid solvent evaporation may result in defects in the film, such as pinholes or cracks, while slow

solvent evaporation can lead to incomplete crystallization of the film, affecting device performance. The crystallization assistance process following film coating is discussed in detail in Section 3.1.5 including methods such as air-knife and fast-vacuum-assisted flash evaporation. Furthermore, the unique structural characteristics of slot-die coating allow for more intriguing approaches to crystallization assistance, such as utilizing the synergistic heating of the slot-die head and substrate to facilitate crystallization (Fig. 8f). This method effectively suppresses the coffee-ring effect and enhances crystallization quality. A temperature-adjustable slot-die head was designed by Seo *et al.*[105] under the heating condition of 75 °C, together with the substrate environment of 150 °C (Fig. 8g), they used a one-step method to prepare PSCs with a PCE of 17.05%, which is an improvement of more than 15% compared to the control. However, it is important to note that when the temperature of the slot-die head exceeds 80 °C, solute precipitation at the outlet can obstruct the precursor flow in the ink reservoir. Their findings demonstrate that this strategy significantly enhances the controllability of nucleation. A more appropriate nucleation rate reduction provides sufficient time for the formation of larger grains. Notably, in the absence of hot substrate assistance, merely adjusting the temperature of the hot-head resulted in a significant performance degradation with increasing temperature (Fig. 8h). This is attributed to the negative temperature gradient from the outlet to the substrate, which reduces solvent evaporation and consequently diminishes the crystallization driving force.[108] Despite the superior scalability of slot-die coating due to its continuous liquid supply design, the fine delivery tubes and complex feeding structures of this method increase the difficulty of equipment cleaning and maintenance. Additionally, the significant cost of consumables associated with daily laboratory use is also a noteworthy concern.

3.1.5 Assist process for meniscus coating crystallization. The volatility characteristics of perovskite precursors are contingent upon solvent selection, and the efficient evaporation of solvents plays a crucial role in achieving high-quality crystallization in meniscus coating. On the scale of small cells, the anti-solvent-assisted rapid extraction approach has been extensively investigated.[109] However, in the ideal R2R production scenario, the significant anti-solvent usage introduces additional processing costs. During the early stages of module research, the concept of anti-solvent baths was proposed, but the purification of the anti-solvent under continuous contamination proved to be a challenging issue.[110] Hence, in large-scale PSMs fabrications, to enhance the crystallinity to an exceptional level in more effective and efficient ways, researchers have adopted advanced techniques such as air-knife-assisted, heat-assisted, and vacuum-assisted methodologies.

Among these options, the air-knife-assisted process has emerged as one of the most extensively employed techniques for accelerating solvent evaporation, primarily due to its instantaneous switching capability and exceptional control (Fig. 9a). Typically, inert gases such as nitrogen and argon are commonly employed in this process. The pioneer is the work by Huang *et al.*[111] in 2014 introduced the utilization of gas-assisted crystallization on perovskite films. The fundamental principle underlying this strategy involves the direct removal of surplus solvents through the introduction of enhanced airflow, leveraging gas diffusion mechanisms.[112,113] The net mass flow rate j, governs the evaporation process and can be determined using the following equation:

$$j = \left(\frac{M}{2\pi R}\right)^{\frac{1}{2}}\left(\frac{P}{\sqrt{T}} - \frac{P_g}{\sqrt{T_g}}\right) \quad (12)$$

where M is the molar mass, P and P_g are the saturated vapour pressure and the partial pressure of the evaporated gas phase.

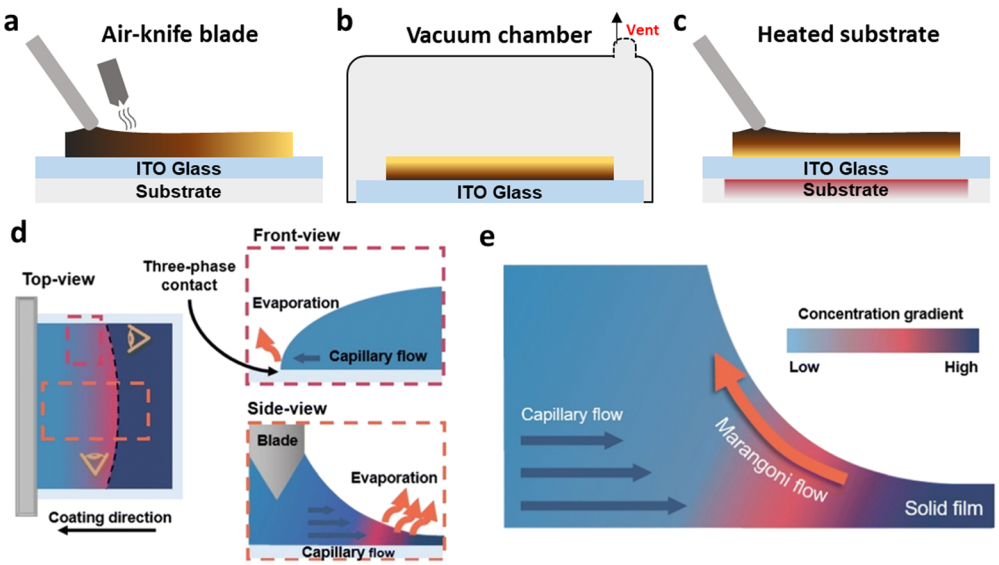

Fig. 9 (a) Schematic illustrations of air-knife assist, (b) vacuum assist and (c) *in situ* heat assist modes. (d) Schematics of main, side and top views of uneven evaporation during blade coating. (e) Schematic diagrams of the flow tracks of the Marangoni and capillary convective flows under meniscus coating process.[114]

T and T_g are the solution and gas temperatures, whose the difference is usually minimal. Consequently, the air-knife brings about rapid airflow, which reduces P_g and consequently leads to an increase in solvent diffusion flux. Besides, changes in the position of the air knife can alter the level of diffusion of solvent molecules, depending on the concentration gradient d given by:

$$d = \frac{\partial C}{\partial h} \approx \frac{\Delta P}{h} \tag{13}$$

where C is the gas concentration, ΔP is the pressure difference between solvent and environment and h represents the distance of air-knife to the wet perovskite film. These relationships demonstrated the closer the distance, the higher the diffusion flux. Gao *et al.*[113] systematically discussed these core parameters of the air knife and summarised and reported a multi-flow air knife (MAK) air-knife assist mode in which a wind circulation system with slots was constructed inside the air-knife to clean up saturated DMF evaporated during the proceeding. They found that narrowing the gap can promote the diffusion of solvent molecules, while the composite airflow can reduce the wavy coffee rings formed by unidirectional wind action and effectively improve the film-forming quality. Eventually, a 300 L min^{-1} flow rate and 1 mm gap were adapted to obtain a compact $MAPbI_3$ film. The current certificated-record for the highest PSMs was also achieved with N_2 knife assistance from blade coating.

Besides, vacuum assistance is also a fast and proficient solvent removal solution (Fig. 9b). By rapidly evacuating the chamber to a negative pressure state, the solvent can be quickly evaporated and dried within seconds. Guo *et al.*[115,116] first introduced this technique in the meniscus process in 2019 and analyzed the reasons for the improvement in the filling factor from the perspective of crystallization kinetics control. In this flow, vacuum pumping rate and duration are two important factors affecting nucleation and crystallization, and their relationship is as follows:

$$P = P_0 \exp(-\alpha t) + P_{\text{limit}} \tag{14}$$

where P, P_0 and P_{limit} present the chamber pressure, the standard vapor pressure and the limit vacuum value respectively. α is the pumping rate constant and t is the pumping time. Xiao *et al.*[117] quantitatively analyzed the relationship between vacuum level and the crystallization and growth of wet perovskite films in blade coating process. They found that a faster pumping rate, at the same duration, greatly facilitated the formation of intermediates, which aided in the nucleation of crystals. Additionally, solvents with high coordination energy, such as *N*-methyl-2-pyrrolidone (NMP), posed a hindrance to pumping, leading to the formation of complex solvation intermediates and inducing the formation of the δ-phase. This method has been proven to have extremely high feasibility, and currently one of the highest-performing PSMs, with a certified PCE of 23.28% on a 22.96 cm^2 aperture area, was achieved by Xu *et al.*[118] harnessing the vacuum-flash process. They employed the Lewis base ligand solvent *N*-ethyl-2-pyrrolidone (NEP), which has a weak coordination ability, as a substitute for NMP and DMSO to regulate the formation of intermediates. Under the condition of a volume ratio of 94 : 6 between DMF and NEP, they achieved champion performance. They discovered that at this volume ratio, there was only a 1-second difference in nucleation rate during the cell-to-module scaling process, providing a surprisingly scalable solution. Ultimately, during the scaling process from 0.08 cm^2 to 22.96 cm^2, there was only approximately a 0.9% efficiency loss. This highlighted the tremendous commercial prospects of vacuum-assisted technology.

Another way of accelerating evaporation is the *in situ* heating (Fig. 9c). Initially, determining the thermal processing window is essential to achieve an equilibrium that prevents the excessive capillary flow from transporting solutes to the interface, forming coffee rings that disrupt homogeneity and morphology. In this context, it becomes necessary to consider a new fluid mechanics factor, the Marangoni effect (Fig. 9d and e).[76,114] As the solvent evaporates during the coating process, the formation of temperature gradients causes the surface tension modification at the contact phase. The hot environment intensifies to a reverse Marangoni flow, offsetting capillary flow, to help mass transport from the edges towards the solution center. Here, the Marangoni number Ma is used to represent a dimensionless quantity that characterizes the relationship between surface tension and viscous forces. The relationship is as follows:

$$\text{Ma} = -\frac{\mathrm{d}\gamma}{\mathrm{d}T}\frac{\Delta T L}{\mu\alpha} \tag{15}$$

where α is thermal diffusivity and L the height of the gap. Siegrist *et al.*[97] investigated the influence of substrate temperature on the deposition of SnO_2 thin films by blade coating. Under a constant speed of 30 mm s^{-1}, they found that a temperature close to the solvent boiling point (70 °C) was the proper window for balancing capillary and Marangoni flows and forming a uniform film. Eventually, they attained high homogeneity of functional layer coating over a 5 cm × 5 cm area and obtained PSMs with up to 18.8% PCE. Furthermore, they discussed and demonstrated that the tempering effect caused by the residence time of the solution had a negligible impact. In addition, heat casting can often shorten or even eliminate the post-annealing process, allowing for high throughput rapid industrial production. Deng *et al.*,[30] whom we mentioned in the previous section, introduced a very low concentration of surfactant LP to modify the drying kinetics of the liquid film in the blade coating. They also introduced in their process that by adding a preheated substrate at 145 °C, they enhanced the process of perovskite film formation.

In summary, the meniscus coating process and crystallization-assisted techniques in terms of processing to aid in understanding and obtaining more perfect crystal films have been developed. Additionally, innovative material engineering approaches that enhance performance through solvent and additive solutions in subsequent discussions were explored.

3.2 Droplets-based fabrication process

Controlled contact-free droplet splatting is a viable solution for large-area manufacturing in the fields of electronics, bioengineering and nanotechnology, *etc.* Disparate from the direct fluid coating, this approach utilizes a nozzle to disperse droplets, forming uniform functional films onto a substrate, thereby enabling customizable and scalable fabrication techniques.

The outcome of this process is determined by the specifications of the nozzle (distance to substrate, speed, flow rate), the ink (viscosity, surface tension), and the substrate (temperature, wetting properties). From the perspective of theoretical physics models of the process, it is summarized as droplet impact dynamics (DID), within which, the factors mentioned above are quantified using three evaluation criteria for printing adaptability: Weber (We), Reynolds (Re), Ohnesorge (Oh) and Z. We and Re determine the relative importance of inertial forces compared to viscous effects and the ratio of inertial forces to capillary forces, respectively. Oh and Z refer to the dimensionless quantifications of the balance between viscous forces, inertial forces, and capillary forces, and are used to determine whether the ink can be sprayed stably. These can be expressed using the following equations:

$$\mathrm{We} = \frac{\rho U D^2}{\gamma} \tag{16}$$

$$\mathrm{Re} = \frac{\rho U D}{\mu} \tag{17}$$

$$\mathrm{Oh} = \frac{1}{Z} = \mu \Big/ \sqrt{\rho U \gamma} = \frac{\sqrt{\mathrm{We}}}{\mathrm{Re}} \tag{18}$$

where U represents the impact velocity of the droplet, D represents the characteristic length of the droplet. Researcher found that the stable printable zone of DID is restricted through these four 'gates' with $1 < Z < 10$, $\mathrm{We} > 4$ and $\mathrm{We}^{1/2}\mathrm{Re}^{1/4} \leq 50$ as illustrated in Fig. 10a.[119]

Spray coating and inkjet printing are the most promising processing techniques in the field of PSMs that apply this underlying physical model. In this chapter, these two techniques will be discussed in detail.

3.2.1 Spray coating. Spray coating is a large-scale manufacturing method for PSMs by dispersing micro-sized droplets onto a substrate with nozzles' favor. It enables high throughput and large-area processing, and area expansion can be achieved by adding nozzle arrays. Presently ETL, HTL, perovskite, and even electrode coverage can be realized by the spray coating process. The desired thin film is formed by the sequential processes of droplet formation, atomization, and droplet merging to form a wet film and subsequent drying, resulting in the

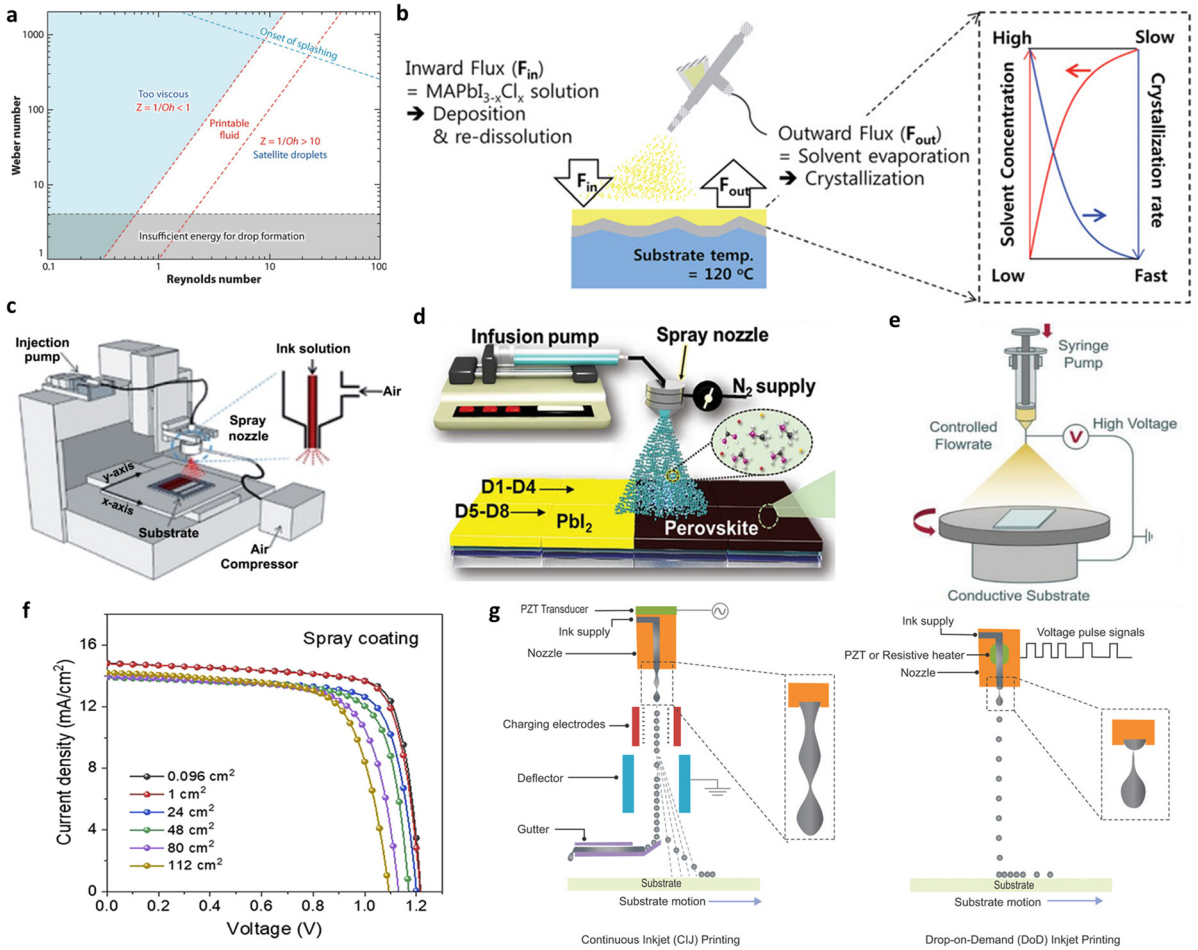

Fig. 10 (a) The processing parameter window for DID.[120] Copyright 2023, Elsevier Ltd. (b) Schematic illustration of the spray coating and crystallization mechanism.[121] (c) Schematic diagrams of pressure-assisted spray,[122] (Copyright 2012, Elsevier B.V.) (d) sonication-assisted spray[123] (Copyright 2023, Wiley-VCH GmbH) and (e) electrospray coating.[124] (Copyright 2023, Wiley-VCH GmbH) (f) changes in the efficiency of PSCs of different sizes prepared by spray coating.[125] (g) Schematics of CIJ and DOD inkjet printing methods.[119] Copyright 2017, Wiley-VCH Verlag GmbH & Co. KGaA, Weinheim.

uniform coverage and crystallization of the perovskite films (Fig. 10b). External aids are required during the process of atomizing the solution into droplets, which leads to three branching approaches: pressure-assisted spray, sonication-assisted spray, and electrospray. Regarding pressure-assisted spray (Fig. 10c), ink is fragmented into small droplets using high-speed airflow, which are then deposited onto the substrate under the influence of the airflow through the nozzle. Kang *et al.*[123] successfully prepared PSMs with 15.8% PCE on a 13 cm^2 area by incorporating propylene carbonate (PC) into the precursor. The addition of PC facilitated the formation of porous and highly oriented porous PbI_2 films, effectively mitigating film defects. Sonication-assisted spray utilizes ultrasonic atomization to refine the precursor ink of perovskite into extremely fine droplets, which are subsequently deposited onto the substrate through a nozzle (Fig. 10d). Im *et al.*[125] fabricated $CsPbI_2Br/CsPbI_{3-x}Br_x$ gradient perovskite structures with sonication-assisted spray. By broadening the absorption range, they achieved a significant enhancement in PCE of nearly 30% to 13.82% on a 112 cm^2 PSM. Furthermore, the PSM demonstrated only a 9% performance degradation after a 1000-hour light soaking test. Electrospray employs electrostatic repulsion to drive the droplets towards the substrate for deposition. Indeed, there have been few reported studies on the electrospray-fabricated modules (Fig. 10e). However, significant progress has been made in terms of the perovskite films optimization. Chen *et al.*[124] proposed an approach to mitigate the composite X-site perovskite recipes' severe photoinduced phase segregation by utilizing the coulomb fission and electric polarization effects in electrospray. They achieved a champion PCE of 20.77% in large-area (1 cm^2) cells based on $Cs_{0.21}FA_{0.74}MA_{0.05}Pb(I_{0.95-x}Br_xCl_{0.05})_3$ perovskite with a wide bandgap of 1.68 eV. The size and uniformity of the droplets are crucial for achieving a perfect-morphology coating and are influenced by factors such as the fluidic properties of the coating solution (viscosity and surface tension determined by precursors concentration), nozzle type, substrate temperature, spray distance and spray velocity *etc.* Deferme *et al.*[126] employed the one factor at a time (OFAT) methodology to systematically investigate the variables involved in the gas quenching process during solution drying. Their study revealed that a crucial factor in enhancing the quality of the thin film was the combination of high gas pressure and a short quenching distance. To sum up, spray coating demonstrates favorable cost-effectiveness and reduced material waste compared to alternative techniques. However, its limited control over solution uniformity leads to non-uniform film thickness, distinguishing it from approaches such as blade coating and slot-die. This non-uniformity can exacerbate interface defects and ion migration, ultimately affecting the performance of PSMs. Unlike the predictable radial force-induced circular uniformity variations in spin coating, the non-uniformity in spray coating is often irregular, which also poses barriers for small lab-scale trials.

3.2.2 Inkjet printing. Drawing inspiration from the remarkable achievements of office printers, inkjet printing has been explored in electronic device manufacturing fields in recent years.[127,128] In PSMs, Yang *et al.*[129] demonstrated the first use of a perovskite precursor $MAPbI_3$ as an ink for PSCs inkjet printing, resulting in 11.60% PCE. Similar to spray coating, it involves the use of a nozzle to release droplets and create patterns. However, what makes inkjet printing unique is its brilliant precision, which enables exceptional flexibility and control in terms of printing thickness, area, and patterns.[127] Continuous inkjet (CIJ) and drop-on-demand (DOD) are the primary techniques employed in inkjet printing (Fig. 10g). CIJ operates by continuously generating droplets and deflecting them toward the desired pattern direction using an applied external electric field. The extra ink is recollected to a gutter. In contrast, DOD straightly prints droplets onto the designated pattern location with higher accuracy and smaller droplet size, which is considered more competitive. Furthermore, DOD can be categorized into thermal and piezoelectric inkjet modes, depending on the type of stress pulse employed. Chalkias *et al.*[130] utilized a piezoelectric-assisted inkjet printing process, achieving 10.07% PCE on a 52.4 cm^2 effective area PSM. They introduced a green, fast-volatile solvent, gamma-valerolactone (GVL), to minimize solvent–solute coordination complexes. This facilitated a fast and efficient crystallization film formation process without requiring annealing.

In addition to the light-absorbing layer, Schackmar *et al.*[131] developed all-functional-layer inkjet-printed PSCs using a full-functional layer. They conducted a step-by-step optimization of inks such as NiO_x, phenyl-C61-butyric acid methyl ester ($PC_{61}BM$), and BCP, as well as the specifications for nozzles and the substrate interface. The resulting PSCs achieved PCE of 17.2% and 12.3% for devices with areas of 0.11 cm^2 and 1 cm^2 respectively. Wei *et al.*[132] investigated the feasibility of utilizing the passivating agent 2-adamantylamine hydrochloride (2-ADAHCl) through inkjet printing. By controlling the deposition surface density at 2.5 μg cm^{-2}, they achieved a remarkable PCE of 24.57% in their PSC devices. Gao *et al.*[133] have achieved large-area $MAPbI_3$ perovskite solar cells based on full inkjet printing. They utilized PEN as the inkjet printing substrate and, following vapor annealing in ethyl acetate, obtained a dense and uniform morphology perovskite film over a sizable area of 120 cm^2 with 16.78% milestone PCE.

The relatively slow processing speed of inkjet printing, compared to other large-area techniques, can be attributed to the smaller size of the nozzle. This may explain the limited number of published results regarding the successful application of inkjet printing in large-area PSMs research. Moreover, achieving synchronized crystallization at different positions during the printing process is a significant challenge, given the critical importance of timing for perovskite precursors. This complex crystallization kinetics problem greatly impacts the uniformity of the resulting films. Along with the high demand of the DID process on the quality of inks, the development of inks is an extremely important topic.

3.3 Contact pattern printing process

3.3.1 Screen printing. Screen printing is a versatile technique that uses a mesh screen to transfer patterns onto a substrate. It is a dominant process in both silicon solar cells and DSSCs. In perovskite photovoltaic system, it has become an

ideal choice for R2R production due to its excellent compatibility with perovskite precursors, substrates glass, PET, PEN, TiO_2, NiO_x, SnO_2, and carbon electrodes.[134–136] Initially, the precursor ink is poured into the printing mesh. Subsequently, under the compulsion snap-off of the doctor blade, the ink permeates the screen and is transferred onto the substrate. Ultimately, as the droplet disengages from the screen, a liquid bridge is formed and propelled by surface tension, it undergoes flattening to yield a thin film as shown in Fig. 11a. The whole process is a convoluted dynamic process which can be attributed to the Hagen–Poiseuille fluid model[137,138] which presents the relationship between the volume flow rate Q and ink viscosity μ as in the following equation:

$$Q = \left[\frac{\pi D^4}{128\mu}\right]\frac{\Delta p}{L} \tag{19}$$

where Δp is the printing process pressure drop, D and L are the diameter and length of the mesh channel. Ku *et al.*[139] first reported the utilization of screen printing technology in PSCs, achieving a PCE of 6.6%. Chen *et al.*[138] developed a solvent engineering approach utilizing high-viscosity methylammonium acetate (MAAc) to modulate the perovskite precursor ink, achieving an astonishingly high ink utilization rate close to 100%. Additionally, they summarized the process trends from 0.25 cm^2 to 25 cm^2 substrates for achieving cell-to-module fabrication at various sizes and achieved the champion PCE of 11.80% and 20.52% on a 16.37 cm^2 minimodule and PSCs respectively through precursors ink screen printing. On this basis the boundaries of solvent engineering have been renewed and expanded, in 2023, their another work[140] illustrated the introduction of the strong ligand solvent methylamine propionate (MAPa) at 25% v/v to MAAc, forming a Pb^{2+} anchorable co-solvent system. Along with this approach, they break the all-screen printing record, pulling the PCE of PSCs up to almost 17%. The mechanism of ink separation between the mesh and the substrate during the screen printing process is crucial for producing defect-free, smooth, and high-performance continuous printed films. Potts *et al.* employed an image-assisted screen-printing visualization (SPV) technique and demonstrated the lowest printing defects when adjusting the viscosity of the TiO_2 ETL ink to a 1 : 0.75 paste to dilutant ratio. Their study achieved an efficiency close to 9.9% on PSMs with an area of 224 cm^2.

Overall, the excellent compatibility of screen printing enables the realization of large-area printing for the full functional layer of PSMs. Currently, it exhibits outstanding performance in processing high-viscosity inks within mesoporous carbon electrode device structures. Notably, in scalable production, how to clean the mesh poses a complex and costly issue compared to other processes.

3.3.2 Flexographic printing. Flexographic printing (relief printing) is a mature R2R manufacturing method in the printing industry. It involves the stable transfer of ink onto a ceramic anilox roller from a flexographic plate roller. The surface of the ceramic anilox roller contains tiny cavities that collect the ink and further transfer it to the raised areas on the printing plate cylinder. Finally, the ink is transferred onto the substrate as illustrated in Fig. 11b.

Flexographic printing technology is widely used to produce transparent electrodes and interface layers in polymer and organic solar cells.[143–145] It is considered to have great potential in customized flexible PSMs. However, currently, there is limited research and most of it focuses on non-absorb ink development, such as Poly(3,4-ethylenedioxythiophene) polystyrene sulfonate

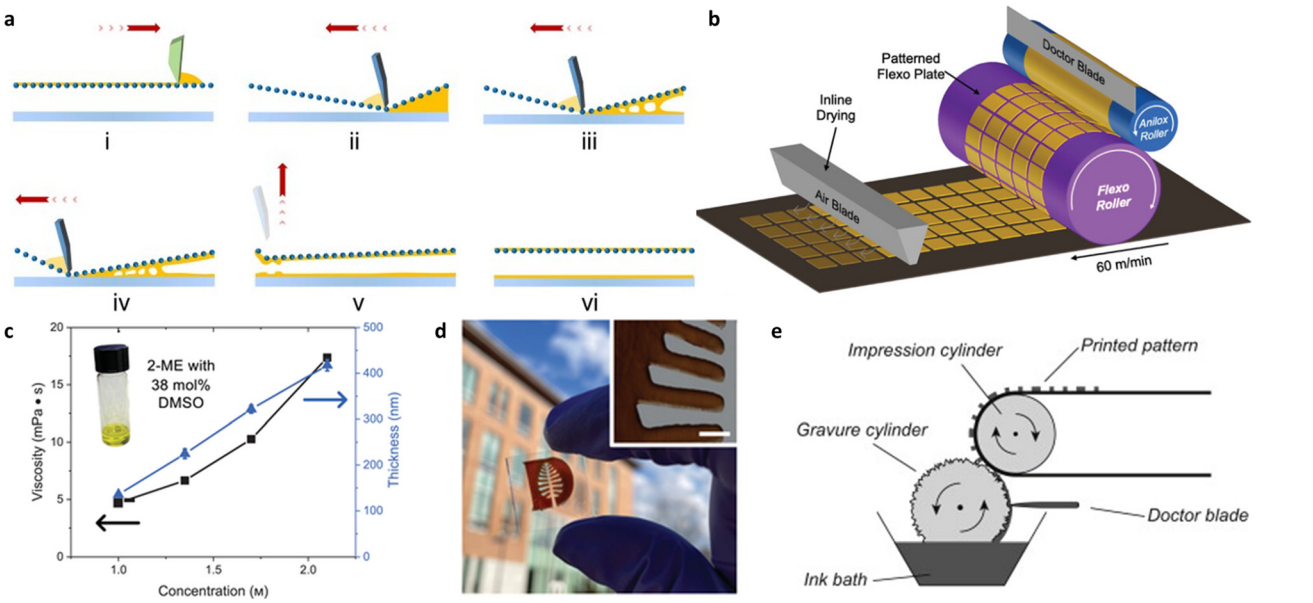

Fig. 11 (a) Schematic diagram of screen printing: transfer of ink from the screen to the substrate.[138] Copyright 2022, Springer Nature. (b) Schematic diagram of flexographic printing process. (c) Viscosity of perovskite ink (black line) and thickness of deposited perovskite film (blue line) as a function of lead concentration in the perovskite precursor. (d) Precise graphic printing by flexographic.[141] Copyright 2023, Wiley-VCH GmbH. (e) Schematic diagram of gravure printing process.[142] Copyright 2015, Elsevier Ltd.

(PEDOT:PSS),[146] NiO_x,[147] *etc.* Thus far, the team of Scheideler and Huddy is the only one that has published their exploration of the flexographic process for perovskite ink (Fig. 11c and d).[141] They successfully prepared $MA_{0.6}FA_{0.4}PbI_3$ films with controlled thicknesses ranging from 100–500 nm under N_2-assisted conditions. Also, their precise edge control resolved the challenge of uneven edges in the P2 scribing process. Ultimately, they achieved large-scale manufacturing on a 140 cm^2 substrate and realized a champion PCE of 20.4% on a 0.134 cm^2 PSC. Unfortunately, they did not continue the exploration of PSMs, but they have already paved a significant milestone in this area.

3.3.3 Gravure printing. Gravure printing is a sophisticated printing method that involves creating recessed patterns, filling them with ink, and transferring the inked pattern in a cyclical printing process onto a substrate as shown in Fig. 11e. However, gravure printing is not ideal for printing on mechanically sensitive rigid substrates, which limits its applications. The shape and thickness of the printed pattern depend on the depth of the recessed pattern and the working speed of the gravure cylinder. The printing speed of gravure printing machines can exceed 18 m min^{-1}, but the optimal process parameters vary depending on the ink being used.[148] The initial development of gravure printing in the electronic device field was practiced on organic photovoltaics (OPVs), Light-emitting diodes (LEDs), photodetectors, *etc.*[149–153] As for the PSMs segment, it is still at the beginning stage. In 2019, the initially published gravure printing in flexible perovskite photovoltaic devices was raised by Kim and colleagues.[154] They figured out the printing conditions for fully functional layers and obtained a PCE of 17.2% on small-area flexible PSCs (F-PSCs), and they confirmed the feasibility of the R2R process. Later on, this research team utilized a *tert*-butyl alcohol (tBuOH) and ethyl acetate (EA) co-solvent bathing approach to improve the crystal morphology of $(FAPbI_3)_{0.95}(MAPbBr_3)_{0.05}$. This led to a remarkable achievement of a new PCE record of 19.1% for gravure-printed F-PSCs.[110] Regrettably, they did not continue with the manufacturing of modules based on this technique. Furthermore, it seems that there have been no significant further advancements in the research related to this particular approach, with Kim and his colleagues being the primary contributors to the progress made thus far.

3.4 Solvent-free fabrication techniques

The solvent-free processing technique is an environmentally friendly method for manufacturing PSMs. In comparison to the traditional solvent-based process, it completely has no or minimal use of organic solvents. This method reduces the negative environmental impact by minimizing the emission of volatile organic compounds, thereby mitigating potential risks to air quality and human health. In general, solvent-free vapor deposition is an environmentally friendly large-area coating strategy that offers excellent reproducibility. It also allows for flexible control of patterns through the use of masks. Additionally, it enables the production of high-quality crystalline films with uniform and controllable thickness. Unfortunately, the energy consumption and equipment costs associated with high-vacuum and high-temperature environments are unavoidable drawbacks. However, despite these limitations, vapor deposition remains a highly promising and competitive large-area coating strategy with significant potential.

3.4.1 Chemical vapor deposition. CVD technology plays a crucial role in PSMs for the preparation of high-quality functional thin films, such as ETL and perovskite, to enhance the performance and stability of solar cells. At high temperatures, the reactant gases undergo chemical reactions to produce reactive species, which adsorb and react on the substrate surface, forming uniform and dense film structures. Due to the relatively low vacuum requirements of CVD, it is possible to simultaneously reduce costs and shield against external stimuli during the fabrication process.[155] In 2014, Leyden *et al.*[156] were the first to utilize hybrid-CVD to produce PSCs with a PCE of 11.8% that remained stable in a nitrogen environment for 1100 hours by evaporating MAI powder in dual-temperature furnace (Fig. 12a). In the CVD process, precise control of parameters such as the composition, temperature, and pressure of the reactant gases enables accurate manipulation of the thin film growth process. Shen *et al.*[157] attempted low-pressure hybrid chemical vapor deposition, revealing the influence of working pressure and reaction time on the deposition of perovskite. They achieved a PCE of 6.22% on a 8.4 cm^2 PSMs active area at a working pressure of 1 Torr. Remarkably, by coordinating precursor material quantities through calculations, they increased material utilization to 50% under these conditions. Since then, Qi's group[48] has continued to research in this field, committed to scale-up, and used hybrid-CVD to tightly and evenly incorporate Cs into FA-based perovskite films. With the help of this A-site cation doping strategy (Fig. 12b), PSMs with good stability were prepared. For the first time, a PCE of nearly 10% was achieved on an area of 10×10 cm^2. In this process, they also found that the vacuum process of CVD has a universally harmful effect on the hole-blocking. As a result, the dual-ETL interface was designed and the interfacial carrier flow was successfully improved.

3.4.2 Physical vapor deposition. At the same time, PVD illustrates a promising potential in the production of functional layers with high quality and various functionalities in the PSMs industry. The resulting thin films exhibit excellent chemical stability and mechanical properties, making them desirable for PSM applications. In the PVD process, the reaction chamber is first evacuated to a high vacuum state, and then the solid-state material is transformed into a vapor phase using a heat source. Subsequently, the vapor-phase material deposits onto the substrate surface, forming a layer of dense and uniform thin film. Among the various methods used in PVD, evaporation and sputtering are the most commonly employed techniques for producing dense thin films. Yi *et al.*[159] discovered that an increased abundance of chlorine in the precursor leads to improved surface smoothness and more uniform and rational crystallization in perovskite films through PVD (Fig. 12d). They achieved an efficiency of 19.87% on a 14.4 cm^2 minimodule. In addition to precursor engineering, the implementation of a multi-source co-evaporation strategy has emerged as a viable

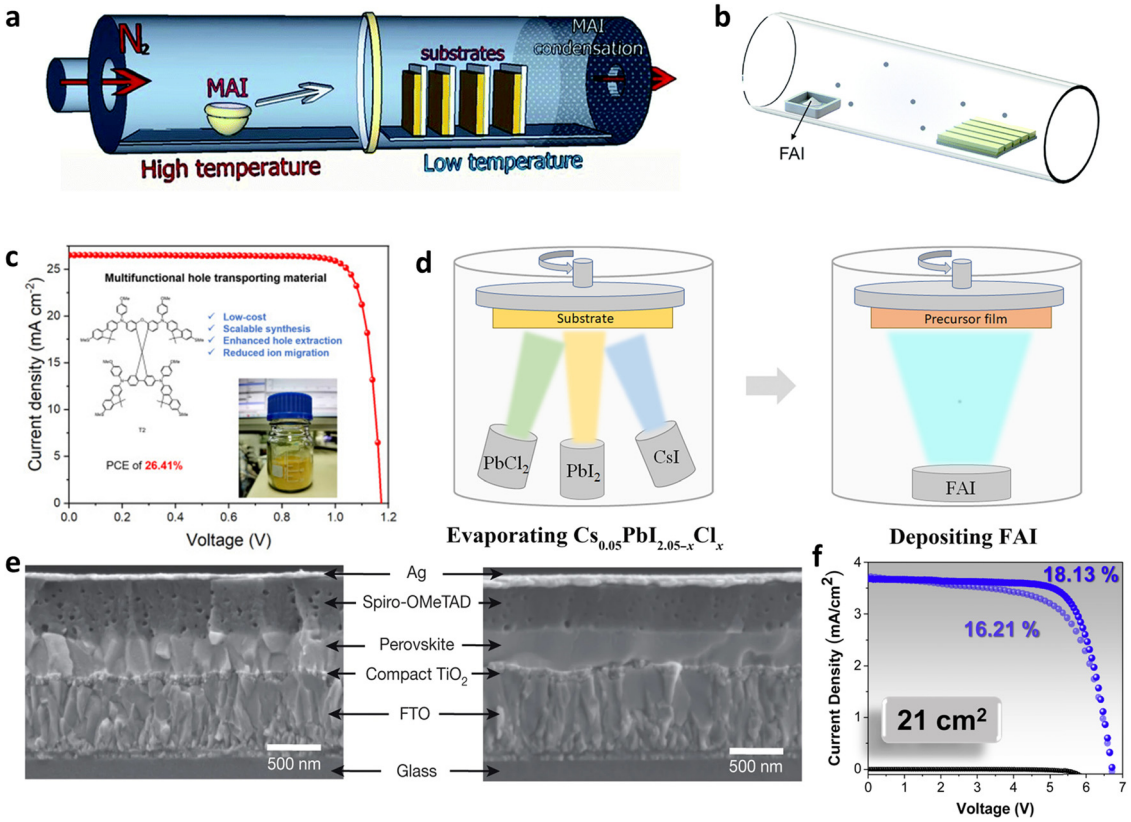

Fig. 12 (a) Schematic diagram of the HCVD furnace and MAI deposition onto metal halide seeded substrates.[156] (b) Hybrids-CVD of the FAI organic precursor for the formation of perovskite.[48] (c) New HTL materials 'T2' assisted the PSCs to achieved a records PCE though co-evaporation.[158] Copyright 2024, Elsevier Inc. (d) Simplified scheme presenting the Cl-containing alloy-mediated sequential vacuum deposition approach.[159] (e) The cross-sectional SEM images of PSCs constructed from a vapor-deposited perovskite film (left) and a solution-processed perovskite film (right).[160] Copyright 2013, Springer Nature Limited. (f) PCE has been enhanced to 18.13% on a 21 cm^2 platform with co-evaporation.[161] Copyright 2020, Elsevier Inc.

and sophisticated approach. The pioneering work by the Snaith group[160] showcased the successful utilization of the co-evaporation technique, yielding a commendable PCE of 15.4% on a minimodule scale with great crystallization morphology (Fig. 12e). Building upon this achievement, the research conducted by the Bruno team[161] unveiled impressive advancements, achieving a record-breaking efficiency of 18.13% on a larger 21 cm^2 platform (Fig. 12f) through the incorporation of interface modifications using MAI and potassium acetate (KAc). Furthermore, their endeavors extended beyond conventional perovskite materials to explore the fabrication of ST-PSMs, showcasing a noteworthy efficiency of 11.2%. These remarkable strides not only contribute to the progress of photovoltaics but also hold significant potential for fostering the advancement of BIPV. There are also techniques that combine the advantages of both methods to prepare high-performance perovskite films. Lu *et al.*[162] proposed a two-step recrystallization strategy, which involves the application of PVD to prepare CsBr/PbI_2 films, followed by the deposition of an FAI/FACl liquid film with a molar ratio of 2 : 1 using CVD. This hybrid vapor deposition approach induced the formation of PbI_2-DMSO intermediate phases at grain boundaries. Through recrystallization, a dense and low-defect $Cs_xFA_{1-x}PbI_{3-y}Br_y$ light-absorbing layer is formed. This approach achieved a champion PCE of 19.9% on PSMs with an area of 10 cm^2. More recently, Zhou *et al.*,[158] as the holders of the efficiency record, fabricated high-quality $FAPbI_3$ thin films by combining a dual-source two-step co-evaporation method (Fig. 12c), achieving a record-breaking certified efficiency of 26.21% on small-area devices and a PCE of 21.45% on a mini-module with an area of 14.4 cm^2.

Through the comparison of the deposition processes of various large-area PSMs, we have summarized the differences between different techniques in Table 2 to aid in understanding the distinctions among them. Spin-coating consistently leads with the highest efficiency records; however, concerning scalability, a majority of high efficiency PSMs are generated through meniscus-based technologies and PVD. Despite their ability to provide high-quality thin films, CVD and PVD processes are constrained in high-throughput manufacturing due to their demanding processing environments and slower deposition rates. Droplets-based and pattern-based methods exhibit relatively lower efficiencies but possess the advantage of patterned manufacturing, suitable for specific application scenarios. Techniques such as flexographic and gravure printing have yet to witness successful PSM attempts, leaving room for further research in the future. Overall, we believe that blade coating and slot-die coating strike a balance between manufacturing efficiency and device performance, serving as robust tools for the industrialization of large-scale PSMs. Future process selections should weigh efficiency, material utilization,

Table 2 The comparison of parameters in mainstream large-scale PSMs production processes

Perovskite deposition methods	Process type	Materials consumption	Cycle time	Environment requirement	PCE records of PSCs (%)	PCE records of PSMs (%)
Spin coating	Centrifugal	High	Medium	Glove box	26.7[35]	22.96[163]
Blade coating	Meniscus-based	Low	Fast	Ambient, low humidity	25.31[164]	23.3[20]
Slot-die coating	Meniscus-based	Low	Fast	Ambient, low humidity	24.1[165]	21.9[165]
Spray coating	Droplets-based	Low	Fast	Ambient, low humidity	22.43[166]	18.0[166]
Inkjet printing	Droplets-based	Low	Fast	Ambient, low humidity	18.26[167]	16.78[133]
Screen printing	Pattern-based	Low	Fast	Ambient, low humidity	20.52[138]	18.12[138]
Flexographic printing	Pattern-based	Medium	Fast	Ambient, low humidity	20.4[141]	Undisclosed
Gravure printing	Pattern-based	Medium	Fast	Ambient, low humidity	19.1[110]	Undisclosed
CVD	Evaporation	High	Slow	Controlled gas environment	21.98[168]	16.16[168]
PVD	Evaporation	High	Slow	Vacuum	26.21[158]	21.45[158]

process speed, and environmental adaptability to drive the commercial application of PSMs.

4. Large-scale deposition of other layers

Apart from the perovskite light-absorbing layer, the deposition of other functional layers (such as the HTL, ETL, and back electrode) exerts a significant influence on both device performance and stability. Similar to the perovskite layer, the fabrication of these functional layers can be broadly classified into solution-based and vapor-phase techniques. The selection of an appropriate deposition method depends on factors such as material solubility, dispersibility, and the stringent quality requirements for thin-film uniformity and functionality.

4.1 Solution-based techniques

Due to its cost-effectiveness and procedural simplicity, solution deposition is widely employed for the deposition of soluble or dispersible materials. Solution deposition is suitable for the deposition of soluble or dispersible materials. Spray coating and chemical bath deposition are commonly utilized for depositing metal nanoparticles. Chang *et al.*[169] utilized a spray coating process to deposit $ZnTiO_3$ ETLs on FTO, producing a minimodule with a PCE of 20.27%. Bi and colleagues[62] achieved a PCE of 15.6% by spray-coating NiO_x on a 36 cm^2 area. Chen *et al.*[170] also employed spray coating to deposit a novel HTL $Ni_xMg_{1-x}LiO$, enabling high-speed charge carrier extraction while preventing pinholes on a large scale. Furthermore, the meniscus coating technique is suitable for the deposition of high solubility transport layers. Huang's research group[95,171,172] has successfully employed the blade-coating deposition technology for poly[bis(4-phenyl)(2,4,6-trimethylphenyl)amine] (PTAA), demonstrating impressive stability and PCE in modules using a 2.2 mg mL^{-1} PTAA solution within a 150 μm coating gap. Wang *et al.*[173] deposited the new hole transport material poly-DBPP self-assembled monolayer (SAM) *via* blade coating at a coating speed of 20 mm s^{-1} and a 200 μm coating gap. This approach yielded one of the most outstanding PCE of 25.1% in PSCs and achieved a high PCE of 22% on PSMs.

Research indicates that the cost of metal electrodes accounts for over 40%[174] of the total cost of perovskite PV devices. In the PSC industry striving for low-cost production to replace silicon-based cells, Carbon materials exhibit good stability, inertness to ion migration, and inherent waterproof properties, making them a promising alternative material to address the high-cost issue. Carbon paste, a back electrode material known for its carrier selectivity, is typically deposited using solution methods such as blade coating, screen printing.[175,176] After calibrating the multilayer functional level for level matching, Yang *et al.*[177] achieved high-performance PSMs with a PCE of 15.3% based on $MA_{0.9}Ga_{0.1}PbI_3$ using a blade-coated low-temperature carbon electrode. Xu *et al.*[178] utilized high-temperature screen printing deposition for all functional layers except the perovskite layer and electrodes, achieving an impressive PCE of 12.87% on an active area of 60.08 cm^2. While devices based on carbon electrodes lag behind those using metal electrodes due to moderate hole extraction capabilities, energy mismatches, and limited lateral conductivity, they hold significant potential for the complete R2R manufacturing of perovskite devices. Furthermore, substituting carbon for metal electrodes will reduce the use of rare contact metals, thereby lowering costs. However, solution methods may face challenges in ensuring adequate uniformity and precision for ultra-thin films with thickness requirements as low as a few nanometers.

4.2 Vapor-phase techniques

For insoluble organic compounds and inorganic oxides that require high thickness accuracy, vapor-phase deposition methods are more suitable. Vapor-phase deposition techniques include sputtering, PVD, CVD, atomic layer deposition (ALD). These methods allow materials to be deposited in gaseous form onto substrates in vacuum or specific gas atmospheres, offering advantages such as high precision, uniformity, and controllability. PVD deposition of metal electrodes, ETL C_{60}, buffer layer BCP, *etc.*,[63,172,179–181] has been widely reported and is a mature technology. However, other techniques are still being explored in this field. Xu *et al.*[118] employed radiofrequency sputtering at room temperature in a pure Ar_2 atmosphere to deposit a 10 nm thin nickel oxide layer. Through the collaborative blade-coating of perovskite deposition, they successfully obtained the second highest PCE ranking currently certified PCE 23.28% on a 22.96 cm^2 minimodule. Lan *et al.*[182] achieved notable results by depositing a 15 nm SnO_2 buffer layer using ALD, enhancing charge extraction and reducing interface recombination. They obtained a respectable efficiency of 17.30% on a relatively large

900 cm^2 module. Broadly speaking, the utilization of vapor-phase processes in large-area modules is widespread, however, due to the vacuum environment required, the production speed in large-scale industrial production lines is slower compared to solution-based methods. Moreover, participation in ideal R2R continuous production processes poses significant challenges.

5. State-of-the-art PSMs improvement strategies

To further enhance the performance and explore prospects the of PSMs, researchers incessantly investigate novel strategies for improvement. This chapter primarily focuses on the latest enhancement approaches, including additive engineering, solvent engineering, and interface modification, to optimize the performance of PSMs. By synergistically employing these cutting-edge strategies, the overall performance and stability of PSMs can be significantly enhanced, thus providing robust support for the widespread application and adoption of sustainable energy solutions.

5.1 Solvent engineering

The pioneering work by Snaith *et al.*[183] in 2012 revealed the use of DMF as a solvent for perovskite precursors, and Conings *et al.*[184] then demonstrated that the addition of DMSO can further enhance the solubility of perovskite. Hence, this discovery laid the foundation for the classical DMF/DMSO mixed precursors solvent system. With gamma-butyrolactone (GBL), NMP they are recognized to be the most effective solvent options.[185,186] These high-boiling polar solvents can be effectively eliminated through the centrifugal force exerted during spin-coating techniques. However, in the aforementioned prevalent pathways for large-scale PSMs production, as indicated by our fluid analysis, the drying process of the solvents becomes considerably more arduous, leading to defect-ridden perovskite films. Consequently, there is an urgent demand for solvents possessing high evaporation flux, which can alleviate this issue and enhance the quality of the films.

Notably, 2-methoxyethanol (2-ME) is considered an effective primary solvent due to its low boiling point (124 °C) and high vapor pressure (6 Tor). It has been proven to assist in the crystallization and shaping processes in meniscus coating.[21,187] The feasibility of post-treatment-free 2-ME was first used and demonstrated by Hendriks *et al.*[187] ACN has a great potential to optimize the rapid formation of high quality perovskite films without external forces due to its extremely high evaporation flux. Deng *et al.*[188] employed a solvent mixture strategy by combining the nonvolatile, coordinating solvents (NVCS) DMSO with two volatile, noncoordinating solvents (VNCS) ACN and 2-ME in a 3 : 2 volume ratio. As the proportion of ACN increased, the processing speed was found to grow within the window of 40–99 mm s^{-1}. At the same time, the grains become larger with the help of DMSO (Fig. 13b). Based on this solvent strategy, they achieved an NREL-certified efficiency of 16.4% on an aperture area of 63.7 cm^2 and kept a high stability for over 1000 hours of maximum power point (MPP) testing (Fig. 13c). In the absence of Lewis base solvent additives, the rapid crystallization of the 2-ME/ACN combination leads to severe crystal defects. However, through experimentation, it has been found that the addition of 20% DMSO effectively regulates and delays the crystallization process, thereby assisting in improving the grain size and crystallinity. Similarly, other Lewis base solvents have shown similar effects.[189,190] Chung *et al.*[191] discovered that incorporating the Lewis base solvent 1,3-dimethyl-imidazolidinone (DMI) into 2-ME enhances the nucleation rate of the stable FAI–PbI_2 coordination complex intermediate phase. This successful inhibition of δ-phase perovskite formation contrasts with the traditional addition of DMSO. By carefully adjusting the proportions, they found that the optimal crystal formation was achieved with a volume ratio of 925 : 75 for 2-ME and DMI, respectively (Fig. 13d and e). Overall, they achieved an impressive PCE of 20.8% on a larger substrate exceeding 100 cm^2, with an effective area of 81 cm^2, using gas-quenched blade coating. Abate *et al.*[192] developed a DMSO/2-ME/ACN binary and ternary solvent system suitable for slot-die coating in wide-bandgap inorganic $CsPbI_{2.77}Br_{0.23}$ perovskite with Lewis base as the primary solvent. By utilizing dynamic light scattering, they discovered that the optimal dispersion of colloidal particles and the resulting improved crystalline surface, leading to enhanced charge transport and an impressive PCE of 19.05%, can be achieved at a DMSO to ACN ratio of 0.8 : 0.2. However, the ternary solvent system exhibited severe surface pinholes. Electrochemical impedance spectroscopy (EIS) revealed a tenfold reduction in composite resistance, from over 2000 to 177.40 Ω. Furthermore, in their attempts on large-area substrates of 100 cm^2, they achieved a PCE of 8.07%. ACN also serves as a primary solvent. Yuan *et al.*[193] have developed a precursor ink strategy with high-evaporative ACN as the primary component and DMSO/DMF as auxiliary additives. This innovative approach effectively suppresses the formation of the coffee ring phenomenon. The low-coordination solvent environment provided by ACN reduces the phase transition barrier of δ-$FAPbI_3$ from −4.2 eV to −4.6 eV. Additionally, it mitigates the defect collapse caused by non-evaporative DMSO at the buried interface, thereby significantly enhancing stability. Remarkably, this strategy enables an exceptionally wide blade coating processing window ranging from 5 to 180 mm s^{-1}, realizing a 15.64 cm^2 minimodule with an outstanding PCE of 21.9%.

5.2 Additive engineering

Additive engineering is a widely used and practical approach for enhancing the performance of PSMs. Some organic molecules can induce better perovskite crystallization. Jiang *et al.*[194] conducted a study on a series of carbonyl additives with large π-electron conjugated structures, and observed a positive correlation between dipole moment polarization and the defect-constraining ability of perovskite as shown in Fig. 14a. Among them, 4-(*N*,*N*-diphenylamino) benzaldehyde (DLBA) stood out with a high dipolarity of 5.88 D. Additionally, DLBA was found to be capable of modifying the surface hydrophobicity of perovskite, thereby reducing the interfacial potential barrier caused by polarity differences. This successful adjustment resulted in lower charge recombination, as evidenced by EIS

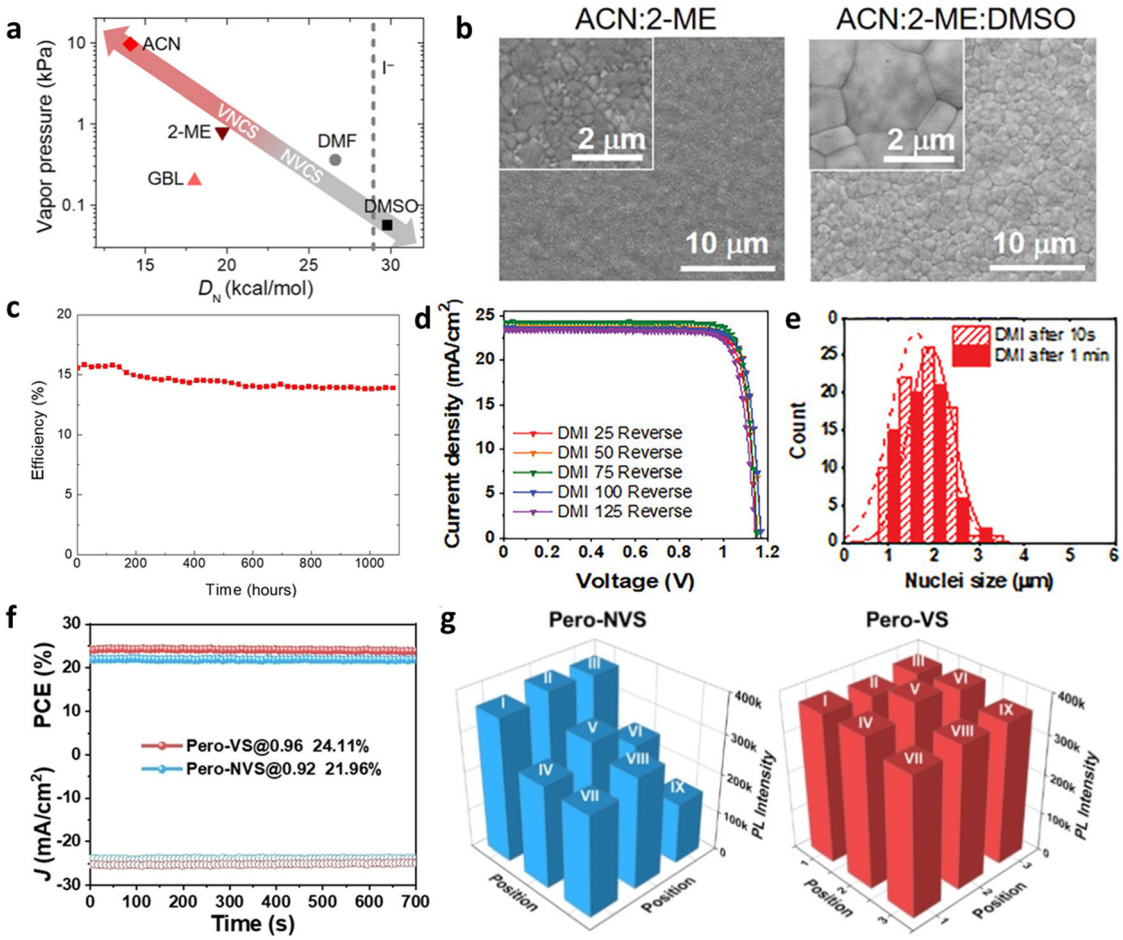

Fig. 13 (a) Vapor pressure and donor number (D_N) of VNCS ACN, 2-ME, GBL and NVCS DMF, DMSO. (b) SEM images of perovskite films fabricated with ACN/2-ME w/ and w/o DMSO. (c) Long-term operational stability of an encapsulated perovskite module loaded at MPP under 1-sun equivalent illumination.[188] (d) *J*–*V* curves with different DMI dosage. (e) Nucleation distribution of 2-Me/DMI complexes.[191] (f) Axial steady-state photocurrent output of $FAPbI_3$ perovskite films (g) the corresponding intensities of 9 platforms in the large-area $FAPbI_3$ perovskite films.[193] Copyright 2023, Wiley-VCH GmbH.

showing a significant decrease in charge transfer resistance. Ultimately, the researchers fabricated PSMs with an area of 14 cm^2 and achieved a PCE of 20.18%, highlighting the potential of carbonyl small molecules. The long-standing challenges of large-scale fabrication and stability in PSMs can be mitigated by incorporating the organic molecule tris(pentafluorophenyl)borane (TPFB) into the HTL. Gu *et al.*[180] discovered that the addition of the water-resistant material TPFB greatly protected the devices from water intrusion as illustrated in Fig. 14b. In a groundbreaking study involving a double-sided perovskite configuration, they achieved exceptional stability with T_{97} exceeding 6000 hours.

Additionally, it is worth mentioning that the addition of the salt has been demonstrated as an excellent modulation strategy. Uddin *et al.*[197] incorporated a zinc metal salt, zinc trifluoromethane sulfonate ($Zn(OOSCF_3)_2$), which effectively suppressed iodine vacancies by utilizing the iodine reduction capability of CF_3SOO^-. During the crystallization process, the presence of Zn^{2+} ions accelerated the nucleation rate. Furthermore, a series of experiments involving the replacement of the anion verified the synergistic passivating effect of this couple of ions. This strategy successfully achieved large-area modules exceeding 100 cm^2 with a certified efficiency of 19.21%. Chen *et al.*[172] explored a cost-effective and efficient reducing additive, benzylhydrazine hydrochloride (BHC), which suppressed the molecularization tendency of iodine in the aging solution (Fig. 14c). In addition, Shi *et al.*[195] introduced the small molecule salt pentanamidine hydrochloride (PAd) and utilized the strong interaction between amidinium and PbI_2 to induce unidirectional crystal growth along (100), skipped the inferior intermediate δ-phase (Fig. 14d). As a result, a 21.4% certificated minimodule was fabricated to prove the scaling up ability. This characteristic extended the shelf life of the precursor solution and significantly reduced the time and material costs associated with large-scale production. Their efforts resulted in a blade-coated module achieving a certified efficiency of 18.2%. Methylammonium chloride (MACl) is widely used as an powerful organic halide salt additive in FA-based perovskite systems, but previous investigations have mainly focused on small-scale explorations.[198–200] Bu *et al.*[196] conducted a study on the application of MACl in large-scale films. They discovered that MACl can significantly reduce the formation energy in the FA-Cs co-A-site

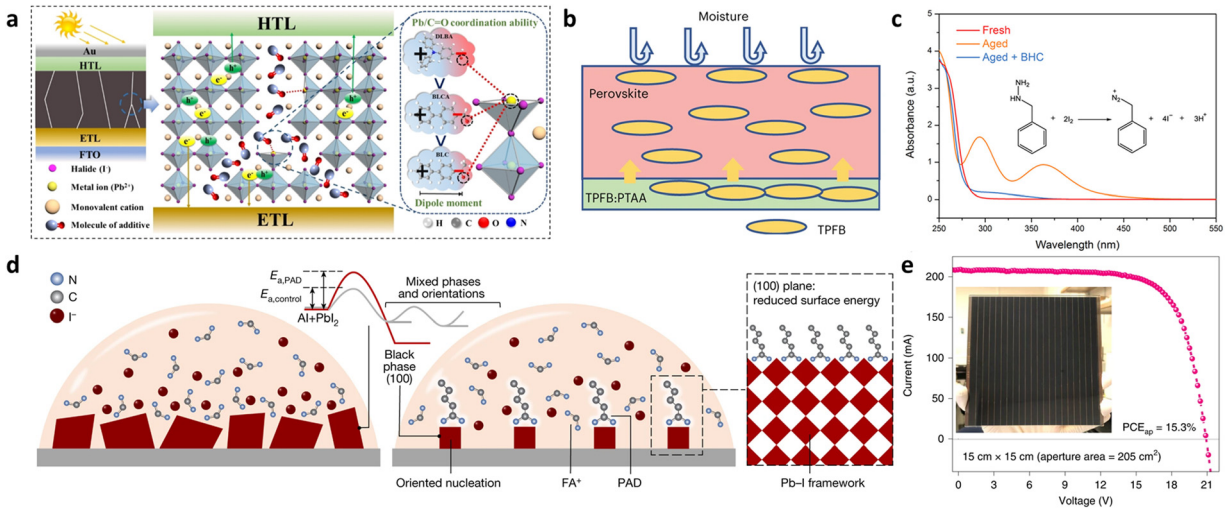

Fig. 14 (a) Action mechanism diagram of additive dipole effect on perovskite film.[194] Copyright 2023, Wiley-VCH GmbH. (b) Schematic diagram of how TPFB prevented the damage of water to perovskite. Yellow arrows indicate the spread of TPFB from the HTL to perovskite film.[180] Copyright 2023, Springer Nature. (c) Ultraviolet (UV)–visible absorption spectra of the fresh and aged 1.37 M MAI : FAI (7 : 3) before and after adding BHC.[172] (d) Schematic illustration of the thermodynamic driving force and the kinetics of the oriented nucleation of perovskite films.[195] Copyright 2023, Springer Nature. (e) Cross-section SEM image of the fully blade-coated perovskite solar sub-module.[196] Copyright 2022, Springer Nature.

system, bypassing the intermediate perovskite-DMF phase and directly transforming into a dense α-phase. Through observing the annealing processes, tiny crystals gradually merged, accompanied by the volatilization of MACl, as a ripening process that resulted in the formation of complete crystals without the anti-solvent extraction. The omission of anti-solvent undoubtedly paved the way for large-scale production. Encouragingly, they achieved a blade-coated submodule with an area of 205 cm^2 and a minimodule with an area of 22.4 cm^2, exhibiting PCEs of 15.30% and 20.5% (Fig. 14e), respectively. Further, the addition of ionic liquids can modulate the potential aggregation problems of organic halide additives. Ding *et al.*[20] developed an ionic liquid additive, 1,3-bis(cyanomethyl)imidazolium chloride ([Bcmim]Cl), that synergistically interacts with MACl, and regulates the aggregation of MACl. Through a series of attempts with fixed cation [Bcmim]+ and various anions, it was observed that Cl^- resulted in stronger proton exchange, manifested by the increased acidity trend in the solution and broadened peaks in ^1H NMR spectra. Helium ion microscopy coupled with secondary ion mass spectromet (HIM-SIMS) analysis demonstrated that the incorporation of this ionic liquid dispersed the aggregated MACl, with $[Bcmim]^+$ being dispersed at the grain boundaries, inducing larger crystal formation and reducing defect density. Ultimately, this strategy enabled them to achieve a certified-PCE record of 23.30% for a blade-coated minimodule.

5.3 Interface modification

Interface modification regulates charge transfer and reduces energy losses in PSMs by introducing functional materials at the interfaces. These functional materials can adjust the energy level alignment, enhance light absorption, improve charge separation efficiency, and thus enhance the photovoltaic conversion efficiency and stability.[95,201–203]

Defect trap states are highly detrimental as they significantly impact both the stability and efficiency of perovskite materials in PSMs. Currently, researchers have identified a range of interface passivation agents that can effectively mitigate the trap states on the surface. For instance, inorganic salts are being utilized to reconstruct the perovskite surface, thereby enhancing carrier mobility and reducing recombination. Additionally, organic polymer materials are being employed to crosslink and anchor free ions, minimizing ion migration and improving the interface characteristics. Rana *et al.*[102] introduced a hydrophobic fluorinated anilinium benzylphosphonate (FABP) as a fully organic passivation agent. By utilizing ammonium and phosphonate groups, they employed a double recombination anchoring mechanism that highlighted the inherent thermal stability of the FACs organic–inorganic hybrid perovskite $Cs_{0.15}FA_{0.85}Pb(I_{0.83}Br_{0.17})_3$, while maintaining over 90% of the initial efficiency after 850 hours of sunlight exposure. They demonstrated the feasibility of this large-scale module fabrication process using slot-die coating and achieved an efficiency of 19.28% on an active area of 58.5 cm^2 (Fig. 15a). Fei *et al.*[95] incorporated PTAA with BCP to chelate the free Pb^{2+} ions at the interface of perovskite, effectively eliminating the formation of a several tens of nanometers thick amorphous layer caused by DMSO evaporation (Fig. 15b). This approach addressed the bottom surface defects that commonly occur during the top-down crystallization of $FA_{0.9}Cs_{0.1}PbI_3$ perovskite films using the N_2 air-knife-assisted blade coating process.[204] As a result, the efficiency of the minimodule was improved to 21.8% while the small blade-coated cells' was 24.6%. Here, our research group published a surface modifier called *N*,*N*-diphenylguanidine monohydrobromide (DPGABr), which can reconstruct the surface within a few hundred milliseconds under blade coating, achieving over 24% PCE on blade-coated small-area PSCs in the ambient air.[21]

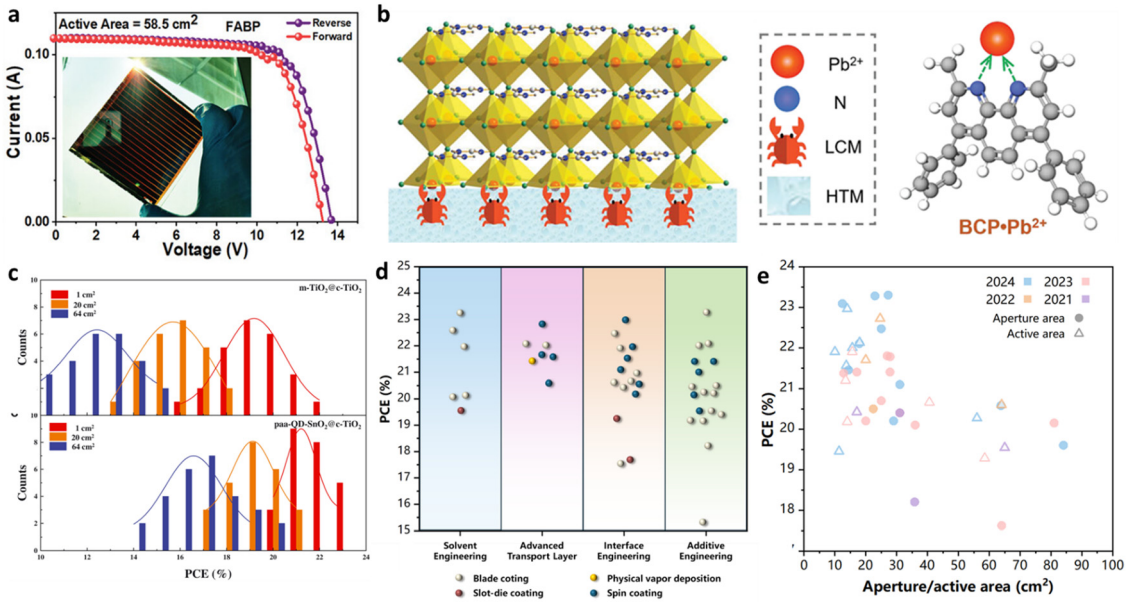

Fig. 15 (a) *J*–*V* curve of the best-performing FABP passivated PSMs.[102] Copyright 2023, Wiley-VCH GmbH. (b) Illustration of the chelation of the lead chelation molecules (LCMs) (in the HTL) with Pb^{2+} ions at the bottom side of the perovskite films.[95] Copyright 2023, American Association for the Advancement of Science. (c) A statistical distribution of the PCE for PSCs with different ETLs.[205] Copyright 2022, American Association for the Advancement of Science. (d) PCE advances in PSMs categorized by improvement strategies and deposition approaches; (e) aperture/active area and year of publication.

In addition, there has been a wave of research focused on the design of novel transport layers. Instead of repairing the interfaces, the strategy of creating new interface systems with materials that exhibit higher charge carrier mobility has gained attention. The development of efficient transport layers can induce a more favorable energy level alignment, thereby reducing losses due to non-radiative recombination. Kim *et al.*[205] designed a new ETL composed of polyacrylic acid (PAA)-stabilized tin(IV) oxide quantum dots (QD-SnO_2) as an alternative to the traditional mesoporous titanium dioxide (m-TiO_2) to reduce optical losses at the interface caused by reflection and interference (Fig. 15c). They achieved a minimodule PCE of 21.7% with a 20 cm^2 active area. The carboxyl groups of PAA are tightly cross-linked with compact-TiO_2 (c-TiO_2), forming an excellent electron-selective contact and optimizing energy level alignment. External quantum efficiency (EQE) measurements confirmed that the J_{sc} of the $FAPbI_3$ system was increased to over 26 mA cm^{-2}. Moreover, the electro-luminescence EQE (EQE_{EL}) decreased from 8.3% to 2.5%, indicating a significant reduction of non-radiative recombination by 80%. Besides, Zhou *et al.*[158] synthesized a novel HTL material T2, which possesses a deeper highest occupied molecular orbital (HOMO). They achieved a PCE of 21.45% on a solvent-free, dual-source CVD platform with an effective area of 14.4 cm^2. The introduction of thiomethyl groups with sulfur atoms in T2 allowed for the anchoring of non-coordinated Pb^{2+} ions at the perovskite interface. Additionally, from a band alignment perspective, T2 exhibited better system-level energy level alignment with both the perovskite and top Au electrode compared to the traditional 2,2′,7,7′-tetrakis(*N*,*N*-di-*p*-methoxyphenylamine)-9,9′-spirobifluorene (spiro-OMeTAD).

Moreover, SAM materials have been considered a promising and effective solution for fixing or replacing HTL by reinforcing anchoring effects. For instance, the three-tooth structure strengthened the anchoring effect of the phosphate groups in SAM directly with TCO to improve the current leakage[206] and the NiO_x-SAM strong linkage modification for the perovskite buried interface.[207] Regarding the application of SAMs in large-scale PSMs, their utilization is still relatively uncommon. Fortunately, Ren *et al.*[202] made preliminary explorations in this area. They polymerized a well-investigated tiny molecule SAMs, (4-(3,6-dimethyl-9*H*-carbazol-9-yl)butyl)phosphonic acid (Me-4PACz), into a long-chain structure. By implementing the N_2 air-knife assisted blade coating process, they achieved a PCE of 20.7% on a module with an aperture area of 25 cm^2 and enhanced the stability to over 1400 hours. Unlike single unit molecules, this denser polymerized structure exhibited reduced sensitivity during anchoring to the TCO, thereby widening the processing window. It resulted in a longer fluorescence lifetime of 633 ns. Additionally, the phosphonic acid groups passivated the buried interface of the perovskite, reducing non-radiative recombination and significantly improving the FF to 83.9%. By optimizing the perovskite thin film and modifying the interface, the photovoltaic efficiency of HTL-free and ETL-free PSCs has significantly surpassed 24%. Zhu *et al.*[208] introduced the SAM into the perovskite precursor solution to deposit and bind it to ITO, ultimately achieving a high-efficiency HTL-free inverted structure device with a record PCE of 24.5% with the assistance of larger Me-4PACz molecules. Additionally, using spin-coating techniques, they achieved a high PCE of 22.5% on a 1 cm^2 area. These findings collectively demonstrate the significant potential and advantages of TL-free structures. These structural optimization

and innovations will further promote the development of PSCs as a renewable energy technology with promising applications.

This chapter presents a thorough examination of the crucial strategies for enhancing the performance of PSMs, which include additive engineering, solvent engineering, and interface modification. Table 3 and Fig. 15d and e have been utilized to respectively encapsulate the recent progressions in PSMs, delineating them based on effective area and chronological categorization, as well as the processing methodologies and strategic approaches employed. By analyzing these methods comprehensively, it becomes evident that their shared principles and mechanisms primarily manifest in three key areas. Initially, optimizing crystal quality and managing defects is vital. The selection of additives and solvents can notably improve the nucleation and growth processes of perovskite crystals. For instance, by controlling solvent evaporation rates or introducing Lewis basic additives, it is possible to enhance grain size and reduce defect density, thereby boosting photovoltaic performance.[20,189–192,197] Furthermore, interface modification strategies enhance carrier dynamics by improving energy level alignment. The utilization of organic polymers or inorganic salts as passivation agents not only enhances interface charge transfer but also improves the long-term stability of devices. Lastly, auxiliary optimization strategies for large-scale processing are essential for industrial production. Achieving uniformity and stability necessitates addressing challenges such as optimizing solvent systems, incorporating interface materials suitable for high-throughput preparation, and developing adjustable film-forming processes. Future research should explore the synergistic effects of these strategies, emphasizing scalability and cost-effectiveness.[158,205] Additionally, it is crucial to adopt environmentally friendly practices to mitigate recycling challenges. For example, the utilization of green solvents like ACN is pivotal for advancing the commercial development of perovskite solar technology.[188,195]

6. Device encapsulation and stability tests

Researchers have made significant breakthroughs in the PCE of PSMs as they gradually acquire the fabrication processes of the functional layers on a larger scale.[20,158,209,224] However, to achieve commercialization and large-scale production, enhancing the stability of PSMs is a topic that deserves deep consideration. The instability issues of PSMs can be divided into two fields, intrinsic and extrinsic. Intrinsic factors include the instability caused by phase transitions and defects in perovskite materials, while extrinsic factors involve rapid aging and degradation induced by environment heat, moisture, and oxygen.[225–228]

The internal instability of perovskite materials is closely intertwined with their structural and chemical stability. The mathematical formulation of the Goldschmidt tolerance factor t[229] can be expressed as follow:

$$t = (r_A + r_X)/\sqrt{2}(r_B + r_X) \quad (20)$$

where r_A, r_B and r_X represent the radius respectively. It has been recognized that perovskite lattice structures can maintain higher stability and symmetry within the range of t values between 0.825 and 1.059.[230] The tolerance factors of disparate perovskite are shown in Fig. 16a. This methodology has been a valuable tool in the analysis of perovskite crystal stability for almost a century. Therefore, the introduction of additives can change the tolerance factor and further affect the stability of perovskite. Park *et al.*[231] incorporated guanidine derivatives as additives, resulting in a 30% enhancement in aging stability. The incorporation of X-site chlorides has facilitated more precise control over the crystallization process, with MACl being extensively utilized as an additive.[20,198–200] In addition, elements such as Cs and Rb are considered to have excellent structural and chemical stabilizing effects.[232] Simultaneously, extrinsic factors significantly impact the stability of solar modules. Moisture ingress can induce hydrolysis and ion dissociation in perovskite materials and the presence of oxygen promotes oxidation reactions in perovskite materials, leading to structural damage and performance degradation. However, with the interest in long-term stability mechanisms, the tolerance coefficient as a determinant of stability is not comprehensive enough.

Additionally, UV radiation is a critical factor that triggers photodegradation, charge defects, and lattice distortions in perovskite materials. Elevated temperatures accelerate lattice expansion and ion migration processes, contributing to decreased material stability. Mechanical stress, such as bending and stretching, can cause cracks and fractures in the perovskite layer, consequently reducing module performance and lifespan. Furthermore, light intensity and spectral composition influence the stability of perovskite materials, with high-intensity light and specific wavelengths leading to material degradation and deterioration.[235] Take $MAPbI_3$ as an example, the pathway of perovskite degradation is illustrated in Fig. 16b.[234] Simultaneously, during the real-life operation of PSMs, it has been found that the stability of PSMs is also affected by factors such as layer delamination and potential-induced degradation (PID). The multi-layer structure of PSMs inherently introduces challenges related to delamination, primarily stemming from the lamination process and differential thermal expansion characteristics across layers. Delamination issues manifest in two key areas: the separation between encapsulation materials and the device, and internal delamination within the device itself. The former is chiefly influenced by the properties of the encapsulation materials, with considerations such as water vapor and air barrier capabilities, as well as mechanical resistance playing pivotal roles. Multi-layer encapsulation[236,237] and advanced lamination processes[238,239] can effectively improve the resistance to delamination. In rare cases, delamination will occur immediately after an immature lamination process.[240] However, the delamination phenomenon between layers inside PSMs is different. Erdil *et al.*[240] tested the relationship between each layer through indoor thermal cycle testing and found that this phenomenon is dominated by temperature fluctuations. The ETL part of C_{60} and SnO_2 is the most likely to fall off in the entire structure. We were surprised to find that this coincides with the delamination phenomenon of SnO_2 often encountered in vacuum annealing

Table 3 Recent state-of-the-art PSMs improve strategies

Perovskite composition	Type	Effective materials	Perovskite process type	Assist mode	PCE (%)	Aperture/ active area[a] (cm^2)	Year	Ref.
$Cs_{0.05}MA_{0.05}FA_{0.9}Pb(I_{1-x}Cl_x)$	Additive engineering	[Bcmim]Cl	Blade coating	N_2 air knife	23.3[C]	27.22[1]	2024	20
$Cs_{0.1}FA_{0.9}PbI_3$	Solvent engineering	NEP	Blade coating	Vacuum	23.28[C] 22.55[C]	22.96[1] 57.13[1]	2024	118
$FAPbI_3$	Solvent engineering	DMF	Blade coating	N_2 air knife	23.09[C]	12.4[1]	2024	164
$((FA_{0.95}Cs_{0.05})PbI_3)_{0.975}$-$(MAPbBr_3)_{0.025}$	Interface treatment	SnO_2 with different oxygen vacancies level	Spin coating	Anti-solvent	22.96	14[2]	2024	163
$Rb_{0.03}Cs_{0.05}MA_{0.05}FA_{0.90}PbI_3$	Advanced ETL Materials	TiO_2 nanoparticles	Spin coating	Vacuum	22.72[C]	24.63[2]	2022	209
$FAPbI_3$	Interface treatment	Trifluoroacetate (TFA^-) and 3,3-diphenylpropylammonium (DPA^+)	Blade coating	N_2 air knife	22.47 (20.50[C]) 20.88	25[1] 64[1]	2024	210
$FA_{0.9}Cs_{0.1}PbI_3$	Additive engineering	Ferrocenium hexafluorophosphate ($FcPF_6$)	Blade coating	Vacuum	22.13 20.27	36[1] ($18^{2)}$) 100[1] ($56^{2)}$)	2024	211
$FA_{0.9}Cs_{0.1}PbI_3$	Advanced HTL Materials	[2-(9-Ethyl-9*H*-carbazol-3-yl)ethyl]phosphonic acid ($EtCz_3EPA$)	Blade coating	Regular annealing	22.1	17.88[1]	2024	179
$MA_{0.7}FA_{0.3}PbI_3$	Advanced HTL Materials	Poly-DBPP	Blade coating	N_2 air knife	22	30.03[1]	2024	173
$FAPbI_3$	Additive engineering	Perfluoroalkylsulfonyl quaternary ammonium iodide (FSAI)	Blade coating	N_2 air knife	22	15.64[2]	2024	212
$FA_{0.92}MA_{0.08}PbI_{2.76}Br_{0.24}$	Interface treatment	2-Chloro-5-(trifluoromethyl)-phenylammonium bromide	Spin coating	Regular annealing	21.9	10[2]	2024	165
$FAPbI_3$	Solvent engineering	ACN	Blade coating	N_2 air knife	21.9	15.64[2]	2023	193
$FA_{0.9}Cs_{0.1}PbI_3$	Interface treatment	BCP	Blade coating	Regular annealing	21.8[C]	26.9[1]	2023	95
$Cs_{0.05}MA_{0.05}FA_{0.9}PbI_3$	Advanced HTL Materials	A novel spiro-type HTM 'DP'	Spin coating	vacuum	21.78[C]	27.86[1]	2023	213
$FAPbI_3$	Advanced HTL Materials	Polyacrylic acid-stabilized tin(IV) oxide quantum dots	Spin coating	Anti-solvent	21.7[C] 20.6[C]	20[2] 64[2]	2022	205
$Cs_{0.05}MA_{0.1}FA_{0.85}PbI_{2.9}Br_{0.1}$	Interface treatment	Phenethylammonium bromide (PEABr) and polymethyl methacrylate (PMMA)	Spin coating	Anti-solvent	21.56	13.68[2]	2024	214
$FAPbI_3$	Advanced HTL Materials	A novel spiro-type HTM 'T2'	PVD	None	21.45	14.4[1]	2024	158
$FAPbI_3$	Additive engineering	PAd	Spin coating	Vacuum	21.4[C]	27.83[1]	2023	195
$Cs_{0.05}FA_{0.85}MA_{0.10}$-$Pb(I_{0.97}Br_{0.03})_3$	Additive engineering	Fullerene derivative 4-(1′,5′-dihydro-1′-methyl-2′*H*-[5,6] fullereno-C_{60}-I_h-[1,9-*c*]pyrrol-2′-yl) phenylphosphonic acid (CPPA)	Spin coating	Vacuum	21.4 (19.6[C])	17.1[1]	2023	215
$Cs_{0.05}(FA_{0.9}MA_{0.1})_{0.95}$-$Pb(I_{0.9}Br_{0.1})_3$	Module protection	O_3	Spin coating	Anti-solvent	21.37[C]	12.84[1]	2023	61
$FAPbI_3$	Interface treatment	Benzamidine hydrochloride (PFACl)	Spin coating	Regular annealing	21.2	13.44[2]	2023	216
$FAPbI_3$	Additive engineering	Thermotropic liquid crystals 3,4,5-trifluoro-4′-(trans-4-propylcyclohexyl)biphenyl (TFPCBP)	Spin coating	Vacuum	21.1[C]	31[1]	2024	217
$MA_{0.7}FA_{0.3}PbI_3$	Interface treatment	Me-4PACz	Blade coating	N_2 air knife	20.7	25[1]	2023	202
$FAPbI_3$	Interface treatment	Carbon disulfide (CS_2) vapour	Blade coating	Undisclosed	20.66	40.6[2]	2023	218
$Cs_{0.05}FA_{0.95}PbI_3$	Interface treatment	Dimethylammonium trifluoroacetate (DMATFA)	Spin coating	Vacuum	20.58	63.74[1]	2024	219
$FA_{0.88}Cs_{0.12}PbI_3$	Additive engineering	MACl	Blade coating	Air knife	20.5 15.3	22.4[1] 205[1]	2022	196
$FA_{0.83}Cs_{0.17}PbI_3$	Solvent engineering	NMP	Slot-die coating	Air knife	20.42 (19.3[C]) 19.54	17.1[2] 65[2]	2021	220
$FA_{0.95}MA_{0.05}PbI_{2.85}Br_{0.15}$	Additive engineering	1-Butyl-3-methylimidazolium thiocyanate (BMIMSCN)	Blade coating	Regular annealing	20.4	10[2]	2022	221
$(FAPbI_3)_{0.95}(MAPbBr_3)_{0.05}$	Interface treatment	Acetylcholine bromide (ACBr)	Blade coating	N_2 air knife	20.4 (17.53[C])	31[1]	2021	222
$MA_{0.7}FA_{0.3}PbI_3$	Additive engineering	TPFB	Blade coating	N_2 air knife	20.2 (19.2[C])	22[1]	2023	180
$Cs_{0.05}MA_{0.05}FA_{0.9}PbI_3$	Interface treatment	Potassium borohydride (KBH_4)	Spin coating	Vacuum	20.2	29[1]	2024	223
$FA_{0.90}MA_{0.03}Cs_{0.07}$-$Pb(I_{0.92}Br_{0.08})_3$	Additive engineering	DLBA	Spin coating	Anti-solvent	20.18	14[2]	2023	194
$(FAPbI_3)_{0.95}(MAPbBr_3)_{0.05}$	Solvent engineering	DMI	Blade coating	Air knife	20.10	36[1]	2023	191

Table 3 (*continued*)

Perovskite composition	Type	Effective materials	Perovskite process type	Assist mode	PCE (%)	Aperture/ active area[a] (cm^2)	Year	Ref.
$MA_{0.7}FA_{0.3}PbI_3$	Additive engineering	$Zn(OOSCF_3)_2$	Blade coating	N_2 air knife	20.15 19.60[C] 19.21[C]	81^1 84^1 108^1	2024	197
$FA_{1-x}MA_xPb(I_{1-y}Br_y)_3$	Additive engineering	2-(*N*-Morpholino)ethane-sulfonic acid potassium salt (MESK)	Blade coating	N_2 air knife	19.45	11.35^2	2024	181
$Cs_{0.15}FA_{0.85}Pb(I_{0.83}Br_{0.17})_3$	Interface treatment	FABP	Slot-die coating	N_2 air knife	19.28 17.62	58.5^2 64^1	2023	102
$MA_{0.7}FA_{0.3}PbI_3$	Additive engineering	BHC	Blade coating	N_2 air knife	18.2	35.8^1	2021	172

[C]The PCE has been certified by a recognised authority. [1]Aperture area. [2]Active area. [a] Since authors use different statistical scales for area, in order to avoid ambiguity, we use superscripts 1 and 2 to represent aperture area and active area (without considering GFF) respectively for ease of understanding.

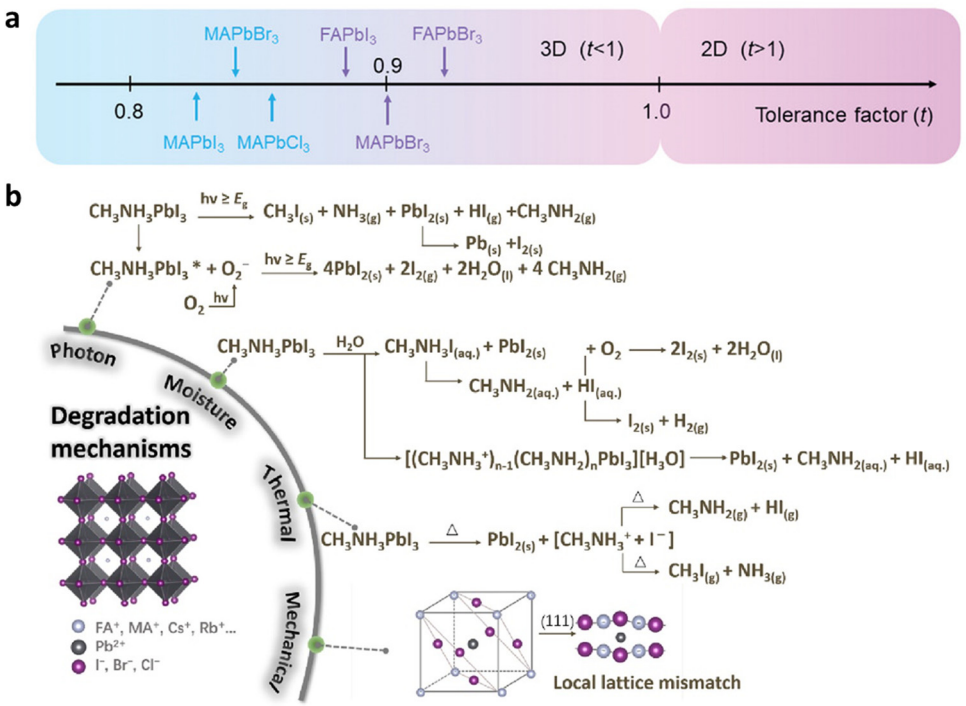

Fig. 16 (a) Tolerance factors distribution of different perovskite compositions.[233] Copyright 2022, Wiley-VCH GmbH (b) The instability stress sources of perovskite materials.[234]

in Qi *et al.*'s[48] exploration of CVD preparation of PSMs in Section 3.4.1. These findings have promoted in-depth research on advanced thermally stable carrier transport materials and thermal insulation packaging materials. Additionally, PID is manifested as a significant decline in the performance of photovoltaic devices under the influence of an external voltage bias or internal electric field, which is caused by the high voltage difference between the module and the ground during operation.[241] In traditional silicon solar modules (SSMs), PID is observed as the migration of alkali metal ions, such as sodium ions (Na^+), in soda lime glass when the device is at a negative potential to the ground, which can cause rapid and catastrophic damage.[242–244] In addition to the impacts similar to those in SSMs, which mainly come from the packaging materials, perovskite has unique ionic properties and the multiple impacts of PID caused by its internal high ion migration activity are more serious and fatal to stability.[245,246] Interestingly, Zhang *et al.*[241] found that after applying −1500 V negative bias for 18 hours, the diode characteristics of the device gradually disappeared and could be quickly recovered to 80% in dark storage. They believed that this recoverability was due to the ion migration performance of perovskite, which enabled the Na^+ driven by the bias to migrate quickly out of the perovskite layer. Researchers are still exploring the mechanisms involved, but some strategies have been found to alleviate PID to a certain extent by selecting proper functional layer and interlayer buffer strategies. Zeel *et al.*[246] found that

using $PC_{61}BM$ as ETL in n–i–p can temporarily reduce PID, with only 4% performance loss under 18 hours of continuous bias. NiO_x barrier layer was found by Nakka and colleagues[247] that successfully kept Na+ away from perovskite and reduced the PCE loss from 73% to 35%. Currently, the IEC 62804-1-1 technical specification defines the test method for crystalline silicon PV modules,[248] but there is no specific PID test standard for PSMs. Research papers generally utilize the horizontal comparison of performance degradation under the condition of applying a negative bias of −1000 V. Given this, we contend that with the deepening industrial deployment, it is imperative to establish more standardized and comprehensive industry testing standards to evaluate the stability factors of both internal and external placements and operations at various stages. This initiative aims to bolster the commercial impetus of PSMs and enhance customer assessment criteria.

Table 4 Specification parameters and criteria for common encapsulation materials

Characteristics	Specification or requirement
WVTR	10^{-4}–10^{-6} g m^{-2} day^{-1}
OTR	10^{-3}–10^{-5} cm^3 m^{-2} day^{-1} atm^{-1}
T_g	<−40 °C (during winter in deserts)
Total hemispherical light transmission over the wavelength range from 400 nm to 1100 nm	>90% of incident light
Hydrolysis	None (80 °C, 100% RH)
Water absorption	<0.5 wt% (20 °C/100% RH)
Resistance to thermal oxidation	Stable (up to 85 °C)
Mechanical creep	None (90 °C)
Tensile modulus	<20.7 MPa (<3000 psi) at 25 °C
Chemical inertness	No reaction (with embedded Cu coupons at 90 °C)
UV absorption degradation	None (>350 nm)
Hazing or clouding	None (80 °C, 100% RH)

6.1 Device encapsulation

Encapsulation, which is considered by an increasing number of scientists to be a consensus in development, serves as a direct and effective bidirectional protective measure. It effectively isolates the extrinsic complex environment that accelerates aging while also preventing the leakage of lead in PSMs from impacting the extrinsic environment.[249] Due to the unique degradation mechanisms and fragile stability of PSMs, the primary task is to ensure isolation from water and oxygen. For PSMs, although we all know that encapsulation technology is a commercially indispensable technological barrier, the exploration of encapsulating technology is still far behind the focus on performance at the current stage. The main parameters affecting the encapsulation of the material are shown in Table 4.[226]

Due to the light absorption window being restricted to the bottom surface, the optimal encapsulating technique for PSMs corresponds to that of SSMs, employing a single-sided glass vacuum lamination process. This process can be categorized into two distinct pathways, the thin-film encapsulation (TFE) from the top to the bottom, and the edge seal (ES) from the side to the center, as depicted in Fig. 17a.[250] Both these two processes offer excellent encapsulating performance. ES is considered a more cost-effective encapsulating solution as it requires less material. However, in the field of flexible encapsulating, TFE surpasses ES since the encapsulation material has a smaller contact area and mechanical side stress in ES, leading to potential seal damage during bending. At present, commercial polymer demonstrate excellent performance in both TFE and ES processes and can be uniformly applied to the device using spin coating or injection methods. Traditional polymers such as PMMA,[251–253] ethyl vinyl acetate (EVA),[254] and polycarbonate (PC),[227] *etc.* have shown promising results in TFE. With the increasing area of functional layer deposition,

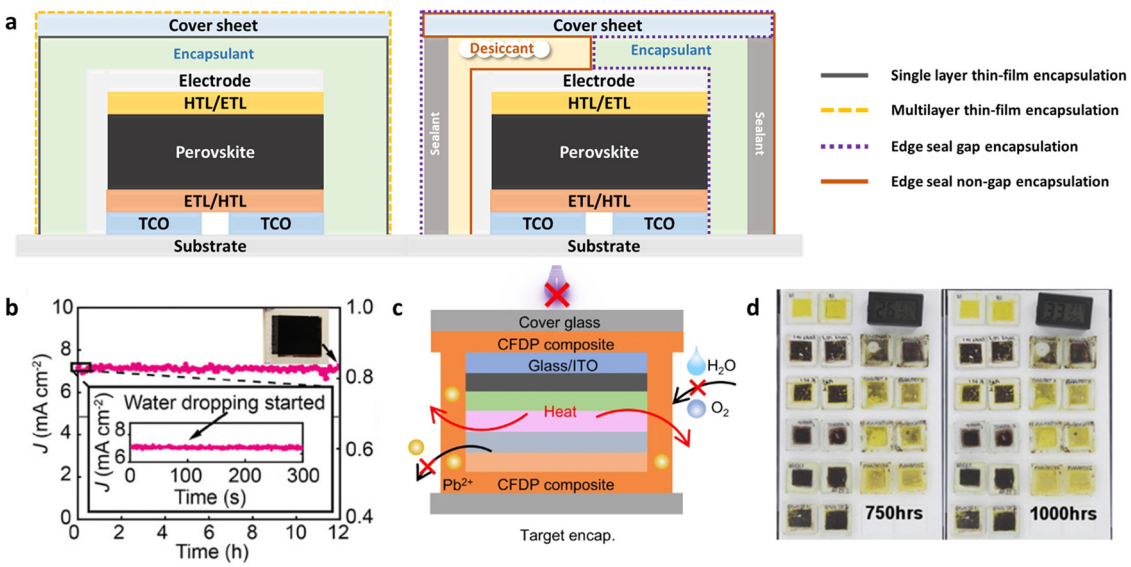

Fig. 17 (a) Schematic diagrams of different TFE and ES encapsulation approaches. (b) High stability performance under water drop stress.[136] (c) Schematic of CFDP package without UV irradiation.[257] (d) The degradation performance after 750 and 1000 hours.[258] Copyright 2016, Elsevier Ltd.

the TFE encapsulation mode also requires materials with corresponding extensibility to serve PSMs and better facilitate commercial applications. PMMA, known for its high impact resistance and thermal stability, is widely utilized in the circuit printing field. Typically prepared *via* spin coating, PMMA usage aligns with the challenges faced in the laboratory-scale expansion of PSCs. Hughes *et al.*[255] addressed this issue by adjusting the solvent environment of PMMA, designing uniformly dispersed encapsulants in ethyl acetate. This innovative approach provided a PSM-friendly solution idea for large-area coating using a spray coating process. Moreover, PC is considered to be a good packaging material due to its excellent flexibility, but its high roughness is seldom used in large area packaging. Skafi *et al.*[256] used a blade coating method to reduce its roughness from over 1400 nm to 23 nm by applying a resin mixture and enhanced its chemical resistance, which provides an imaginative way for PC to be used in large area PSMs.

Furthermore, more recent research on advanced encapsulation materials has also seen new developments, which especially affect several narrow protective capabilities. In addition to glass encapsulation, Mai *et al.*[136] explored novel encapsulation techniques by introducing Glaco, a commercialized thin nanostructured super-repellent coating material. They successfully induced an advancing contact angle greater than 167° and a contact angle hysteresis less than 10°. This method significantly enhanced the waterproofing performance of the devices from nearly zero to over 12 hours of water tolerance (Fig. 17b). This provides a promising avenue for enhancing the stability against water-induced degradation. Based on existing materials and processes, the isolation of water and oxygen has generally met the requirements. However, there has been limited attention given to external thermal management and the environmental pollution caused by lead leakage. Thermal energy produced can lead to rapid ion migration, resulting in the severe degradation of perovskite materials. While Pb, as a highly toxic element, poses a significant threat to human and environmental safety if it leaks. Tong and colleagues[257] developed a self-crosslinked fluoropropyl methylsiloxane-dimethylsiloxane multiblock polymer (CFDP) encapsulation material that can be processed at room temperature, eliminating the thermal instability caused by high-temperature lamination (Fig. 17c). The material maintained 95% efficiency after undergoing 220 thermal cycles. Moreover, the incorporation of carbonyl groups facilitated coordination and anchored Pb, leading to 99% leaking inhibition during a rainwater exposure test. Moreover, Qi *et al.*[259] discovered that materials with high self-healing properties at temperatures above T_g can significantly reduce the risk of Pb leakage. They made remarkable achievements by adopting ternary additive engineering to a thermocrosslinking epoxy resin, changing T_g to 42 °C. This modification led to a staggering reduction of 375 times in lead leakage under extreme and harsh hail simulation conditions. Additionally, Mariani *et al.*[260] discovered a new packaging material, viscoelastic (semi-solid)/highly viscous (liquid) polyolefin, which can be operated in industrial high-throughput solventless lamination. The addition of two-dimensional hexagonal boron nitride (h-BN) in the solution further enhances its adhesive, barrier, and thermal management properties. High stability was demonstrated through multiple cycles of aging tests involving light, heat, and impact.

6.2 Standardized stability tests

The encapsulated perovskite module needs to undergo a series of stability tests to evaluate its performance under different environmental conditions. However, most research papers on stability mainly focus on inconsistent simple tests like environmental storage or light soaking at present, which do not meet the stringent stability requirements for commercial products under specific conditions, limiting the full potential of the technology. Therefore, the development of guiding standards for stability testing of PSMs is pressing and imperative.

Regarding traditional ground-mounted photovoltaics, which mainly refers to silicon solar arrays, the International Electrotechnical Commission (IEC) has provided a set of on-site performance testing standards known as IEC 61215.[248,261] However, due to the differences in physical systems, these standards are not applicable to the new generation thin-film cells such as OPV and PSMs. In the battle to establish standards, many scholars have proposed solutions, but the problem is the inability to form unified standardized criteria. This undoubtedly hinders the transition of experimental products to the industrial production process.[262–264] Therefore, in 2011, Reese *et al.*[265] integrated and organized the major research advancements in the field and introduced the International Summit on Organic PV Stability (ISOS) protocols as a standardized aging experiment guideline. This document is not a definitive verdict but rather a standardized guidance to assist in conducting experiments in disparate research environments. It serves as a starting point and will be gradually improved as research progresses.[266]

The ISOS testing protocol is primarily defined by the combination of four stressors, namely, light exposure (one standard solar simulator or complete darkness), ambient contaminants (inert gases, atmospheric air, or controlled relative humidity), temperature (ambient temperature, 65 °C, or 85 °C), and electrical bias (open circuit (OC), maximum power point tracking, or +/− fixed voltage).[265] Based on the different combinations of these environmental stressors, the testing protocol is divided into five stress testing tracks. ISOS-D and ISOS-L represent a complementary set of light environment stress controls. ISOS-D involves testing the device's resilience to atmospheric contents and monitoring the degradation and the formation of defects in a darkened setting. Conversely, ISOS-L entails prolonged continuous light soaking, which expedites defect formation and phase separation processes. In addition to these steady-state tests under fixed conditions, ISOS-T and ISOS-LT explore cyclic conditions. Their objective is to investigate the lifespan under the cyclic interplay of heat and light-moisture-heat, which more faithfully simulate the dynamic environmental variations of light and temperature in real-world climates. The repetitive migration of charge carriers during this process is regarded as a significant acceleration factor for aging. Recognizing that indoor testing alone cannot adequately reflect real-world scenarios like building-integrated photovoltaics, such as BIPV, ISOS-O is specifically devised for outdoor testing. It primarily focuses on

statistically assessing the lifetime performance under actual outdoor conditions. Given the diverse climatic conditions across different regions, this testing approach places greater emphasis on comprehensive data collection to provide a wide range of acceleration factor information.

The new edition of ISOS offers three targeted testing protocols for PSCs to address their dual degradation mechanisms of intrinsic and extrinsic stability. The light soaking and dark mode alternating cycle testing, ISOS-LC, has been included as a supplement to assess the reversible chemical processes of metastable perovskite under light-induced degradation and recovery. In addition, studies have shown that the shielded part of the PSMs during operation will not generate current but will form a reverse bias, which will cause internal ion migration and charge carrier accumulation, forming a thermal trap. ISOS-V recommends applying bias at the MPP or OC position in the dark to enhance understanding of PSM degradation under bias. Moreover, due to the potential masking effect of sensitive gas atmospheres on the intrinsic stability performance of PSMs, the ISOS-I protocol has been included in the assessment framework. It proposes maintaining a fixed atmospheric environment to eliminate this potential drawback. This is not established as an independent measure but rather serves as an addition to the aforementioned protocols. If an inert gas environment is adopted, it is considered to comply with the ISOS-I protocol.

Furthermore, within each pathway, there are three subdivisions, allowing for fine-grained control of the testing conditions. These are designed for various experimental conditions, with Level 3 representing more stringent testing requirements and higher equipment demands in the laboratory. Level 1, on the other hand, utilizes commonly available equipment and is considered the minimum requirement for stability testing. The specific testing conditions can be found in Table 5.[265,266]

7. Conclusions and outlook

In summary, important issues for PSMs, including structural design, scalable deposition theoretical models and methods, fabrication technologies for high-quality functional layers, and

Table 5 ISOS test standard specifications[266]

Test ID	Light source (stability)	Temperature	RH	Environment/set-up	Light source (IV)	Load
Dark storage (ISOS-D)						
ISOS-D-1	None	Ambient (23 ± 4 °C)	Ambient	Ambient air	Solar simulator/ sunlight	OC
ISOS-D-2	None	65, 85 °C	Ambient	Oven, ambient air	Solar simulator	OC
ISOS-D-3	None	65, 85 °C	85%	Env. chamber	Solar simulator	OC
Bias stability (ISOS-V)						
ISOS-V-1	None	Ambient (23 ± 4 °C)	Ambient	Ambient air	Solar simulator	Positive:
ISOS-V-2	None	65, 85 °C	Ambient	Oven, ambient air	Solar simulator	V_{MPP};
ISOS-V-3	None	65, 85 °C	85%	Env. chamber	Solar simulator	V_{oc}; E_g/q; J_{sc} Negative: V_{oc}, J_{MPPa}
Light-soaking (ISOS-L)						
ISOS-L-1	Solar simulator	Ambient (23 ± 4 °C)	Ambient	Light only	Solar simulator	MPP or OC
ISOS-L-2	Solar simulator	65, 85 °C	Ambient	Light/temperature	Solar simulator	MPP or OC
ISOS-L-3	Solar simulator	65, 85 °C	~50%	Light/temperature/RH	Solar simulator	MPP
Outdoor stability (ISOS-O)						
ISOS-O-1	Sunlight	Ambient	Ambient	Outdoor	Solar simulator	MPP or OC
ISOS-O-2	Sunlight	Ambient	Ambient	Outdoor	Sunlight	MPP or OC
ISOS-O-3	Sunlight	Ambient	Ambient	Outdoor	Sunlight/solar simulator	MPP
Thermal cycling (ISOS-T)						
ISOS-T-1	None	RT to 65, 85 °C	Ambient	Hot plate/oven	Solar simulator	OC
ISOS-T-2	None	RT to 65, 85 °C	Ambient	Oven/Env. chamber	Solar simulator	OC
ISOS-T-3	None	−40 to +85 °C	<55%	Env. chamber	Solar simulator	OC
Light cycling (ISOS-LC)						
ISOS-LC-1	Solar simulator/Dark	Ambient (23 ± 4 °C)	Ambient	Light only	Solar simulator	MPP or OC
ISOS-LC-2	cycle period: 2, 8, or 24 h;	65, 85 °C	Ambient	Light/temperature	Solar simulator	MPP or OC
ISOS-LC-3	Duty cycle: 1 : 1 or 1 : 2	65, 85 °C	<50%	Light/temperature/RH	Solar simulator	MPP
Solar-thermal cycling (ISOS-LT)						
ISOS-LT-1	Solar simulator	Linear/step ramping between RT and 65 °C	Monitored, uncontrolled	Weathering chamber	Solar simulator	MPP or OC
ISOS-LT-2	Solar simulator	Linear ramping between 5 °C and 65 °C	Monitored, controlled at 50% beyond 40 °C	Env. chamber with a sun simulator	Solar simulator	MPP or OC
ISOS-LT-3	Solar simulator	Linear ramping between −25 °C and 65 °C	Monitored, controlled at 50% beyond 40 °C	Env. chamber with sun simulator and freezing	Solar simulator	MPP or OC

product-oriented encapsulation and stability testing have been systematically investigated in recent years. Encouragingly, through collaborative efforts in both the academic and industrial communities, minimodules and large modules exceeding 800 cm^2 have achieved PCE of over 23% and 20%,[20,37] respectively, gradually approaching the energy conversion performance of silicon solar modules. However, considering commercialization demands, efficiency, stability, and safety are all essential and require further enhancement. In producing large PSMs, three critical steps: functional layer deposition, scribing, and encapsulation, will play decisive roles in addressing these urgent needs.

Several advancements can be observed from a materials-to-devices perspective on the manufacturing steps of PSMs. Firstly, interface, solvent, and additive engineering have been identified as effective means to adjust the inherent crystal structure and morphology, thereby enhancing efficiency and intrinsic stability in materials and physical theory. Device performance can be significantly improved by integrating chemical mechanisms such as anchoring and intermediates, along with energy level alignment between functional layers. Recent developments in surface passivation molecules provide researchers with improved methods for modifying shallow surface morphology. Secondly, the exploration of high-throughput and uniform deposition processes has facilitated the rapid industrialization and scale-up of PSMs. In particular, the mainstream meniscus coating technology warrants further investigation into the harmonious relationship between coating machine process parameters and the fluid dynamics of precursor solutions. Currently, the highest efficiencies in this process have been achieved through air knife-assisted fluid dynamics engineering for interface morphology control, indicating substantial potential for further development. In contrast, meniscus coating and printing technologies present more promising avenues for scalability. Thirdly, the limits of active area utilization are being continuously pushed by enhancing laser precision and patterning. Although breakthroughs such as the low dead zone technology achieving over 99.5% GFF for minimodules have been reported, the application area remains less than 3 cm^2 and further exploration into reliability and reproducibility in larger-area devices is warranted.[60] Fourthly, in terms of product durability and stability, perovskite materials are still highly sensitive. During large-area deposition, mixed components such as $MA_xFA_{(1-x)}PbI_3$ and $FA_xCs_{(1-x)}PbI_3$ have demonstrated superior chemical and operational stability within existing technologies, which merits attention. When addressing long-term operational concerns, encapsulation serves as a robust protective measure that can significantly mitigate the bidirectional penetration impacts on PSMs, including external mechanical and environmental influences, as well as internal material degradation and toxic material leakage. The single-sided glass vacuum lamination process is regarded as a suitable approach for application in PSMs due to its rapid and straightforward production workflow. Fifthly, the ISOS standards for perovskite stability testing represent an essential framework for the commercialization of PSMs, providing impetus for the emergence of better products. However current literature predominantly focuses on stability testing related to light soaking and cycling, while further exploration of thermal cycling and ultraviolet stability testing remains necessary.

On the basis of the increasingly mature technology in a single junction, tandem PSMs with a high theoretical efficiency limit have attracted wide attention. Among various technological pathways, silicon/perovskite tandems have demonstrated the most outstanding performance levels, reaching 34.6%.[13] The control of interface states between materials poses a significant challenge as the number of layers increases. Simultaneously, with an increasing number of interfaces, the phenomenon of delamination during long-term device operation will become more complex. Furthermore, by exploiting the tunable bandgap properties of perovskite, precise design of photoelectric matching for wide and narrow bandgap subcells is necessary to avoid spectral overlap and energy wastage.[267–269] With the current emergence of industrialization, the development of portable PSMs with functionalities such as flexibility and semi-transparency is a promising direction to meet diverse commercial demands. This opens up rich possibilities for wearable electronic applications. The bending resistance of F-PSMs is critically important, posing new challenges for the stability of their transport layers, perovskite materials, and the secure contact at interfaces. Moreover, their compatibility with R2R production methods makes it essential to explore large-scale printing processes that facilitate collaborative interactions among various material systems. Semi-transparent PSMs can be applied in contexts such as solar windows, significantly enhancing solar energy utilization, particularly in urban environments. Additionally, the inevitable leakage of lead from high-performance PSMs poses negative risks to both human health and the environment. The fatigue of materials in F-PSMs can further accelerate this leakage, making the exploration of lead-free perovskite components a crucial research avenue. Furthermore, it is necessary to develop specialized encapsulation materials and process to address these concerns effectively for unavailability due to rigid cover sheet.

Data availability

Data availability is not applicable to this article as no new data were created or analyzed in this study.

Conflicts of interest

The authors declare no conflict of interest.

Acknowledgements

This work is financially supported by the Research Center for Organic Electronics of the Hong Kong Polytechnic University (Project No. 1-CE0P). This work is also supported by the Research Grants Council of Hong Kong, China (Project No. 15306822) and the project of strategic importance of the Hong Kong Polytechnic University (Project No. ZE2X).

References

1 H. H. Liu, A. G. Aberle, T. Buonassisi and I. M. Peters, *Sol. Energy*, 2016, **135**, 598–604.
2 F. Li, F. R. Lin and A. K. Jen, *Adv. Mater.*, 2024, **36**, 2307161.
3 *Global Market Outlook For Solar Power 2023 - 2027*, **https://www.solarpowereurope.org/insights/market-outlooks/global-market-outlook-for-solar-power-2023-2027-1**, (accessed 11, 2023).
4 *Solar Panels Market Outlook & Forecasts 2024-2029: Green Building Initiatives Drive Demand, Enhancing Energy Efficiency and Sustainability*, **https://www.businesswire.com/news/home/20240902284683/en/Solar-Panels-Market-Outlook-Forecasts-2024-2029-Green-Building-Initiatives-Drive-Demand-Enhancing-Energy-Efficiency-and-Sustainability--ResearchAndMarkets.com**.
5 D.-Y. Son, J.-W. Lee, Y. J. Choi, I.-H. Jang, S. Lee, P. J. Yoo, H. Shin, N. Ahn, M. Choi, D. Kim and N.-G. Park, *Nat. Energy*, 2016, **1**, 16081.
6 J. S. Manser and P. V. Kamat, *Nat. Photonics*, 2014, **8**, 737–743.
7 S. De Wolf, J. Holovsky, S.-J. Moon, P. Loper, B. Niesen, M. Ledinsky, F.-J. Haug, J.-H. Yum and C. Ballif, *J. Phys. Chem. Lett.*, 2014, **5**, 1035–1039.
8 T. Miyasaka, *Chem. Lett.*, 2015, **44**, 720–729.
9 V. Gonzalez-Pedro, E. J. Juarez-Perez, W.-S. Arsyad, E. M. Barea, F. Fabregat-Santiago, I. Mora-Sero and J. Bisquert, *Nano Lett.*, 2014, **14**, 888–893.
10 J. Burschka, N. Pellet, S.-J. Moon, R. Humphry-Baker, P. Gao, M. K. Nazeeruddin and M. Grätzel, *Nature*, 2013, **499**, 316–319.
11 J. M. Frost, K. T. Butler, F. Brivio, C. H. Hendon, M. van Schilfgaarde and A. Walsh, *Nano Lett.*, 2014, **14**, 2584–2590.
12 A. Kojima, K. Teshima, Y. Shirai and T. Miyasaka, *J. Am. Chem. Soc.*, 2009, **131**, 6050–6051.
13 *Interactive Best Research-Cell Efficiency Chart*, **https://www.nrel.gov/pv/interactive-cell-efficiency.html**.
14 M. Yang, D. H. Kim, T. R. Klein, Z. Li, M. O. Reese, B. J. Tremolet de Villers, J. J. Berry, M. F. A. M. van Hest and K. Zhu, *ACS Energy Lett.*, 2018, **3**, 322–328.
15 K. Xiao, R. Lin, Q. Han, Y. Hou, Z. Qin, H. T. Nguyen, J. Wen, M. Wei, V. Yeddu, M. I. Saidaminov, Y. Gao, X. Luo, Y. Wang, H. Gao, C. Zhang, J. Xu, J. Zhu, E. H. Sargent and H. Tan, *Nat. Energy*, 2020, **5**, 870–880.
16 J. Zhuang, P. Mao, Y. Luan, N. Chen, X. Cao, G. Niu, F. Jia, F. Wang, S. Cao and J. Wang, *Adv. Funct. Mater.*, 2021, **31**, 2010385.
17 L. A. Castriotta, M. Zendehdel, N. Yaghoobi Nia, E. Leonardi, M. Löffler, B. Paci, A. Generosi, B. Rellinghaus and A. Di Carlo, *Adv. Energy Mater.*, 2022, **12**, 2103420.
18 Y. Xiao, C. Zuo, J.-X. Zhong, W.-Q. Wu, L. Shen and L. Ding, *Adv. Energy Mater.*, 2021, **11**, 2100378.
19 F. Matteocci, S. Razza, F. Di Giacomo, S. Casaluci, G. Mincuzzi, T. M. Brown, A. D'Epifanio, S. Licoccia and A. Di Carlo, *Phys. Chem. Chem. Phys.*, 2014, **16**, 3918–3923.
20 B. Ding, Y. Ding, J. Peng, J. Romano-deGea, L. E. K. Frederiksen, H. Kanda, O. A. Syzgantseva, M. A. Syzgantseva, J.-N. Audinot, J. Bour, S. Zhang, T. Wirtz, Z. Fei, P. Dörflinger, N. Shibayama, Y. Niu, S. Hu, S. Zhang, F. F. Tirani, Y. Liu, G.-J. Yang, K. Brooks, L. Hu, S. Kinge, V. Dyakonov, X. Zhang, S. Dai, P. J. Dyson and M. K. Nazeeruddin, *Nature*, 2024, **628**, 299–305.
21 J. Zhuang, C. Liu, B. Kang, H. Cheng, M. Xiao, L. Li and F. Yan, *Adv. Mater.*, 2023, 2309869.
22 P. J. S. Rana, B. Febriansyah, T. M. Koh, B. T. Muhammad, T. Salim, T. J. N. Hooper, A. Kanwat, B. Ghosh, P. Kajal, J. H. Lew, Y. C. Aw, N. Yantara, A. Bruno, S. A. Pullarkat, J. W. Ager, W. L. Leong, S. G. Mhaisalkar and N. Mathews, *Adv. Funct. Mater.*, 2022, **32**, 2113026.
23 M. Park, W. Cho, G. Lee, S. C. Hong, M.-C. Kim, J. Yoon, N. Ahn and M. Choi, *Small*, 2019, **15**, 1804005.
24 H. Eggers, F. Schackmar, T. Abzieher, Q. Sun, U. Lemmer, Y. Vaynzof, B. S. Richards, G. Hernandez-Sosa and U. W. Paetzold, *Adv. Energy Mater.*, 2020, **10**, 1903184.
25 F. De Rossi, J. A. Baker, D. Beynon, K. E. A. Hooper, S. M. P. Meroni, D. Williams, Z. Wei, A. Yasin, C. Charbonneau, E. H. Jewell and T. M. Watson, *Adv. Mater. Technol.*, 2018, **3**, 1800156.
26 L. B. Qiu, S. S. He, Y. Jiang and Y. B. Qi, *J. Mater. Chem. A*, 2021, **9**, 22759–22780.
27 S. Siegrist, S. C. Yang, E. Gilshtein, X. X. Sun, A. N. Tiwari and F. Fu, *J. Mater. Chem. A*, 2021, **9**, 26680–26687.
28 Z. Y. Jiang, B. K. Wang, W. J. Zhang, Z. C. Yang, M. J. Li, F. M. Ren, T. Imran, Z. X. Sun, S. S. Zhang, Y. Q. Zhang, Z. G. Zhao, Z. H. Liu and W. Chen, *J. Energy Chem.*, 2023, **80**, 689–710.
29 J. Zhuang, P. Mao, Y. Luan, X. Yi, Z. Tu, Y. Zhang, Y. Yi, Y. Wei, N. Chen, T. Lin, F. Wang, C. Li and J. Wang, *ACS Energy Lett.*, 2019, **4**, 2913–2921.
30 Y. Deng, X. Zheng, Y. Bai, Q. Wang, J. Zhao and J. Huang, *Nat. Energy*, 2018, **3**, 560–566.
31 W. Zhao, D. Lin, P. Guo, N. Jia, J. Wu, Q. Ye, F. Yan and H. Wang, *Adv. Funct. Mater.*, 2024, 2423096.
32 J. Park, J. Kim, H.-S. Yun, M. J. Paik, E. Noh, H. J. Mun, M. G. Kim, T. J. Shin and S. I. Seok, *Nature*, 2023, **616**, 724–730.
33 L. Rakocevic, L. E. Mundt, R. Gehlhaar, T. Merckx, T. Aernouts, M. C. Schubert, S. W. Glunz and J. Poortmans, *Sol. RRL*, 2019, **3**, 1900338.
34 *Champion Photovoltaic Module Efficiency Chart*, **https://www.nrel.gov/pv/module-efficiency.html**, 2024.
35 M. A. Green, E. D. Dunlop, M. Yoshita, N. Kopidakis, K. Bothe, G. Siefer, D. Hinken, M. Rauer, J. Hohl-Ebinger and X. Hao, *Prog. Photovoltaics Res. Appl.*, 2024, **32**, 425–441.
36 *KRICT Develops Innovative Perovskite Solar Cell with UniTest*, **https://www.businesskorea.co.kr/news/articleView.html?idxno=217516**.
37 *Wuxi Utmolight Technology*, **https://utmolight.com/en/**.
38 *RenShine Solar*, **https://www.renshinesolar.com/**, 2024.
39 *Kunshan GCL Photoelectric Materials*, **https://www.gcltech.com/en/goods/produce1/73.html**.
40 Z. Yang, Z. Liu, V. Ahmadi, W. Chen and Y. Qi, *Sol. RRL*, 2022, **6**, 2100458.
41 J. M. C. da Silva Filho, A. D. Gonçalves, F. C. Marques and J. N. de Freitas, *Sol. RRL*, 2022, **6**, 2100865.

42 W. Zhao, P. Guo, J. Wu, D. Lin, N. Jia, Z. Fang, C. Liu, Q. Ye, J. Zou, Y. Zhou and H. Wang, *Nano-Micro Lett.*, 2024, **16**, 191.
43 Z. Yang, W. Zhang, S. Wu, H. Zhu, Z. Liu, Z. Liu, Z. Jiang, R. Chen, J. Zhou, Q. Lu, Z. Xiao, L. Shi, H. Chen, L. K. Ono, S. Zhang, Y. Zhang, Y. Qi, L. Han and W. Chen, *Sci. Adv.*, 2021, **7**, eabg3749.
44 F. Di Giacomo, L. A. Castriotta, F. U. Kosasih, D. Di Girolamo, C. Ducati and A. Di Carlo, *Micromachines*, 2020, **11**, 1127.
45 A. L. Palma, *Sol. RRL*, 2020, **4**, 1900432.
46 S. Razza, S. Pescetelli, A. Agresti and A. Di Carlo, *Energies*, 2021, **14**, 1069.
47 A. L. Palma, F. Matteocci, A. Agresti, S. Pescetelli, E. Calabrò, L. Vesce, S. Christiansen, M. Schmidt and A. D. Carlo, *IEEE J. Photovolt.*, 2017, **7**, 1674–1680.
48 L. Qiu, S. He, Y. Jiang, D.-Y. Son, L. K. Ono, Z. Liu, T. Kim, T. Bouloumis, S. Kazaoui and Y. Qi, *J. Mater. Chem. A*, 2019, **7**, 6920–6929.
49 D. H. Kim, J. B. Whitaker, Z. Li, M. F. A. M. van Hest and K. Zhu, *Joule*, 2018, **2**, 1437–1451.
50 M. A. Alam and M. R. Khan, *Principles of Solar Cells*, Purdue University, USA, 2022.
51 S. Dongaonkar and M. A. Alam, *Prog. Photovoltaics Res. Appl.*, 2015, **23**, 170–181.
52 D. Castro, V. C. M. Duarte and L. Andrade, *ACS Omega*, 2022, **7**, 40844–40852.
53 S. Bhattarai, A. Sharma, D. Muchahary, M. Gogoi and T. D. Das, *Optik*, 2021, **243**, 167492.
54 L. Gao, L. Chen, S. Huang, X. Li and G. Yang, *ACS Appl. Energy Mater.*, 2019, **2**, 3851–3859.
55 B. Stegemann and C. Schultz, *Encycl. Appl. Phys.*, 2019, 1–30, DOI: **10.1002/3527600434.eap830**.
56 W. Zhao, P. Guo, C. Liu, N. Jia, Z. Fang, L. Ye, Q. Ye, Y. Xu, A. P. Glotov, A. A. Novikov, V. A. Vinokurov, D. Harvey, D. Shchukin and H. Wang, *Adv. Mater.*, 2023, **35**, 2300403.
57 L. Yu, W. Zhang, H. Ge, G. Yan, W. Yu, Y. Du, L. Zhou, W. Long and Y. Huang, 2023, **13**.
58 H. Higuchi and T. Negami, *Jpn. J. Appl. Phys.*, 2018, **57**, 08RE11.
59 L. Rakocevic, G. Schöpe, B. Turan, J. Genoe, T. Aernouts, S. Haas, R. Gehlhaar and J. Poortmans, *Prog. Photovoltaics Res. Appl.*, 2020, **28**, 1120–1127.
60 F. Di Giacomo, L. A. Castriotta, F. Matteocci and A. Di Carlo, *Adv. Energy Mater.*, 2024, 2400115.
61 Y. Gao, C. Liu, M. He, C. Zhang, L. Liu, Q. Luo, Y. Wu, H. Zhang, X. Zhong, R. Guo, Y. Xie, S. Wu, R. E. I. Schropp and Y. Mai, *Adv. Mater.*, 2023, 2309310.
62 E. Bi, W. Tang, H. Chen, Y. Wang, J. Barbaud, T. Wu, W. Kong, P. Tu, H. Zhu, X. Zeng, J. He, S.-I. Kan, X. Yang, M. Grätzel and L. Han, *Joule*, 2019, **3**, 2748–2760.
63 C. Chen, S. Zhang, S. Wu, W. Zhang, H. Zhu, Z. Xiong, Y. Zhang and W. Chen, *RSC Adv.*, 2017, **7**, 35819–35826.
64 Y. Yoo, G. Seo, H. J. Park, J. Kim, J. Jang, W. Cho, J. H. Kim, J. Shin, J. S. Choi, D. Lee, S.-W. Baek, S. Lee, S. M. Kang, M.-C. Kim, Y.-E. Sung and S. Bae, *J. Mater. Chem. A*, 2024, **12**, 1562–1572.
65 Y. Gao, K. Huang, C. Long, Y. Ding, J. Chang, D. Zhang, L. Etgar, M. Liu, J. Zhang and J. Yang, *ACS Energy Lett.*, 2022, **7**, 1412–1445.
66 Z. Yang, Y. Jiang, Y. Wang, G. Li, Q. You, Z. Wang, X. Gao, X. Lu, X. Shi, G. Zhou, J.-M. Liu and J. Gao, *Small*, 2024, **20**, 2307186.
67 X. Meng, Z. Cai, Y. Zhang, X. Hu, Z. Xing, Z. Huang, Z. Huang, Y. Cui, T. Hu, M. Su, X. Liao, L. Zhang, F. Wang, Y. Song and Y. Chen, *Nat. Commun.*, 2020, **11**, 3016.
68 L. Yuan, Z. Wang, R. Duan, P. Huang, K. Zhang, Q. Chen, N. K. Allam, Y. Zhou, B. Song and Y. Li, *J. Mater. Chem. A*, 2018, **6**, 19696–19702.
69 D. B. Ritzer, B. Abdollahi Nejand, M. A. Ruiz-Preciado, S. Gharibzadeh, H. Hu, A. Diercks, T. Feeney, B. S. Richards, T. Abzieher and U. W. Paetzold, *Energy Environ. Sci.*, 2023, **16**, 2212–2225.
70 H. C. Weerasinghe, N. Macadam, J.-E. Kim, L. J. Sutherland, D. Angmo, L. W. T. Ng, A. D. Scully, F. Glenn, R. Chantler, N. L. Chang, M. Dehghanimadvar, L. Shi, A. W. Y. Ho-Baillie, R. Egan, A. S. R. Chesman, M. Gao, J. J. Jasieniak, T. Hasan and D. Vak, *Nat. Commun.*, 2024, **15**, 1656.
71 G. E. Eperon, V. M. Burlakov, A. Goriely and H. J. Snaith, *ACS Nano*, 2014, **8**, 591–598.
72 J. Tong, Z. Song, D. H. Kim, X. Chen, C. Chen, A. F. Palmstrom, P. F. Ndione, M. O. Reese, S. P. Dunfield, O. G. Reid, J. Liu, F. Zhang, S. P. Harvey, Z. Li, S. T. Christensen, G. Teeter, D. Zhao, M. M. Al-Jassim, M. F. A. M. van Hest, M. C. Beard, S. E. Shaheen, J. J. Berry, Y. Yan and K. Zhu, *Science*, 2019, **364**, 475–479.
73 C. Zhang, C. Ji, Y.-B. Park and L. J. Guo, *Adv. Opt. Mater.*, 2021, **9**, 2001298.
74 S. Yoon, H. U. Ha, H.-J. Seok, H.-K. Kim and D.-W. Kang, *Adv. Funct. Mater.*, 2022, **32**, 2111760.
75 E. Magliano, P. Mariani, A. Agresti, S. Pescetelli, F. Matteocci, B. Taheri, A. Cricenti, M. Luce and A. Di Carlo, *ACS Appl. Energy Mater.*, 2023, **6**, 10340–10353.
76 X. Dai, Y. Deng, C. H. Van Brackle and J. Huang, *Int. J. Extreme Manuf.*, 2019, **1**, 022004.
77 C. K. Lun, S. B. Savage, D. Jeffrey and N. Chepurniy, *J. Fluid Mech.*, 1984, **140**, 223–256.
78 B. Levich and L. Landau, *Acta Physicochim. URSS*, 1942, **17**, 42.
79 M. Le Berre, Y. Chen and D. Baigl, *Langmuir*, 2009, **25**, 2554–2557.
80 R. L. Davis, S. Jayaraman, P. M. Chaikin and R. A. Register, *Langmuir*, 2014, **30**, 5637–5644.
81 S. G. Kwon and T. Hyeon, *Small*, 2011, **7**, 2685–2702.
82 M. Volmer, *Z. Phys. Chem.*, 1926, **119**, 277–301.
83 R. Becker and W. Döring, *Kinetic treatment of the nucleation in supersaturated vapors*, National Advisory Commitee for Aeronautics, 1954.
84 I. A. Howard, T. Abzieher, I. M. Hossain, H. Eggers, F. Schackmar, S. Ternes, B. S. Richards, U. Lemmer and U. W. Paetzold, *Adv. Mater.*, 2019, **31**, 1806702.
85 J. X. Zhong, W. Q. Wu, L. M. Ding and D. B. Kuang, *Energy Environ. Mater.*, 2021, **4**, 277–283.
86 F. Padinger, C. Brabec, T. Fromherz, J. C. Hummelen and N. S. Sariciftci, *Opto-Electron. Rev.*, 2000, **8**, 280–283.
87 M. Kaelin, D. Rudmann and A. N. Tiwari, *Sol. Energy*, 2004, **77**, 749–756.

88 S. Ito, T. Kitamura, Y. Wada and S. Yanagida, *Sol. Energy Mater. Sol. Cells*, 2003, **76**, 3–13.
89 G.-S. Kim, H.-K. Seo, V. P. Godble, Y.-S. Kim, O. B. Yang and H.-S. Shin, *Electrochem. Commun.*, 2006, **8**, 961–966.
90 S. Ito, Y. Makari, T. Kitamura, Y. Wada and S. Yanagida, *J. Mater. Chem.*, 2004, **14**, 385–390.
91 I. K. Ding, J. Melas-Kyriazi, N.-L. Cevey-Ha, K. G. Chittibabu, S. M. Zakeeruddin, M. Grätzel and M. D. McGehee, *Org. Electron.*, 2010, **11**, 1217–1222.
92 Y.-H. Chang, S.-R. Tseng, C.-Y. Chen, H.-F. Meng, E.-C. Chen, S.-F. Horng and C.-S. Hsu, *Org. Electron.*, 2009, **10**, 741–746.
93 B. Schmidt-Hansberg, M. F. G. Klein, K. Peters, F. Buss, J. Pfeifer, S. Walheim, A. Colsmann, U. Lemmer, P. Scharfer and W. Schabel, *J. Appl. Phys.*, 2009, **106**, 124501.
94 J. H. Kim, S. T. Williams, N. Cho, C.-C. Chueh and A. K. Y. Jen, *Adv. Energy Mater.*, 2015, **5**, 1401229.
95 C. Fei, N. Li, M. Wang, X. Wang, H. Gu, B. Chen, Z. Zhang, Z. Ni, H. Jiao, W. Xu, Z. Shi, Y. Yan and J. Huang, *Science*, 2023, **380**, 823–829.
96 P.-T. Tsai, K.-C. Yu, C.-J. Chang, S.-F. Horng and H.-F. Meng, *Org. Electron.*, 2015, **22**, 166–172.
97 S. Siegrist, P. Nandi, R. K. Kothandaraman, A. Abdessalem, A. N. Tiwari and F. Fu, *Sol. RRL*, 2023, **7**, 2300273.
98 A. T. Mallajosyula, K. Fernando, S. Bhatt, A. Singh, B. W. Alphenaar, J.-C. Blancon, W. Nie, G. Gupta and A. D. Mohite, *Appl. Mater. Today*, 2016, **3**, 96–102.
99 J. T. Matondo, H. Hu, Y. Ding, M. Mateen, G. Cheng and J. Ding, *Adv. Mater. Technol.*, 2024, **9**, 2302082.
100 D. Vak, K. Hwang, A. Faulks, Y.-S. Jung, N. Clark, D.-Y. Kim, G. J. Wilson and S. E. Watkins, *Adv. Energy Mater.*, 2015, **5**, 1401539.
101 L. Cai, L. Liang, J. Wu, B. Ding, L. Gao and B. Fan, *J. Semicond.*, 2017, **38**, 014006.
102 P. J. S. Rana, B. Febriansyah, T. M. Koh, A. Kanwat, J. Xia, T. Salim, T. J. N. Hooper, M. Kovalev, D. Giovanni, Y. C. Aw, B. Chaudhary, Y. Cai, G. Xing, T. C. Sum, J. W. Ager, S. G. Mhaisalkar and N. Mathews, *Adv. Mater.*, 2023, **35**, 2210176.
103 X. Ding, J. Liu and T. A. L. Harris, *AIChE J.*, 2016, **62**, 2508–2524.
104 J. B. Whitaker, D. H. Kim, B. W. Larson, F. Zhang, J. J. Berry, M. F. A. M. Van Hest and K. Zhu, *Sustainable Energy Fuels*, 2018, **2**, 2442–2449.
105 Y.-H. Seo, S.-P. Cho, H.-J. Lee, Y.-J. Kang, S.-N. Kwon and S.-I. Na, *J. Power Sources*, 2022, **539**, 231621.
106 I. Zimmermann, M. Al Atem, O. Fournier, S. Bernard, S. Jutteau, L. Lombez and J. Rousset, *Adv. Mater. Interfaces*, 2021, **8**, 2100743.
107 S. Chen, X. Dai, S. Xu, H. Jiao, L. Zhao and J. Huang, *Science*, 2021, **373**, 902–907.
108 G. Cotella, J. Baker, D. Worsley, F. De Rossi, C. Pleydell-Pearce, M. Carnie and T. Watson, *Sol. Energy Mater. Sol. Cells*, 2017, **159**, 362–369.
109 Y. Yang, Y. Wang, Z. Qu, K. Zhang, T. Liang, S. Chen, W. Lv, F. Min, Y. Chen and Y. Qiao, *Angew. Chem.*, 2023, **135**, e202300971.
110 Y. Y. Kim, T.-Y. Yang, R. Suhonen, A. Kemppainen, K. Hwang, N. J. Jeon and J. Seo, *Nat. Commun.*, 2020, **11**, 5146.
111 F. Huang, Y. Dkhissi, W. Huang, M. Xiao, I. Benesperi, S. Rubanov, Y. Zhu, X. Lin, L. Jiang and Y. Zhou, *Nano Energy*, 2014, **10**, 10–18.
112 I. W. Eames, N. J. Marr and H. Sabir, *Int. J. Heat Mass Transfer*, 1997, **40**, 2963–2973.
113 L.-L. Gao, C.-X. Li, C.-J. Li and G.-J. Yang, *J. Mater. Chem. A*, 2017, **5**, 1548–1557.
114 G. Park, Y. Cho, S. Jeong, J. Park, S.-J. Yoon and C. Yang, *J. Mater. Chem. A*, 2023, **11**, 12185–12193.
115 F. Guo, S. Qiu, J. Hu, H. Wang, B. Cai, J. Li, X. Yuan, X. Liu, K. Forberich, C. J. Brabec and Y. Mai, *Adv. Sci.*, 2019, **6**, 1901067.
116 F. Guo, W. He, S. Qiu, C. Wang, X. Liu, K. Forberich, C. J. Brabec and Y. Mai, *Adv. Funct. Mater.*, 2019, **29**, 1900964.
117 Q. Xiao, A. Zhang, W. Ye, X. Yang, Y. Zhu, B. Jiang, C. Ge, X. Li, H. Song, C. Chen and J. Tang, *Sol. RRL*, 2023, **7**, 2300486.
118 Y. Xu, C. Zhou, X. Li, K. Du, Y. Li, X. Dong, N. Yuan, L. Li and J. Ding, *Small Methods*, 2024, 2400428.
119 X. Peng, J. Yuan, S. Shen, M. Gao, A. S. R. Chesman, H. Yin, J. Cheng, Q. Zhang and D. Angmo, *Adv. Funct. Mater.*, 2017, **27**, 1703704.
120 Y. Wu, Y. Zhang, M. Yan, G. Hu, Z. Li, W. He, X. Wang, A. Abulimit and R. Li, *Appl. Mater. Today*, 2024, **36**, 102036.
121 J. H. Heo, M. H. Lee, M. H. Jang and S. H. Im, *J. Mater. Chem. A*, 2016, **4**, 17636–17642.
122 J.-W. Kang, Y.-J. Kang, S. Jung, M. Song, D.-G. Kim, C. Su Kim and S. H. Kim, *Sol. Energy Mater. Sol. Cells*, 2012, **103**, 76–79.
123 B. Tyagi, N. Kumar, H. B. Lee, M. M. Ovhal, V. V. Satale, A. Mohamed, D.-H. Kim and J.-W. Kang, *Small Methods*, 2024, **8**, 2300237.
124 X. Niu, N. Li, Z. Cui, L. Li, F. Pei, Y. Lan, Q. Song, Y. Du, J. Dou, Z. Bao, L. Wang, H. Liu, K. Li, X. Zhang, Z. Huang, L. Wang, W. Zhou, G. Yuan, Y. Chen, H. Zhou, C. Zhu, G. Liu, Y. Bai and Q. Chen, *Adv. Mater.*, 2023, **35**, 2305822.
125 J. H. Heo, F. Zhang, C. Xiao, S. J. Heo, J. K. Park, J. J. Berry, K. Zhu and S. H. Im, *Joule*, 2021, **5**, 481–494.
126 J. Silvano, S. Hamtaei, P. Verding, B. Vermang and W. Deferme, *ACS Appl. Energy Mater.*, 2023, **6**, 7363–7376.
127 H. Liu, G. Shi, R. Khan, S. Chu, Z. Huang, T. Shi, H. Sun, Y. Li, H. Zhou, P. Xiao, T. Chen and Z. Xiao, *Adv. Mater.*, 2024, **36**, 2309921.
128 N. A. N. Ouedraogo, Y. Ouyang, B. Guo, Z. Xiao, C. Zuo, K. Chen, Z. He, G. O. Odunmbaku, Z. Ma, W. Long, J. Yang, Y. Yuan, J. Fang, Q. Bao, C. Yi, X. Fang, H. Dong, Y. Yang, F. Liu, K. Yan, L. Ding and K. Sun, *Adv. Energy Mater.*, 2024, 2401463.
129 Z. Wei, H. Chen, K. Yan and S. Yang, *Angew. Chem., Int. Ed.*, 2014, **53**, 13239–13243.
130 D. A. Chalkias, A. Mourtzikou, G. Katsagounos, A. N. Kalarakis and E. Stathatos, *Small Methods*, 2023, **7**, 2300664.
131 F. Schackmar, H. Eggers, M. Frericks, B. S. Richards, U. Lemmer, G. Hernandez-Sosa and U. W. Paetzold, *Adv. Mater. Technol.*, 2021, **6**, 2000271.

132 L. Tan, H. Jiang, R. Yang, L. Shen, C. Sun, Y. Jin, X. Guan, P. Song, L. Zheng, C. Tian, L. Xie, J. Yang and Z. Wei, *Adv. Energy Mater.*, 2024, 2400549.
133 B. Gao and J. Meng, *Sol. Energy*, 2021, **230**, 598–604.
134 Y.-B. Cheng, A. Pascoe, F. Huang and Y. Peng, *Nature*, 2016, **539**, 488–489.
135 Y. D. Kim and J. Hone, *Nature*, 2017, **544**, 167–168.
136 C. T. K. Mai, J. Halme, H. A. Nurmi, A. M. da Silva, G. S. Lorite, D. Martineau, S. Narbey, N. Mozaffari, R. H. A. Ras, S. G. Hashmi and M. Vuckovac, *Adv. Sci.*, 2024, 2401016.
137 J. A. Sulpizio, L. Ella, A. Rozen, J. Birkbeck, D. J. Perello, D. Dutta, M. Ben-Shalom, T. Taniguchi, K. Watanabe, T. Holder, R. Queiroz, A. Principi, A. Stern, T. Scaffidi, A. K. Geim and S. Ilani, *Nature*, 2019, **576**, 75–79.
138 C. Chen, J. Chen, H. Han, L. Chao, J. Hu, T. Niu, H. Dong, S. Yang, Y. Xia, Y. Chen and W. Huang, *Nature*, 2022, **612**, 266–271.
139 Z. Ku, Y. Rong, M. Xu, T. Liu and H. Han, *Sci. Rep.*, 2013, **3**, 3132.
140 C. Chen, C. Ran, C. Guo, Q. Yao, J. Wang, T. Niu, D. Li, L. Chao, Y. Xia and Y. Chen, *Adv. Energy Mater.*, 2023, **13**, 2302654.
141 J. E. Huddy and W. J. Scheideler, *Adv. Funct. Mater.*, 2023, **33**, 2306312.
142 B. Roth, R. R. Søndergaard and F. C. Krebs, in *Handbook of Flexible Organic Electronics*, ed. S. Logothetidis, Woodhead Publishing, Oxford, 2015, pp. 171–197, DOI: 10.1016/B978-1-78242-035-4.00007-5.
143 G. Wang, M. A. Adil, J. Zhang and Z. Wei, *Adv. Mater.*, 2019, **31**, 1805089.
144 S. Alem, N. Graddage, J. Lu, T. Kololuoma, R. Movileanu and Y. Tao, *Org. Electron.*, 2018, **52**, 146–152.
145 M. Hösel, R. R. Søndergaard, M. Jørgensen and F. C. Krebs, *Adv. Eng. Mater.*, 2013, **15**, 1068–1075.
146 R. Søndergaard, M. Hösel, D. Angmo, T. T. Larsen-Olsen and F. C. Krebs, *Mater. Today*, 2012, **15**, 36–49.
147 J. E. Huddy, Y. Ye and W. J. Scheideler, *Adv. Mater. Technol.*, 2022, **7**, 2101282.
148 B. Parida, A. Singh, A. K. Kalathil Soopy, S. Sangaraju, M. Sundaray, S. Mishra, S. Liu and A. Najar, *Adv. Sci.*, 2022, **9**, 2200308.
149 J. Yang, D. Vak, N. Clark, J. Subbiah, W. W. Wong, D. J. Jones, S. E. Watkins and G. Wilson, *Sol. Energy Mater. Sol. Cells*, 2013, **109**, 47–55.
150 P. Kopola, T. Aernouts, R. Sliz, S. Guillerez, M. Ylikunnari, D. Cheyns, M. Välimäki, M. Tuomikoski, J. Hast and G. Jabbour, *Sol. Energy Mater. Sol. Cells*, 2011, **95**, 1344–1347.
151 G. Grau, J. Cen, H. Kang, R. Kitsomboonloha, W. J. Scheideler and V. Subramanian, *Flexible Printed Electron.*, 2016, **1**, 023002.
152 P. Kopola, M. Tuomikoski, R. Suhonen and A. Maaninen, *Thin Solid Films*, 2009, **517**, 5757–5762.
153 Y. Y. Kim, T. Y. Yang, R. Suhonen, M. Välimäki, T. Maaninen, A. Kemppainen, N. J. Jeon and J. Seo, *Adv. Sci.*, 2019, **6**, 1802094.
154 Y. Y. Kim, T.-Y. Yang, R. Suhonen, M. Välimäki, T. Maaninen, A. Kemppainen, N. J. Jeon and J. Seo, *Adv. Sci.*, 2019, **6**, 1802094.
155 E. Smecca, V. Valenzano, S. Valastro, I. Deretzis, G. Mannino, G. Malandrino, G. Accorsi, S. Colella, A. Rizzo, A. La Magna, A. Listorti and A. Alberti, *J. Mater. Chem. A*, 2021, **9**, 16456–16469.
156 M. R. Leyden, L. K. Ono, S. R. Raga, Y. Kato, S. Wang and Y. Qi, *J. Mater. Chem. A*, 2014, **2**, 18742–18745.
157 P.-S. Shen, J.-S. Chen, Y.-H. Chiang, M.-H. Li, T.-F. Guo and P. Chen, *Adv. Mater. Interfaces*, 2016, **3**, 1500849.
158 J. Zhou, L. Tan, Y. Liu, H. Li, X. Liu, M. Li, S. Wang, Y. Zhang, C. Jiang, R. Hua, W. Tress, S. Meloni and C. Yi, *Joule*, 2024, **8**, 1691–1706.
159 H. Li, J. Zhou, L. Tan, M. Li, C. Jiang, S. Wang, X. Zhao, Y. Liu, Y. Zhang, Y. Ye, W. Tress and C. Yi, *Sci. Adv.*, 2022, **8**, eabo7422.
160 M. Liu, M. B. Johnston and H. J. Snaith, *Nature*, 2013, **501**, 395–398.
161 J. Li, H. Wang, X. Y. Chin, H. A. Dewi, K. Vergeer, T. W. Goh, J. W. M. Lim, J. H. Lew, K. P. Loh, C. Soci, T. C. Sum, H. J. Bolink, N. Mathews, S. Mhaisalkar and A. Bruno, *Joule*, 2020, **4**, 1035–1053.
162 Y. Wang, P. Lv, J. Pan, J. Chen, X. Liu, M. Hu, L. Wan, K. Cao, B. Liu, Z. Ku, Y.-B. Cheng and J. Lu, *Adv. Mater.*, 2023, **35**, 2304625.
163 Q. Zhao, B. Zhang, W. Hui, Z. Su, H. Wang, Q. Zhang, K. Gao, X. Zhang, B.-H. Li, X. Gao, X. Wang, S. De Wolf, K. Wang and S. Pang, *J. Am. Chem. Soc.*, 2024, **146**, 19108–19117.
164 C. Huang, S. Tan, B. Yu, Y. Li, J. Shi, H. Wu, Y. Luo, D. Li and Q. Meng, *Joule*, 2024, **8**, 2539–2553.
165 Y. Zhu, Y. Zhang, M. Hu, L. Wan, W. Huang, J. Chu, Y. Hao, Y.-B. Cheng, A. N. Simonov and J. Lu, *Small Methods*, 2024, 2401244.
166 T. Xu, Y. Li, H. Cai, Y. Zhu, C. Liu, B. Han, Z. Hu, F. Zhang, J. Ni, J. Li and J. Zhang, *Sol. Energy*, 2024, **272**, 112461.
167 H. Yang, J. Wang, X. Yu, Y. Feng, X. Chen, F. Long, Z. Ku, F. Huang, Y. Cheng and Y. Peng, *Chem. Phys. Lett.*, 2022, **807**, 140084.
168 G. Tong, J. Zhang, T. Bu, L. K. Ono, C. Zhang, Y. Liu, C. Ding, T. Wu, S. Mariotti, S. Kazaoui and Y. Qi, *Adv. Energy Mater.*, 2023, **13**, 2300153.
169 Q. Chang, Y. Yun, K. Cao, W. Yao, X. Huang, P. He, Y. Shen, Z. Zhao, M. Chen, C. Li, B. Wu, J. Yin, Z. Zhao, J. Li and N. Zheng, *Adv. Mater.*, 2024, **36**, 2406296.
170 W. Chen, Y. Wu, Y. Yue, J. Liu, W. Zhang, X. Yang, H. Chen, E. Bi, I. Ashraful, M. Grätzel and L. Han, *Science*, 2015, **350**, 944–948.
171 N. Li, Z. Shi, C. Fei, H. Jiao, M. Li, H. Gu, S. P. Harvey, Y. Dong, M. C. Beard and J. Huang, *Nat. Energy*, 2024, **9**, 1264–1274.
172 S. Chen, X. Xiao, H. Gu and J. Huang, *Sci. Adv.*, 2021, **7**, eabe8130.
173 F. Wang, T. Liu, Y. Liu, Y. Zhou, X. Dong, Y. Zhang, X. Shi, Y. Dou, Z. Ren, L. Wang, Y. Zhao, S. Luo, X. Hu, X. Peng, C. Bao, W. Wang, J. Wang, W. Hu and S. Chen, *Adv. Mater.*, 2024, 2412059.
174 J. Gong, S. B. Darling and F. You, *Energy Environ. Sci.*, 2015, **8**, 1953–1968.

175 S. Zouhair, C. Clegg, I. Valitova, S. March, J. M. Jailani and V. Pecunia, *Sol. RRL*, 2024, **8**, 2300929.
176 M. Forouzandeh, M. Heidariramsheh, H. R. Heydarnezhad, H. Nikbakht, M. Stefanelli, L. Vesce and N. Taghavinia, *Carbon*, 2024, **229**, 119450.
177 F. Yang, L. Dong, D. Jang, B. Saparov, K. C. Tam, K. Zhang, N. Li, C. J. Brabec and H.-J. Egelhaaf, *Adv. Energy Mater.*, 2021, **11**, 2101219.
178 M. Xu, W. Ji, Y. Sheng, Y. Wu, H. Cheng, J. Meng, Z. Yan, J. Xu, A. Mei, Y. Hu, Y. Rong and H. Han, *Nano Energy*, 2020, **74**, 104842.
179 C. Fei, A. Kuvayskaya, X. Shi, M. Wang, Z. Shi, H. Jiao, T. J. Silverman, M. Owen-Bellini, Y. Dong, Y. Xian, R. Scheidt, X. Wang, G. Yang, H. Gu, N. Li, C. J. Dolan, Z. J. D. Deng, D. N. Cakan, D. P. Fenning, Y. Yan, M. C. Beard, L. T. Schelhas, A. Sellinger and J. Huang, *Science*, 2024, **384**, 1126–1134.
180 H. Gu, C. Fei, G. Yang, B. Chen, M. A. Uddin, H. Zhang, Z. Ni, H. Jiao, W. Xu, Z. Yan and J. Huang, *Nat. Energy*, 2023, **8**, 675–684.
181 J. Chang, E. Feng, X. Feng, H. Li, Y. Ding, C. Long, S. Lu, H. Zhu, W. Deng, J. Shi, Y. Yang, S. Xiao, Y. Yuan and J. Yang, *Nano Res.*, 2024, **17**, 8068–8076.
182 A. Lan, H. Lu, B. Huang, F. Chen, Z. Chen, J. Wang, L. Li and H. Do, *ACS Appl. Mater. Interfaces*, 2024, **16**, 64825–64833.
183 M. M. Lee, J. Teuscher, T. Miyasaka, T. N. Murakami and H. J. Snaith, *Science*, 2012, **338**, 643–647.
184 B. Conings, L. Baeten, C. De Dobbelaere, J. D'Haen, J. Manca and H.-G. Boyen, *Adv. Mater.*, 2013, **26**, 2041–2046.
185 H.-S. Kim, C.-R. Lee, J.-H. Im, K.-B. Lee, T. Moehl, A. Marchioro, S.-J. Moon, R. Humphry-Baker, J.-H. Yum and J. E. Moser, *Sci. Rep.*, 2012, **2**, 591.
186 J. Chen, Y. Xiong, Y. Rong, A. Mei, Y. Sheng, P. Jiang, Y. Hu, X. Li and H. Han, *Nano Energy*, 2016, **27**, 130–137.
187 K. H. Hendriks, J. J. van Franeker, B. J. Bruijnaers, J. A. Anta, M. M. Wienk and R. A. J. Janssen, *J. Mater. Chem. A*, 2017, **5**, 2346–2354.
188 Y. Deng, C. H. Van Brackle, X. Dai, J. Zhao, B. Chen and J. Huang, *Sci. Adv.*, 2019, **5**, eaax7537.
189 D.-K. Lee, K.-S. Lim, J.-W. Lee and N.-G. Park, *J. Mater. Chem. A*, 2021, **9**, 3018–3028.
190 L. Guo, Y. Chen, G. Wang, Y. Xia, D. Luo, Z. Zhu, C. Wang, W. Dong and S. Wen, *ACS Appl. Energy Mater.*, 2021, **4**, 2681–2689.
191 J. Chung, S.-W. Kim, Y. Li, T. Mariam, X. Wang, M. Rajakaruna, M. M. Saeed, A. Abudulimu, S. S. Shin, K. N. Guye, Z. Huang, R. J. E. Westbrook, E. Miller, B. Subedi, N. J. Podraza, M. J. Heben, R. J. Ellingson, D. S. Ginger, Z. Song and Y. Yan, *Adv. Energy Mater.*, 2023, **13**, 2300595.
192 S. Y. Abate, Y. Qi, Q. Zhang, S. Jha, H. Zhang, G. Ma, X. Gu, K. Wang, D. Patton and Q. Dai, *Adv. Mater.*, 2024, **36**, 2310279.
193 L. Yuan, X. Chen, X. Guo, S. Huang, X. Wu, Y. Shen, H. Gu, Y. Chen, G. Zeng, H.-J. Egelhaaf, C. J. Brabec, F. Yang, Y. Li and Y. Li, *Angew. Chem., Int. Ed.*, 2024, **63**, e202316954.
194 X. Jiang, B. Zhang, G. Yang, Z. Zhou, X. Guo, F. Zhang, S. Yu, S. Liu and S. Pang, *Angew. Chem., Int. Ed.*, 2023, **62**, e202302462.
195 P. Shi, Y. Ding, B. Ding, Q. Xing, T. Kodalle, C. M. Sutter-Fella, I. Yavuz, C. Yao, W. Fan, J. Xu, Y. Tian, D. Gu, K. Zhao, S. Tan, X. Zhang, L. Yao, P. J. Dyson, J. L. Slack, D. Yang, J. Xue, M. K. Nazeeruddin, Y. Yang and R. Wang, *Nature*, 2023, **620**, 323–327.
196 T. Bu, L. K. Ono, J. Li, J. Su, G. Tong, W. Zhang, Y. Liu, J. Zhang, J. Chang, S. Kazaoui, F. Huang, Y.-B. Cheng and Y. Qi, *Nat. Energy*, 2022, **7**, 528–536.
197 M. A. Uddin, P. J. S. Rana, Z. Ni, G. Yang, M. Li, M. Wang, H. Gu, H. Zhang, B. D. Dou and J. Huang, *Nat. Commun.*, 2024, **15**, 1355.
198 K. Odysseas Kosmatos, L. Theofylaktos, E. Giannakaki, D. Deligiannis, M. Konstantakou and T. Stergiopoulos, *Energy Environ. Mater.*, 2019, **2**, 79–92.
199 X. Shen, B. M. Gallant, P. Holzhey, J. A. Smith, K. A. Elmestekawy, Z. Yuan, P. V. G. M. Rathnayake, S. Bernardi, A. Dasgupta, E. Kasparavicius, T. Malinauskas, P. Caprioglio, O. Shargaieva, Y.-H. Lin, M. M. McCarthy, E. Unger, V. Getautis, A. Widmer-Cooper, L. M. Herz and H. J. Snaith, *Adv. Mater.*, 2023, **35**, 2211742.
200 Y. Zhao and K. Zhu, *J. Phys. Chem. C*, 2014, **118**, 9412–9418.
201 X. Pu, Q. Cao, X. He, J. Su, W. Wang, X. Zhang, D. Wang, Y. Zhang, J. Yang, T. Wang, H. Chen, L. Jiang, Y. Yan, X. Chen and X. Li, *Adv. Energy Mater.*, 2024, **14**, 2303972.
202 Z. Ren, Z. Cui, X. Shi, L. Wang, Y. Dou, F. Wang, H. Lin, H. Yan and S. Chen, *Joule*, 2023, **7**, 2894–2904.
203 W. Zhao, P. Guo, J. Su, Z. Fang, N. Jia, C. Liu, L. Ye, Q. Ye, J. Chang and H. Wang, *Adv. Funct. Mater.*, 2022, **32**, 2200534.
204 G. Yang, Z. Ni, Z. J. Yu, B. W. Larson, Z. Yu, B. Chen, A. Alasfour, X. Xiao, J. M. Luther and Z. C. Holman, *Nat. Photonics*, 2022, **16**, 588–594.
205 M. Kim, J. Jeong, H. Lu, T. K. Lee, F. T. Eickemeyer, Y. Liu, I. W. Choi, S. J. Choi, Y. Jo, H.-B. Kim, S.-I. Mo, Y.-K. Kim, H. Lee, N. G. An, S. Cho, W. R. Tress, S. M. Zakeeruddin, A. Hagfeldt, J. Y. Kim, M. Grätzel and D. S. Kim, *Science*, 2022, **375**, 302–306.
206 H. Tang, Z. Shen, Y. Shen, G. Yan, Y. Wang, Q. Han and L. Han, *Science*, 2024, **383**, 1236–1240.
207 Q. Cao, T. Wang, X. Pu, X. He, M. Xiao, H. Chen, L. Zhuang, Q. Wei, H.-L. Loi, P. Guo, B. Kang, G. Feng, J. Zhuang, G. Feng, X. Li and F. Yan, *Adv. Mater.*, 2024, **36**, 2311970.
208 X. Zheng, Z. Li, Y. Zhang, M. Chen, T. Liu, C. Xiao, D. Gao, J. B. Patel, D. Kuciauskas, A. Magomedov, R. A. Scheidt, X. Wang, S. P. Harvey, Z. Dai, C. Zhang, D. Morales, H. Pruett, B. M. Wieliczka, A. R. Kirmani, N. P. Padture, K. R. Graham, Y. Yan, M. K. Nazeeruddin, M. D. McGehee, Z. Zhu and J. M. Luther, *Nat. Energy*, 2023, **8**, 462–472.
209 Y. Ding, B. Ding, H. Kanda, O. J. Usiobo, T. Gallet, Z. Yang, Y. Liu, H. Huang, J. Sheng, C. Liu, Y. Yang, V. I. E. Queloz, X. Zhang, J.-N. Audinot, A. Redinger, W. Dang, E. Mosconic, W. Luo, F. De Angelis, M. Wang, P. Dörflinger, M. Armer, V. Schmid, R. Wang, K. G. Brooks, J. Wu, V. Dyakonov, G. Yang, S. Dai, P. J. Dyson and M. K. Nazeeruddin, *Nat. Nanotechnol.*, 2022, **17**, 598–605.

210 H. Song, H.-B. Kim, S. C. Cho, J. Lee, J. Yang, W. H. Jeong, J. Y. Won, H. I. Jeong, J. Yeop, J. Y. Kim, B. J. Lawrie, M. Ahmadi, B. R. Lee, M. Kim, S. J. Choi, D. S. Kim, M. Lee, S. U. Lee, Y. Jo and H. Choi, *Joule*, 2024, **8**, 2283–2303.
211 Q. Chang, Y. Yun, K. Cao, W. Yao, X. Huang, P. He, Y. Shen, Z. Zhao, M. Chen, C. Li, B. Wu, J. Yin, Z. Zhao, J. Li and N. Zheng, *Adv. Mater.*, 2024, 2406296.
212 X. Chen, F. Yang, L. Yuan, S. Huang, H. Gu, X. Wu, Y. Shen, Y. Chen, N. Li, H.-J. Egelhaaf, C. J. Brabec, R. Zhang, F. Gao, Y. Li and Y. Li, *Joule*, 2024, **8**, 2265–2282.
213 X. Liu, B. Ding, M. Han, Z. Yang, J. Chen, P. Shi, X. Xue, R. Ghadari, X. Zhang, R. Wang, K. Brooks, L. Tao, S. Kinge, S. Dai, J. Sheng, P. J. Dyson, M. K. Nazeeruddin and Y. Ding, *Angew. Chem., Int. Ed.*, 2023, **62**, e202304350.
214 H. Li, G. Xie, J. Fang, X. Wang, S. Li, D. Lin, D. Wang, N. Huang, H. Peng and L. Qiu, *Nano Energy*, 2024, **124**, 109507.
215 S. You, H. Zeng, Y. Liu, B. Han, M. Li, L. Li, X. Zheng, R. Guo, L. Luo, Z. Li, C. Zhang, R. Liu, Y. Zhao, S. Zhang, Q. Peng, T. Wang, Q. Chen, F. T. Eickemeyer, B. Carlsen, S. M. Zakeeruddin, L. Mai, Y. Rong, M. Grätzel and X. Li, *Science*, 2023, **379**, 288–294.
216 F. Ye, T. Tian, J. Su, R. Jiang, J. Li, C. Jin, J. Tong, S. Bai, F. Huang, P. Müller-Buschbaum, Y.-B. Cheng and T. Bu, *Adv. Energy Mater.*, 2024, **14**, 2302775.
217 Y. Yang, C. Liu, Y. Ding, B. Ding, J. Xu, A. Liu, J. Yu, L. Grater, H. Zhu, S. S. Hadke, V. K. Sangwan, A. S. R. Bati, X. Hu, J. Li, S. M. Park, M. C. Hersam, B. Chen, M. K. Nazeeruddin, M. G. Kanatzidis and E. H. Sargent, *Nat. Energy*, 2024, **9**, 316–323.
218 K. Zhang, Y. Wang, M. Tao, L. Guo, Y. Yang, J. Shao, Y. Zhang, F. Wang and Y. Song, *Adv. Mater.*, 2023, **35**, 2211593.
219 Z. Zhang, M. Li, R. Li, X. Zhuang, C. Wang, X. Shang, D. He, J. Chen and C. Chen, *Adv. Mater.*, 2024, 2313860.
220 T. Bu, J. Li, H. Li, C. Tian, J. Su, G. Tong, L. K. Ono, C. Wang, Z. Lin, N. Chai, X.-L. Zhang, J. Chang, J. Lu, J. Zhong, W. Huang, Y. Qi, Y.-B. Cheng and F. Huang, *Science*, 2021, **372**, 1327–1332.
221 Y. Wang, Y. Yang, N. Li, M. Hu, S. R. Raga, Y. Jiang, C. Wang, X.-L. Zhang, M. Lira-Cantu, F. Huang, Y.-B. Cheng and J. Lu, *Adv. Funct. Mater.*, 2022, **32**, 2204396.
222 J. W. Yoo, J. Jang, U. Kim, Y. Lee, S.-G. Ji, E. Noh, S. Hong, M. Choi and S. I. Seok, *Joule*, 2021, **5**, 2420–2436.
223 Y. Liu, B. Ding, G. Zhang, X. Ma, Y. Wang, X. Zhang, L. Zeng, M. K. Nazeeruddin, G. Yang and B. Chen, *Adv. Sci.*, 2024, **11**, 2309111.
224 Q. Cao, J. Yang, T. Wang, Y. Li, X. Pu, J. Zhao, Y. Zhang, H. Zhou, X. Li and X. Li, *Energy Environ. Sci.*, 2021, **14**, 5406–5415.
225 J. Zhuang, J. Wang and F. Yan, *Nano-Micro Lett.*, 2023, **15**, 84.
226 A. Uddin, M. B. Upama, H. Yi and L. Duan, *Coatings*, 2019, **9**, 65.
227 Y. Wang, I. Ahmad, T. Leung, J. Lin, W. Chen, F. Liu, A. M. C. Ng, Y. Zhang and A. B. Djurišić, *ACS Mater. Au*, 2022, **2**, 215–236.
228 T. Wang, Y. Li, Q. Cao, J. Yang, B. Yang, X. Pu, Y. Zhang, J. Zhao, Y. Zhang, H. Chen, A. Hagfeldt and X. Li, *Energy Environ. Sci.*, 2022, **15**, 4414–4424.
229 V. M. Goldschmidt, *Naturwissenschaften*, 1926, **14**, 477–485.
230 Z. Li, M. Yang, J.-S. Park, S.-H. Wei, J. J. Berry and K. Zhu, *Chem. Mater.*, 2016, **28**, 284–292.
231 Y. Zhang and N.-G. Park, *Adv. Funct. Mater.*, 2023, **33**, 2308577.
232 Y. Hu, M. F. Aygüler, M. L. Petrus, T. Bein and P. Docampo, *ACS Energy Lett.*, 2017, **2**, 2212–2218.
233 G. Wu, R. Liang, M. Ge, G. Sun, Y. Zhang and G. Xing, *Adv. Mater.*, 2022, **34**, 2105635.
234 S. Wang, A. Wang and F. Hao, *iScience*, 2022, **25**, 103599.
235 Q. Fu, X. Tang, B. Huang, T. Hu, L. Tan, L. Chen and Y. Chen, *Adv. Sci.*, 2018, **5**, 1700387.
236 Q.-Q. Chu, Z. Sun, D. Wang, B. Cheng, H. Wang, C.-P. Wong and B. Fang, *Matter*, 2023, **6**, 3838–3863.
237 M. Wong-Stringer, O. S. Game, J. A. Smith, T. J. Routledge, B. A. Alqurashy, B. G. Freestone, A. J. Parnell, N. Vaenas, V. Kumar, M. O. A. Alawad, A. Iraqi, C. Rodenburg and D. G. Lidzey, *Adv. Energy Mater.*, 2018, **8**, 1801234.
238 S. K. Yadavalli, C. L. Lanaghan, J. Palmer, A. J. Gayle, D. Penley, O. Okia, M. Zaccherini, O. Trejo, S. P. Dunfield, D. P. Fenning and N. P. Dasgupta, *ACS Appl. Mater. Interfaces*, 2024, **16**, 16040–16049.
239 R. Schmager, J. Roger, J. A. Schwenzer, F. Schackmar, T. Abzieher, M. Malekshahi Byranvand, B. Abdollahi Nejand, M. Worgull, B. S. Richards and U. W. Paetzold, *Adv. Funct. Mater.*, 2020, **30**, 1907481.
240 U. Erdil, M. Khenkin, W. M. Bernardes de Araujo, Q. Emery, I. Lauermann, V. Paraskeva, M. Norton, S. Vediappan, D. K. Kumar, R. K. Gupta, I. Visoly-Fisher, M. Hadjipanayi, G. E. Georghiou, R. Schlatmann, A. Abate, E. A. Katz and C. Ulbrich, *Energy Technol.*, 2025, **13**, 2401280.
241 J. Zhang, H. Wu, Y. Zhang, F. Cao, Z. Qiu, M. Li, X. Lang, Y. Jiang, Y. Gou, X. Liu, A. M. Asiri, P. J. Dyson, M. K. Nazeeruddin, J. Ye and C. Xiao, *Prog. Photovoltaics Res. Appl.*, 2024, **32**, 941–949.
242 Y. Rong, Y. Hu, A. Mei, H. Tan, M. I. Saidaminov, S. I. Seok, M. D. McGehee, E. H. Sargent and H. Han, *Science*, 2018, **361**, eaat8235.
243 W. Luo, Y. S. Khoo, P. Hacke, V. Naumann, D. Lausch, S. P. Harvey, J. P. Singh, J. Chai, Y. Wang, A. G. Aberle and S. Ramakrishna, *Energy Environ. Sci.*, 2017, **10**, 43–68.
244 V. Naumann, D. Lausch, A. Hähnel, J. Bauer, O. Breitenstein, A. Graff, M. Werner, S. Swatek, S. Großer, J. Bagdahn and C. Hagendorf, *Sol. Energy Mater. Sol. Cells*, 2014, **120**, 383–389.
245 J. Carolus, T. Merckx, Z. Purohit, B. Tripathi, H.-G. Boyen, T. Aernouts, W. De Ceuninck, B. Conings and M. Daenen, *Sol. RRL*, 2019, **3**, 1900226.
246 Z. Purohit, W. Song, J. Carolus, H. Chaliyawala, S. Lammar, T. Merckx, T. Aernouts, B. Tripathi and M. Daenen, *Sol. RRL*, 2021, **5**, 2100349.
247 L. Nakka, G. Shen, A. G. Aberle and F. Lin, *Sol. RRL*, 2023, **7**, 2300582.
248 IEC TS 62804-1-1: 2020, Photovoltaic (PV) modules - Test methods for the detection of potential-induced degradation - Part 1-1: Crystalline silicon - Delamination.

249 Q. Cao, T. Wang, J. Yang, Y. Zhang, Y. Li, X. Pu, J. Zhao, H. Chen, X. Li, I. Tojiboyev, J. Chen, L. Etgar and X. Li, *Adv. Funct. Mater.*, 2022, **32**, 2201036.
250 Y. Han, S. Meyer, Y. Dkhissi, K. Weber, J. M. Pringle, U. Bach, L. Spiccia and Y.-B. Cheng, *J. Mater. Chem. A*, 2015, **3**, 8139–8147.
251 P. Zhu, C. Chen, J. Dai, Y. Zhang, R. Mao, S. Chen, J. Huang and J. Zhu, *Adv. Mater.*, 2024, **36**, 2307357.
252 Z. Liu, B. Sun, T. Shi, Z. Tang and G. Liao, *J. Mater. Chem. A*, 2016, **4**, 10700–10709.
253 X. Zhang, Y. Zhou, Y. Li, J. Sun, X. Lu, X. Gao, J. Gao, L. Shui, S. Wu and J.-M. Liu, *J. Mater. Chem. C*, 2019, **7**, 3852–3861.
254 R. Cheacharoen, N. Rolston, D. Harwood, K. A. Bush, R. H. Dauskardt and M. D. McGehee, *Energy Environ. Sci.*, 2018, **11**, 144–150.
255 D. Hughes, M. Spence, S. K. Thomas, R. Apanavicius, C. Griffiths, M. J. Carnie and W. C. Tsoi, *J. Phys.: Energy*, 2024, **6**, 025001.
256 Z. Skafi, L. A. Castriotta, B. Taheri, F. Matteocci, M. Fahland, F. Jafarzadeh, E. Joseph, A. Chakraborty, V. Singh, V. Mottaghitalab, L. Mivehi, F. Brunetti, L. Sorbello, A. Di Carlo and T. M. Brown, *Adv. Energy Mater.*, 2024, **14**, 2400912.
257 T. Wang, J. Yang, Q. Cao, X. Pu, Y. Li, H. Chen, J. Zhao, Y. Zhang, X. Chen and X. Li, *Nat. Commun.*, 2023, **14**, 1342.
258 T. J. Wilderspin, F. De Rossi and T. M. Watson, *Sol. Energy*, 2016, **139**, 426–432.
259 Y. Jiang, L. Qiu, E. J. Juarez-Perez, L. K. Ono, Z. Hu, Z. Liu, Z. Wu, L. Meng, Q. Wang and Y. Qi, *Nat. Energy*, 2019, **4**, 585–593.
260 P. Mariani, M. Á. Molina-García, J. Barichello, M. I. Zappia, E. Magliano, L. A. Castriotta, L. Gabatel, S. B. Thorat, A. E. Del Rio Castillo, F. Drago, E. Leonardi, S. Pescetelli, L. Vesce, F. Di Giacomo, F. Matteocci, A. Agresti, N. De Giorgi, S. Bellani, A. Di Carlo and F. Bonaccorso, *Nat. Commun.*, 2024, **15**, 4552.
261 IEC 61215-2:2021, Terrestrial photovoltaic (PV) modules - Design qualification and type approval - Part 2, Test procedures.
262 M. Saliba, *Science*, 2018, **359**, 388–389.
263 H. J. Snaith and P. Hacke, *Nat. Energy*, 2018, **3**, 459–465.
264 K. Domanski, E. A. Alharbi, A. Hagfeldt, M. Grätzel and W. Tress, *Nat. Energy*, 2018, **3**, 61–67.
265 M. O. Reese, S. A. Gevorgyan, M. Jørgensen, E. Bundgaard, S. R. Kurtz, D. S. Ginley, D. C. Olson, M. T. Lloyd, P. Morvillo and E. A. Katz, *Sol. Energy Mater. Sol. Cells*, 2011, **95**, 1253–1267.
266 M. V. Khenkin, E. A. Katz, A. Abate, G. Bardizza, J. J. Berry, C. Brabec, F. Brunetti, V. Bulović, Q. Burlingame, A. Di Carlo, R. Cheacharoen, Y.-B. Cheng, A. Colsmann, S. Cros, K. Domanski, M. Dusza, C. J. Fell, S. R. Forrest, Y. Galagan, D. Di Girolamo, M. Grätzel, A. Hagfeldt, E. von Hauff, H. Hoppe, J. Kettle, H. Köbler, M. S. Leite, S. Liu, Y.-L. Loo, J. M. Luther, C.-Q. Ma, M. Madsen, M. Manceau, M. Matheron, M. McGehee, R. Meitzner, M. K. Nazeeruddin, A. F. Nogueira, Ç. Odabaşı, A. Osherov, N.-G. Park, M. O. Reese, F. De Rossi, M. Saliba, U. S. Schubert, H. J. Snaith, S. D. Stranks, W. Tress, P. A. Troshin, V. Turkovic, S. Veenstra, I. Visoly-Fisher, A. Walsh, T. Watson, H. Xie, R. Yıldırım, S. M. Zakeeruddin, K. Zhu and M. Lira-Cantu, *Nat. Energy*, 2020, **5**, 35–49.
267 E. Aydin, T. G. Allen, M. De Bastiani, A. Razzaq, L. Xu, E. Ugur, J. Liu and S. De Wolf, *Science*, 2024, **383**, eadh3849.
268 S. A. U. Hasan, M. A. Zahid, S. Park and J. Yi, *Sol. RRL*, 2024, **8**, 2300967.
269 J. J. Cordell, M. Woodhouse and E. L. Warren, *Joule*, 2025, **9**, 101781.

